Numerical Modeling of Air Ionization for Bioaerosol Removal and Deactivation of Aerosolized Virus by Air Ionization

by

Desmond Essien

A Thesis submitted to the Faculty of the Graduate Studies of

The University of Manitoba

in partial fulfillment of the requirements of the degree of

DOCTOR OF PHILOSOPHY

Department of Biosystems Engineering

University of Manitoba

Winnipeg

Abstract

The main objectives of this study were to numerically model negative air ionization for removal of bioaerosols and, to experimentally determine the effects of air ionization on the concentrations and the infectivity of aerosolized virus in enclosed spaces without ventilation. The Finite Volume Method (FVM) was used to simulate the physical processes of bioaerosol removal from air. A commercial software package (ANSYS FLUENT) was used to implement the FVM model. The transport of bioaerosols were modeled as a discrete phase using the Lagrangian approach under discrete random walk. The ions were modelled as unipolar (negatively charged) with a constant generation rate into the confined space. Experiments were conducted using a commercial ionizer in a chamber to validate the model and to quantify the effects of ionization on viral infectivity and virion (viral particles) concentrations. The model predictions of bioaerosol removal were within 22% of the measured values. The results showed that at a steady-state ion concentration of 2.4×10^{13} ion/m^3, ionization significantly reduced the concentrations of bioaerosols over time. The reduction of bioaerosol concentrations led to a one $\log_{10}$ reduction in virion concentrations over 90 s of ionization. Furthermore, at a steady-state ion concentration of 2.4×10^{13} ion/m^3, ionization began to cause a significant reduction in viral infectivity at 30 s of ionization until a two $\log_{10}$ reduction in viral infectivity was achieved at 90 s. However, at a steady state ion concentration of 3×10^{10} ion/m^3, ionization did not produce any significant effect on the viral infectivity. In conclusion, ionization is an effective technology for the purification of air in enclosed spaces when a critical ion threshold is present. The model presented in this study can be used as a tool to predict the spread and removal of bioaerosols in enclosed spaces.

Acknowledgements

Firstly, I would like to express my sincere gratitude and appreciation to God, the giver knowledge and Jesus Christ the giver of grace. I am most grateful to my advisor Dr. Qiang Zhang for his advice, guidance and the opportunities he offered to me throughout my Ph.D. studies. I would also like to thank my committee members: Dr. Kevin Coombs and Dr. David Levin for introducing me to the subject areas of micro and molecular biology and for guiding the direction of my research studies in these areas. Thank you also for permitting me to use your laboratories to conduct my experiments. I would also like to thank the Natural and Engineering Research Council of Canada (NSERC) for funding my study.

My special gratitude goes to the lab technician, Protiti Khan, who was always willing to set-up cells for me to conduct my plaque assays. I would also like to thank all my lab members at the Fort Garry campus: Amy La-Guzman, Xiaojie (Emily) Yan, Charles Nwaizu, Angelo De Luca and Kelsey Smyth for your constant support and ideas. My deep appreciation also goes to my other lab mates at the Bannatyne campus namely Kathleen Glover, Mahmud Rashid, Ali Zahedi and Affan Zahedi. Your helping hands, encouragement and ideas were helpful.

Finally, I would like to express my profound gratitude to my wife Awura-Ama Dampare and my kids; Praise, Doxanne and Desmond Jnr for the joy you brought to me each day. This work is dedicated to you.

Table of Contents

List of Tables

List of Figures

List of symbols

b	Ion mobility coefficient	$m^2/V/s$
$\overline{c_i}$	Thermal mean speed of ions	240 m/s at STP
C_c	Cunningham slip factor	
C_0	Negative ion concentration	$\#/m^3$
C_{tc}	Bioaerosol concentration at current time	$\#/cm^3$
C_{tp}	Bioaerosol concentration at previous time	$\#/cm^3$
D_i	Ion diffusion coefficient	m^2/s
d_p	Diameter of bioaerosol	m
e	Charge on an electron	1.6×10^{-19} C
$\vec{\mathrm{E}}$	Electric field strength	V/m
E_P	Peek's electric field Intensity	V/m
$\vec{F}_D$	Drag force acting on bioaerosol	N
$\vec{F}_x$	Electrostatic force acting on bioaerosol	N
I	Turbulence intensity	
$\vec{J}$	Current density	A/m^2
k	Boltzmann constant	$1.38064852 \times 10^{-23}$ m^2 kg s^{-2} K^{-1}
K_E	Electric field constant of proportionality	9×10^9 $N.m^2/C^2$
n_c	Integer number of elementary charges	
P	Gas pressure	Pa
P_O	Standard atmospheric pressure	101325 Pa
q_a	Charge on aerosol	C

q_e	Space charge density	(C/m^3)
r_o	Radius of corona wire	m
R_b	Bioaerosol removal rate	$\#cm^{-3}s^{-1}$
t	Bioaerosol resident time	s
T	Simulation gas temperature	K
T_O	Standard temperature	293K
$\vec{u}$	Gas velocity	m/s
$\vec{u}_a$	Bioaerosol velocity	m/s
$\bar{u}_i$	Mean velocity	m/s
u'_i	Fluctuating velocity	m/s
ε_0	Permittivity of space	F/m
μ_t	Turbulent viscosity	m^2/s
$\emptyset$	Electric potential	V
ρ_f	Gas density	kg/m^3

Plaque Assay Symbols

B_R	Biosampler rate	L/min
T_S	Sampling time	mins
V_{AS}	Volume of air sampled	m^3
V_{BC}	Volume of liquid generated into the chamber	ml
V_{iB}	Virus titer in biosampler	PFU/mL
V_{iST}	Virus stock titer	PFU/mL

V_{iTC}	Virus titer in whole chamber	PFU/m^3
V_{TC}	Total volume of chamber	m^3

PCR symbols

V_{BG}	Virus genome in biosampler	VGCN/mL
V_{GC}	Concentration sampled during test	VGCN
V_{iS}	Concentration of virus sampled anytime during the test	PFU
V_{iP}	Virus titer obtained from plaque assay test	PFU/mL
V_{iGC}	Virus genome concentration in whole chamber	VGCN/m^3
V_{iSG}	Virus stock genome concentration	VGCN/mL
V_{ICG}	Final genome concentration	VGCN/Ml

List of Abbreviations

ASAP	Airborne Sample Analysis Platform
ASHRAE	American Society of Heating Refrigeration and Air Conditioning Engineers
BAdV	Bovine Adenovirus
BEM	Boundary Element Method
CaCV	Canine Calicivirus
CFL	Courant–Friedrichs–Lewy
CI	Confidence Interval
cDNA	Complementary Deoxyribonucleic Acid
CFU	Colony Forming Units
CFD	Computational Fluid Dynamics
CPM	Charge Plate Monitor
CPE	Cytopathic Effect
DPM	Discrete Phase Model
DNA	Deoxyribonucleic Acid
EHD	Electrohydrodynamics
EPI	Electrostatic Particle Ionization
FB	Fractional Bias

FEM	Finite Element Method
FRET	Fluorescence Resonance Energy Transfer
FVM	Finite Volume Method
GUI	Graphical User Interface
HEPA	High Efficiency Particulate Air
MoC	Method of Characteristics
MERV	Minimum Efficiency Reporting Values
MRV	Mammalian Reovirus
PDE	Partial Differential Equations
PBS	Phosphate-Buffered Saline
RAM	Random Access Memory
RH	Relative Humidity
RNA	Ribonucleic Acid
RP	Removal Percentage
SEM	Standard Error of Mean
SP	Survival Percentage
TUI	Text User Interface
UDM	User Define Memory

UDS	User Defined Scalar
ULPA	Ultra-Low Particulate Air
UV	Ultraviolet
UVGI	Ultraviolet Germicidal Irradiation
VGCN	Viral Genome Copy Number

1. Introduction

Indoor air quality is critical to the health and well-being of occupants. Clean air is essential for body's respiratory and metabolic processes, whereas poor air quality is known to produce physiological and psychological effects on inhabitants. Aerosols are one of the major sources of air pollution in the indoor environment. Fine aerosols can remain airborne for long periods of time and therefore serve as agents for airborne disease transmission. The pathway for airborne disease transmission is yet to be completely understood and the control thereof remains a technological challenge. Airborne disease transmission continues to pose a threat to human health. Airborne disease transmission has been reported to be a significant contributor of nosocomial infections (infections originating from hospitals). Hospitalized patients remain at risk of becoming infected with pathogens within the confines of the health facilities (Beggs 2003; Shrivastava et al. 2013).

Among the several methods for removing aerosols from the air, air ionization has gained increased research attention because of its effectiveness and relatively low costs. Air ionization involves the generation of ions which attach themselves to aerosols, causing aerosols to be electrically charged, and (negatively) charged aerosols are subsequently drawn to grounded surfaces, thus removed from the air. Several studies have shown air ionization to be a useful technology in purifying air that is loaded with non-pathogenic particulates. The application of air ionization in treating aerosolized pathogens within indoor environments is however rather limited. So far, fewer studies have been conducted to investigate the potential of air ionization as a useful technology for removal and inactivation of airborne pathogens in indoor environments. Compared

to other methods of air purification, few studies have shown air ionization as an effective technology for controlling airborne pathogens.

Ions do not only remove aerosolized pathogens physically from air but may also inactivate pathogens biologically. However, uncertainty remains as to what type of ions (positive, negative ions or a combination of both) that can be best utilized to most effectively inactivate pathogens. Furthermore, little is known of the exact length of time and concentrations of ions (time-dosage) required for inactivation of pathogens. Moreover, the responses of the different kinds of airborne pathogens (viruses, bacteria, fungi) to air ions are yet to be better understood. There also remains the possibility that, air ions may produce varied effects on pathogens of the same kind (for instance viruses in the same family) depending on the biological characteristics of the pathogen. Therefore, studies are required to foster our understanding of air ionization for airborne disease control. This when achieved will present air ionization as a favorable choice for reducing and preventing airborne disease transmission.

Another aspect of air ionization yet to be fully understood, is the interaction among various physical processes involved. Air ionization involves simultaneous processes of air movement, aerosol movement, ion transport, and ion and aerosol deposition. Attempts have been made by researchers to model these processes and their interactions, but with little success. Advances in the processing power of computers, in combination with advanced numerical methods present an opportunity for using numerical techniques to quantify air ionization processes. This study therefore aims to investigate the underlying mechanisms of air ionization processes for removal of

aerosolized pathogens from air through both experimental measurements and numerical simulations. The specific objectives of this thesis research were ;

1. To conduct laboratory experiments to determine the effectiveness of negative air ionization for the physical removal of bioaerosols in a confined space at an ion generation rate of 1.9×10^{14} ions/m^3s and ionization time of 180 seconds.
2. To conduct laboratory experiments to determine the effects of the generated negative ions on the infectivity and concentrations of aerosolized virus.
3. To numerically quantify the spatial distribution of negative ions and bioaerosols in a confined space during ionization.
4. To develop an integrated numerical model to predict the removal of bioaerosols by ionization.

2. Literature Review

2.1 Air quality and bioaerosols

Maintaining healthy air quality is critical to public health and well-being. Activities such as coughing, sneezing, walking, flushing toilets can generate significant amount of aerosols or bioaerosols, which may have significant impacts on microbial air quality that is essential to maintaining safe homes, workplaces and other indoor environments (Mandal and Brandl 2011). Aerosols are fine colloidal particles suspended in air or a gaseous medium (Hirst 1955). Bioaerosols are aerosols originating from a biological source or containing biological agents. Typically, bioaerosols contain viruses, fungi or bacteria. Bioaerosols have been reported to contribute to about 5 to 34% of indoor air pollution (Srikanth et al. 2008). In particular, bioaerosols are carriers of pathogenic microorganisms and play a critical role in airborne disease transmission.

Airborne disease transmission is an ancient concept however scientific research to study the mechanisms only began in the 1930s (Knight 1973). To date the mechanisms by which airborne disease transmission occur are yet to be fully understood and the airborne pathway for disease transmission is considered to be elusive (Zhao et al. 2014). Conceptually, airborne disease transmission occurs as follows: (i) aerosols are generated (disease pathogens are aerosolized, e.g., a sneeze by a sick person or animal); (ii) aerosols containing pathogens (bioaerosols) with aerodynamic diameter larger than 10 μm fall off onto surfaces due to gravity, while smaller aerosols remain airborne for extended hours; (iii) bioaerosols move with air currents to naïve hosts (humans or animals); and (iv) naïve hosts inhale bioaerosols and become infected. Bioaerosols

lesser than 2 μm are easily inhaled and can reach as far as the alveoli in human lungs, and therefore cause an airborne infection at relative low doses (Zhao et al. 2014).

2.2 Physical behavior of bioaerosols in air

The size of bioaerosols is one of the most important physical characteristics that dictates their behavior in air. Bioaerosol sizes are commonly described by their aerodynamic diameters. The aerodynamic diameter of a particle (aerosol) is defined as the diameter of a hypothetical spherical particle with a density of 1 g/cm^3 that has the same settling velocity (or resistance to motion) as the particle (Heber et al. 1988; Cambra-López et al. 2010). Particles with aerodynamic diameter sizes of 10 μm and less are termed as PM_{10}, while those with aerodynamic diameters of less than 2.5 μm are termed as $PM_{2.5}$. The settling times for aerosols released from a height of 3 m, are 10 s for 100 μm, 4 min for 20 μm, 17 min for 10 μm, and 62 min for 5 μm; particles with a diameter lesser than 3 μm hardly settle (Nicas et al. 2005). The sizes of bioaerosols are influenced by the source and method of aerosolization (Pillai and Ricke 2002). Coughing or sneezing generates an enormous quantity of bioaerosols with a greater percentage ranging from 5 to 10 μm (Nicas et al. 2005). Morawska et al. (2009) used an expiratory droplet investigation system (EDIS) to study droplet size distribution during respiratory activities and reported that unique physiological processes produced specific size distribution modes. In a study conducted by Lindsley et al. (2012), coughing was reported to generate between 10,000 to 308,600 particles per cough in a healthy human being however the same study also showed that a human infected with influenza expelled between 900 and 302,200 particles per cough with 63% of the particles generated in the respirable size fraction. When expelled by coughing, bioaerosols undergo size

reduction through evaporation and become a stable small droplet nuclei (Knight 1980; Nicas et al. 2005). Droplet nuclei can remain airborne for extended period of time until they are artificially removed from the air. Droplet nuclei however are hygroscopic in nature and when released into a humid environment, they swell back (Tellier 2006). The hygroscopic growth factor is commonly used to represent the hygroscopic growth of an aerosol and can be expressed as the ratio of the particle dry diameter (RH < 10) and the wet particle diameter at a specific RH (Zamora et al. 2011).

2.3 Biological characteristics of bioaerosols

After generation, bioaerosols undergo natural decay (removal of bioaerosols from air through natural means such as gravitational settling). Larger sized bioaerosols (>10 μm) settle quickly while the smaller sized ones remain airborne (Nicas et al. 2005). The survival fraction can be determined by measuring their concentrations in air using devices such as optical particle counters and other devices (Morawska et al. 2009). However, environmental factors continuously act on the bioaerosols, and often they shrink to sizes well below the detection limits of particle counters. Therefore, it becomes necessary to quantify the bioaerosol using biological means. The "biological concentrations" of bioaerosols captured from air can be determined using a technique called Polymerase Chain Reaction (PCR) (Zhao et al. 2012). The infectivity of captured bioaerosols also can be determined techniques such as plaque assay (for virus bioaerosols) and colony formation assay (for fungi and bacteria bioaerosols) (Franken et al. 2006; Baer and Kehn-Hall 2015). These techniques are discussed in detail in sections 2.4.2 and.2.4.3

2.3.1 Effects of environment on bioaerosols

Environmental factors, particularly temperature and relative humidity (RH) either by their individual or by their combined effects may inactivate the pathogens contained by bioaerosols. For example, during the 2009 influenza A (H1N1/2009) pandemic, studies showed that maintaining hospital premises at a certain temperature and relative humidity (RH) reduced the airborne survival of influenza virus when compared with medical outfits which did not maintain strict control of their indoor temperature and RH (Tang 2009). An important factor for biological decay of airborne microorganisms is the water content of air (Stark 1999). The metric commonly used to indicate water content in air is relative humidity, which is the ratio between the actual vapor pressure of air and the water vapor of saturated air at a certain temperature. Other metrics such as evaporation potential and absolute humidity are less commonly used to characterize the water content in air (Zhao et al. 2012). The ideal water content in the atmosphere (RH) and temperature required to maintain the survival of air borne pathogens vary with the agent (Cox 1987). The mechanisms by which RH affects the survival of airborne microorganisms are difficult to investigate; however, surface damage (for inactivation at high RH) and dehydration (for inactivation at low RH) have been hypothesized to be the most influential underlying causes (De Jong et al. 1973)

Temperature plays an important role in pathogen transmission by bioaerosols. For viruses, variations in temperatures can significantly affect their RNA, viral proteins and enzymes (Lowen et al. 2007). Maintaining temperatures at 60^{o}C for more than an hour inactivates most viruses (Tang 2009). It has been shown that low temperatures (7 to 8^{o}C) are optimal for the survival of

airborne influenza, and that survival decreases progressively at moderate (20.5 to 24 ^{o}C) and then high temperatures (greater than 30^{o}C) (Cooper 1961). Using guinea pigs housed individually in separate cages, Lowen et al. (2007) showed that influenza virus easily travels through the air under dry, cold conditions. In a subsequent study, they found that higher temperatures of ~30^{o}C inhibited bioaerosol transmission of the influenza virus (Lowen et al. 2008). Infectious Bursal Disease (IBD) virus, also known as Gumboro Disease Virus, can be transmitted via the airborne route in the form of bioaerosols at an optimal temperature of 20^{o}C (Zhao et al. 2012).

2.4 Quantification of biological characteristics of bioaerosols

2.4.1 Bioaerosol sampling

The first step in quantifying the biological characteristics of bioaerosols is to sample bioaerosols from the air. The distribution of bioaerosols in the air is very dynamic and therefore sampling of bioaerosols must reflect the true state of bioaerosols present in the airspace. The commonly used methods for bioaerosol sampling are impaction, impingement and filtration (Grinshpun et al. 2007). Techniques such as gravity sampling, electrostatic precipitation and cyclone have also been attempted for sampling bioaerosols. Generally, the sampling efficiency of a sampler is dependent on the particle aerodynamic diameter, wind (airflow) velocity and direction, as well as the inlet characteristics of the device (Grinshpun et al. 2007). The choice of sampling method depends on the objective of study. The methods typically used in sampling bioaerosols are summarized in Table 2.1.

Table 2.1 Bioaerosol sampling techniques (Adapted from Stark 1999).

Sampling method	Principle	Advantages	Disadvantages
Filtration	While air is pumped through a filter medium and the particles are caught in the medium pores of defined size	Simple, inexpensive, and efficient	Dehydration effects; difficult to remove material from the filter medium for subsequent analysis
Impaction	An abrupt change of airflow direction allows particles to be impacted onto a solid surface, such as an agar plate.	Collection of several ranges of particle size is possible; high Efficiency	Risk of particle; overload; limited sampling duration due to agar desiccation; expensive; time consuming
Impinger	Air is blown at high speed onto a liquid volume whereby airborne particles are captured in the liquid	No limited sampling duration; liquid sample can be easily used for subsequent biological testing; separation of clustered bacteria	Evaporation losses; samples must be analysed quickly; low airflow rates
Gravity Sampling	Based on the gravitational settling of larger particles onto liquid or semi-solid medium technique for bioaerosol sampling	Useful for sampling larger sized bioaerosols which settle quickly over time	Difficult to quantify the concentration and volume of the source air.

Filtration

Filtration occurs when air is passed through porous membrane filters usually made of glass fiber, gelatin, polycarbonate or polyvinylchloride (PVC). As air containing particles passes through a filter medium, it generates inertial and electrostatic forces which lock particles in the

pore spaces of the filter medium (Gilbert and Duchaine 2009). Filtration offers convenient sampling and is commonly used for personal sampling devices. One of the shortcomings of filtration is when used in environments highly loaded with bioaerosols, filters become clogged and makes it extremely difficult to quantify the aerosol concentration (Eduard and Heederik 1998).

Impaction

Impaction samplers draw air into a vessel and then force a change in direction causing the particles with high inertia to be impacted over a collection surface (Henningson et al. 1998; Hinds 1982). Particles with aerodynamic diameters larger than a specific size become impacted onto a collection surface, while smaller particles proceed to the next stage impact plate (Hinds, 1982). Impactors are differentiated in characteristics by the shape and size of inlet, the number of collection chambers and the kind of surface onto which the particles are impacted. Impaction surfaces commonly used are solid (slides) and semi solids (agar) or gelatin (Macher and Hansson 1987). The sampling efficiencies of impactors are strongly influenced by the shape and size of the inlet, as well as the air velocity and orientation of the sampling probe. Willeke et al. (1993) reported that when the inlet of an impactor is directed to face wind direction with an inlet air velocity above $5ms^{-1}$, less than 5% of 10 µm sized particles were collected.

Impingement

In impingement sampling, air is drawn through a narrow inlet into a liquid collecting medium. Particles suspended in the air get impinged into the collecting medium when the air is pushed through the liquid. When sampling is completed, aliquots of the collection medium may

be cultivated in growth media to quantify the biological parameters of bioaerosols. Impingers can be used only once during sampling and therefore a number of them may be needed when replicates are required for time dependent sampling (Cartwright et al. 2009). Impingers however can be reused after sterilization. The sampling efficiency of impingers is influenced by the orientation of the inlet and the speed of air movement. Sanchez- Monedero and Stentiford (2003) reported a collection efficiency of 9.6% at 4.5 ms^{-1} air speed across the inlet, however after using a baffle to create a still air condition the collection efficiency increased up to 99%.

Gravity Sampling

Gravity sampling is based on the gravitational settling of larger particles. It's a non-quantitative technique by which a liquid or semi-solid medium (agar) is exposed to an environment to collect bioaerosols in the environment. Over time, the larger bioaerosols settle and are captured by the media (Grinshpun et al. 2007). The use of gravitational sampling is limited because it is so difficult to quantify the concentration and volume of the source air. It therefore remains an unreliable technique for bioaerosol sampling. Once bioaerosols are sampled (captured), appropriate methods may be employed to quantify them. The following sub-sections describe various methods for quantifying the biological characteristics of bioaerosols.

2.4.2 Cell Culture /Plaque Assays

The invention of plaque assay in 1952 introduced an efficient means to quantitatively and qualitatively calculate live animal viral titers (Cooper 1961). The first stage of the plaque assay process involves infecting a confluent monolayer of appropriate susceptible cells with lytic virus

of an unknown concentration that has been serially diluted usually between 10 – 10 million-fold to achieve a countable number of 20 to 100 virions. The infected monolayer is subsequently covered with an overlay medium to prevent viral infection from spreading through either the convectional or mechanical flow of the liquid medium during viral propagation (Baer and Kehn-Hall 2015). Most often, semisolid or solid overlays such as methyl cellulose or carboxymethyl cellulose (CMC) and agarose have traditionally been used, however the development of novel liquid overlays such as Avicel 5-7 has brought about increased use in liquid overlays (Boutin et al. 1988; Baer and Kehn-Hall 2015). The preference of liquid overlays over traditional overlays lies in the ability of liquid overlays to be applied at room temperature. Moreover, application and removal of liquid overlays is significantly easier. Additionally, liquid overlays do not require warming, and hence delicate and heat labile viruses may also prove easier to plaque (Baer and Kehn-Hall 2015). The next stage after infection and application of the immobilizing overlay is the development of individual plaques. The infected cells will replicate lysis-infection cycle and further propagate the infections. This results in discrete and distinct plaques being formed. The plaques are usually visible between 2 to 14 days depending on the host cells and the viral growth kinetics. Crystal violet or neutral red can be used to counterstain the cellular monolayers prior to plaque counting. The plaques in the cellular monolayer can be counted either by eye or by using standard bright field microscopy.

While it is possible to quantify bioaerosols using the plaque assay technique after air has been sampled, most studies only use plaque assay to quantify virus before aerosolization. For example, La (2014) serially diluted Porcine Reproductive and Respiratory Syndrome Virus

(PRRSV) from a concentration of 1×10^7 to 1×10^1 plaque forming units (PFU)/mL before carrying out an RNA extraction for qRT-PCR quantification after air sampling. Sharma et al. (2015) investigated the efficacy of the Airborne Sample Analysis Platform (ASAP) 2800 bioaerosol sampler to collect representative samples of air and identify specific viruses suspended as bioaerosols. An innocuous replication-defective Bovine Adenovirus serotype 3 (BAdV3) was aerosolized in a controlled laboratory environment. The study showed that the ASAP, efficiently captured the (BAdV3) virus at 5×10^3 PFU. They also quantified the genome of the captured bioaerosols and obtained an equivalent concentration of 2×10^5 genome copies. Hagbom et al. (2015) aerosolized Canine Calicivirus (CaCV) and subjected them to ionization in a room for forty minutes. They subsequently took air samples and conducted plaque assays, and showed that viral infectivity was decreased by more than 97% by ionization.

2.4.3 Quantitative reverse transcriptase polymerase chain reaction (qRT-PCR)

This method involves the use of assays for the detection of specific nucleic acids. Quantitative reverse transcriptase polymerase chain reaction (qRT-PCR) has been used by several investigators for bioaerosol quantification (Dee et al. 2009; Otake et al. 2010; Zhao et al. 2012, La 2014). Quantitative reverse transcriptase polymerase chain reaction allows for the quantification of the initial viral genome copy number within a sample. The qRT-PCR process first requires the extraction of Ribonucleic acid (RNA) to obtain nucleic acids templates of appropriate quantity and purity (Guarino et al. 2007). The viral RNA is subsequently reverse transcribed into complementary Deoxyribonucleic acid (cDNA). A 40 cycle process is initiated in which the PCR machine is programmed to cycle through three thermal profiles to instigate

different reactions, namely: (i) denaturation : high temperatures are used to separate double stranded cDNA into single strands (ii) annealing : primers and probes are attached to complementary sequences on the single strands of the cDNA (iii) extension : DNA polymerase extends lengths of the primers to copy the single strand of cDNA that had a complementary sequence of the primer. During qRT-PCR process, the quantification of initial sample concentration cannot be completed without the use of probes. Though it is possible for researchers to design their own probes, the practice is progressively becoming obsolete. Commercial kits that contain all the necessary reagents to perform qRT-PCR are available. Probes contain two dyes called the reporter dye and the quencher dye. The quencher dye, when in proximity to the reporter dye, induces an event called Fluorescence Resonance Energy Transfer (FRET) in which the reporter's energy is transferred to the quencher dye rather than emitted. During the third step of qRT-PCR, when the DNA polymerase extends, it cleaves off the probe and releases the reporter dye, separating it from the quencher dye and allowing the reporter dye to emit fluorescence. The fluorescence that the reporter dye releases when cleaved is measured with the PCR machine and is used to measure the amplification of nucleic acid in the sample.

2.4.4 Plate Counting

This technique involves either directly impacting bioaerosols onto plate cultures or collection liquid may be plated on agar after sampling. Filters can be placed on to agar plates for culture. After appropriate incubation, microbial colonies from the deposited particles are counted and if the sampled air volume is known, the concentration of colony forming units (CFU) per m^3 can be calculated. This visual counting technique is limited in terms of contamination and particle

concentration. In the event of an overgrowth, the total volume of air should be reduced. Plate counting is not suitable for slow micro-organisms or for viruses or in the situation when an identification of a microbial species is required. It is estimated that up to 90% of pathogens may be viable yet not culturable after aerosolization (Heidelberg et al. 1997).

2.4.5 Microscopy

Microscopy is an important technique for direct visualization of bioaerosol particles. In combination with fluorescence and specific antibody stains, immunofluorescence microscopy permits precise identification of micro-organisms. Transmission electron microscope's resolution lies around 1 Å (0.1 nm) (Smith 2008), but this technique is expensive and labor intensive. Computer based image analysis have been developed and offer efficient ways for automatic sample analysis; however, the analysis requires a biological assay to be performed (Stark 1999).

2.5 Air purification technologies

2.5.1 Mechanical Filtration

Mechanical air filtration involves the use of air filters to capture bioaerosols onto a replaceable dry filter medium. The filtration process occurs by means of impactions, interception, diffusion or electrostatic attraction. Filters are commonly made from fibrous materials (Podgórski et al. 2006). Air filters are classified by their particle filtration efficiency and can be classified into four main groups namely: pre filter, medium filter, high efficiency particulate air (HEPA) filter and ultra-low particulate air (ULPA) (Ahn et al. 2006). The American Society of Heating Refrigeration and Air Conditioning Engineers (ASHRAE) and the air filter industry have

developed a standardized rating system of air filters based on a numbering scale which indicates "Minimum Efficiency Reporting Values (MERV)". The scale ranges from 1-16, with the highest (16) having 95% or greater efficiency in filtering 0.3 – 0.1 μm particulates. Medium filters have an efficiency of 60 – 90% for particulates that are 0.3 μm in size and bigger (Chuaybamroong et al. 2010). A combination arrangement of a prefilter and HEPA filters is often used for air quality improvement. HEPA filters may capture 99.97% of particulate matter, and bacteria with sizes of 0.3 μm and above. The filtration efficiency of ULPA filter is over 99.999% with particle diameters from 0.12 to 0.17-μm (Jamriska et al. 1997). HEPA filters are commonly used for air purification in places such as hospitals, respirators and vehicles (Brincat et al. 2016). An emerging material used for air filtration is non-woven nano-fibre material. Their filtration efficiencies are comparable to HEPA filters or even superior to them at smaller particle sizes (Wang et al. 2013). While filtration is a proven technology for air purification, the system operates with some drawbacks. The use of filters often results in significant pressure drop in the ventilation system, and thus energy losses (Fisk et al. 2002). The pressure drop for a medium filter is between 15 and 30 mmAq while those for HEPA and ULPA ranges from 25 to 50 mmAq (Fisk et al. 2002). Moreover, filters of the same rating do not always perform equally (Dee et al. 2009).

Air filtration using non-treated fibrous media is often the preferred method to remove air pollutants. However, the treatment of the fibrous media with other substances is increasingly becoming common. Media with charged fibers have been reported to lead to improved filtration performances. Verdenelli et al. (2002) treated glass acrylic filters with antimicrobial agents and carried out filtration removal efficiency tests. They reported that filters treated with antimicrobials

demonstrated markedly less microbial colonization (varieties of species), higher filtration efficiency and delayed deterioration of the filter. Park et al. (2009) installed a carbon fiber ionizer in front of a filter media to study the removal efficiency of the filter for submicron aerosol particles and bioaerosols in the range of 50 to 600 nm. They found out that in the absence of the ionizer, the particle removal efficiency was 31.4%, and the efficiency increased to 46.9% at an ion production rate of 6.4×10^{12} ions/s. They further reported that the survival fraction of *E.coli* exposed to positive ions for 1, 5, 10 minutes were 61.7%, 45.4% and 24.2%, respectively. Miaśkiewicz-Peska and Łebkowska (2011) treated filters with silver nitrate and tested for its ability to prevent microorganisms from colonization in the filter. They found out that antibacterial filter treatment resulted in a significant reduction in living bacterial cells.

2.5.2 Ultraviolet germicidal Irradiation (UVGI)

Ultraviolet (UV) lights have been used for purification of air. According to World Health Organization, UV light can be classified into three wavelength ranges; UV-A (315–400 nm), UV-B (280–315 nm) and UV-C (100–280 nm). UV-A generates reactive oxygen species which cause oxidative DNA damage leading to single strand and double strand DNA/RNA breaks. Exposure to UV-B does not directly result in the breakdown of the genetic material however the exposure may block the replication of the genetic material (Han et al. 2004). Moreover, some microorganisms may be able to recover from the effects of UV-A and UV-B through a repair mechanism (Liu et al. 2019). UV-C (ultraviolet germicidal irradiation, UVGI) however produces devastating and often unrecoverable effects on microorganisms. Application of UV-C light may result in the formation of pyrimidine dimers and thymine dimers, which interfere with DNA and

eventually lead to cell death. (Lin and Li 2002; Tseng and Li 2005). The effectiveness of UVGI is dependent on the irradiation dosage, the nature of air movement and the air moisture content (Beggs et al. 2005). Different types of microorganism respond differently to the dosage treatment of UVGI. An applied dosage of 1.6 × 104 $\mu Ws/cm^2$ produced 2 $\log_{10}$ reduction in fungal bioaerosols (Kujundzic et al. 2007), while a significantly lower dosage of 300 $\mu Ws/cm^2$ produced a 12-fold reduction in bacterial bioaerosols (Lidwell 1994).

Walker and Ko (2007) conducted a study to quantitatively characterize the UV susceptibility of sampling of aerosolized bacteriophage MS2, adenovirus serotype 2 (ATCC: VR-846) and murine hepatitis virus (MHV) Coronavirus. The viruses were subjected to 254 nm UV-C for 16 s at a UV dose of at a UV dose of 2608 $\mu W\ s/cm^2$. The viral infectivity results obtained showed that both MS2 and adenovirus aerosols were very resistant to UV air disinfection. The susceptibility of coronavirus aerosols was 7-10 times that of the MS2 and adenovirus aerosols.

Jung et al. (2011) developed a UV electrospray assisted (UVAPS) technology and used it to investigate the effect on *Escherichia coli* bioaerosols. At an irradiance of 16 $\mu W/cm^2$ and exposure time of up to 250 s, a 99.2% reduction of the bacteria infectivity occurred. However, the performance of the system was significantly enhanced by the presence of the electrospray technology, which is a form of ionization. While UVGI is a proven technology for air sterilization, the application of the technology may cause adverse effects such as skin reddening and conjuctivitis (Mamahlodi 2019). Often UVGI treatment has to be performed in a room without occupants.

2.5.3 Air ionization

Air ionization is a phenomenon whereby electrons with high energy and speed knock off electrons from gas molecule to create more electrons and ions in air. Air ionization is commonly triggered by corona discharge. Corona discharge takes place when an electrode supplied with a high electrical potential (greater than 5 kV) causes a partial electric discharge near the electrode (Bohgard and Eklund 1998). The partial discharge occurs when the electric field intensity in the region of the electrode exceeds a certain critical value called Peek's Value. The physical configuration of corona electrodes can set up by connecting an electrode with a smaller radius of curvature (pins) connected to a larger electrode (Bohgard and Eklund 1998). This is referred to as point-plane configuration. The electric field around the electrode with smaller radius of curvature is stronger than the larger electrode. (Electric field intensity is inversely proportional to the radius of an electrode). The voltage value at which corona discharge starts is known as the onset voltage. At the applied voltage becomes closer to the onset voltage, there is a region where the corona current increases proportionally with the applied voltage. This region is known as Ohm's law regime. When voltage is increased beyond Ohm's law regime, a complete breakdown of air occurs. The complete breakdown occurs because at that point, the electric field intensity exceeds the dielectric strength of the medium (gas).

Corona discharge can be categorized into positive and negative corona discharge. When a negative voltage is applied, negative corona discharge develops, whereas a positive voltage causes positive corona discharge. In negative corona discharge, the positive ions in the ionization zone are attracted to the corona electrode, leaving negative electrons in the air, which attach themselves

to neutral gas molecules to form negative ions. The presence of a strong negative electric field repels the negative ions to a region beyond the ionization zone. This region is known as the drift zone. In the drift zone, the negative ions attach themselves to airborne particles, causing the airborne particles to be negatively charge and subsequently be drawn to a grounded surface, thus removed from the air.

In positive corona discharge, the positive electric field accelerates electrons towards the electrode. The fast-moving electrons collide with air molecules and knock off more electrons, creating more positive ions in the air. The positive ions are repelled from the ionization zone to the drift zone where they attach themselves to airborne particles. Subsequently, the particles are subsequently drawn to grounded surfaces.

Numerous studies have been conducted to investigate the effectiveness of air ionization in the reduction of bioaerosols and airborne particles. Bohgard and Eklund (1998) investigated the effectiveness of air ionization in reduction of NaCl in an enclosed steel chamber and reported a three-fold decrease in the NaCl particles present in the air. Khan et al. (2000) utilized an air ionizer to investigate the efficiency of negative air ionization in reducing smoke concentration within a 0.5 m^3 enclosure and reported up to a six-fold removal rate. Grabarczyk (2001) conducted studies on a whole room air ionization by hanging a set of electrodes beneath the ceiling of a 50 m^3 room. He reported that 2 hours of whole room air ionization was effective in reducing dust present in the room by 100-fold. Lee et al. (2004) evaluated the efficiency of three commercial air ionizers in reducing aerosols with aerodynamic diameter between 0.04 – 2 μm. They reported that the most powerful device among the three removed about 97% of 0.1 μm particles from air after 30 minutes

of continuous operation of the ionizer. In a similar study, Grinshpun et al. (2005) evaluated five air ionizers (three stationary and two wearable) to determine their efficiency in reducing aerosol concentration within enclosed spaces. They reported that the more powerful of the two wearable ionizers removed 100% of aerosols (0.3 – 3 μm) after 1.5 hours of uninterrupted operation in the chamber under steady state air conditions. The most efficient stationary unit removed 100% of the particles (0.3 - 3μm) within 12 minutes.

Pushpawela et al. (2017) tested a small negative ion generator (Aironic AH-202) for removing ultrafine particles from indoor environments (operated within a closed chamber of volume 1 m^3, in a closed unventilated room of volume 20 m^3 and in three force-ventilated rooms of volume 32, 45 and 132 m^3 and compared performance of the device to a high-flow air filter fitted with a HEPA filter. The closed chamber studies were conducted with ambient particles and with smoke at particle number concentrations of 5×10^3 and 7×10^4 #/cm^3, respectively. In both cases, 70% removal efficiency was obtained in 15 minutes of ionization. They also reported that, the particle removal efficiency of both the ionizer and the air filter decreased as the room size increased. Both devices were also more effective in unventilated rooms than in ventilated rooms. They also found out the ionizer was clearly more efficient than the air filter in the three largest rooms. They concluded that air ionizers are more suited than high-flow air filters in removing ultrafine particles from rooms larger than about 25 m^3.

Clearly, air ionization has been proven to be effective in removing aerosols from air and thus a method of choice for air purification. However, our knowledge of physical mechanisms of the ion-particle interaction is still limited. Moreover, research on quantifying air ionization

mechanisms is rather sparse. To come to a complete understanding of the air ionization mechanisms, it is important that the physical processes can be quantified accurately.

2.5.4 Electrostatic Precipitation

The mechanism of electrostatic precipitation is based on air ionization. An electrostatic precipitator consists of a vertical row of thin wires spaced apart from a stack of metal plates. The plates are grounded are typically spaced about 1 to 16 cm apart. In its operation, the air containing aerosols is directed to flow horizontally between the stack of plates. A corona discharge is created by applying a high negative voltage between the wires and the plates. Consequently, negative ions flow from the wires to the plates and collide with aerosols. The aerosols are subsequently charged and attracted to grounded plates.

Hart et al. (2011) evaluated the effectiveness of an electrostatic filter portable air purifier for reducing the $PM_{2.5}$ produced from wood stoves. They measured particle count concentrations in six particle sizes and particle mass concentrations in two particle sizes for ten 12-hour purifier on and ten purifier off trials. Both particle count and mass concentrations were each reduced by 61-85 percent.

Kim et al. (2015) developed a novel electrostatic precipitator by introducing a wet-porous electrode (WPE) array to enhance the removal performance of ultrafine particles and water-soluble gaseous pollutants generated during manufacturing. The performance of the WPE-ESP was evaluated in terms of the removal efficiency of airborne particles and water-soluble gases under ESP operating conditions in which the ionization charge current, the applied electric field strength of the collection component, and the relative humidity (RH) were varied. A maximum removal

efficiency of ˜99.2% at a 73% RH was obtained. The ESP also removed sulfur dioxide (SO_2) and mitigated ozone (O_3, <10 ppb). Electrostatic precipitation however has been reported to be less damaging to microorganisms contained in bioaerosols (Mandal and Brandl 2011).

2.5.5 Application of air ionization for deactivating microoganisms

The application of ionization by corona discharge for air purification often emphasize on the physical removal of aerosols however little is known of the effects of ionization on inactivating airborne pathogens. The few studies that have been conducted so far, have yielded promising results.

Hagbom et al. (2015) conducted a study to determine the effect of ionization on viral infectivity. Canine Calicivirus was first aerosolized and the aerosols generated were captured by a portable ionizer. Virus samples were taken from the ionizer and used to conduct plaque assays. The reduction in infectivity obtained was greater than 97% after 40 minutes of ionization. They further demonstrated in the same study that; ionization prevented a 100% of guinea pigs from infection. Similarly, Gast et al. (1999), conducted a study to determine the effect of negative air ionization on the prevention of airborne transmission of *Salmonella enteritidis*. One-week old chicks were orally inoculated with *S. enteritidis* and housed in an upstream controlled-environment. Day old chicks were kept downstream in controlled environment cabinets with negative ionizers installed. A negative control without negative ionizers in the downstream was also set up in different cabinets. At 3 and 8-days post inoculation, *S. enteritidis* was found on the surface of 89.6% of the downstream chicks from cabinets without negative air ionizers, but on only 39.6% of the downstream chicks in the presence of the ionizers. Similarly, *S. enteritidis* was recovered from the

ceca of 53.1% of sampled downstream chicks in cabinets without ionizers, but from only 1.0% of the ceca of chicks in cabinets in which ionizers were installed. Fletcher et al. (2007) conducted a study to determine the effect ionization on seven bacterial species (*Staphylococcus aureus*, *Mycobacterium parafortuitum*, *Pseudomonas aeruginosa*, *Acinetobacter baumanii*, *Burkholderia cenocepacia*, *Bacillus subtilis* and *Serratia marcescens*). The bacterial species were exposed to both positive and negative ions in the presence of air. Two interventions were made to distinguish between effects caused by the action of: (i) the air ions (ii) ozone and (iii) the action of the electric field. Firstly, a thin mica sheet was placed between the ionization source and the bacteria, directly over agar plates. This intervention was aimed at leaving the electric field unaltered and this prevented the air ions from reaching the microbial samples. Furthermore, the mica plate prevented ozone produced from reaching the bacteria. The second intervention involved placing an earthed wire mesh directly above the agar plates. This was aimed at eliminating both the electric field and the air ions from having effect on the bacteria, while allowing any ozone present to reach the agar plate. Their results showed that, with the exception of *Mycobacterium parafortuitum*, the principal cause of cell death amongst the bacteria studied was exposure to ozone, while electroporation played a secondary role. However, in the case of *Mycobacterium parafortuitum*, electroporation resulting from exposure to the electric field was determined to might have been the principal cause of cell inactivation.

Hyun et al. (2017) studied the effect air ions generated by corona discharge on the anti-viral efficiency over determined times. They installed a carbon-fiber ionizer upstream of an air filter and an introduced aerosolized bacteriophage MS2 through the filter. Subsequently, they treated

the virus laden filter with another inflow of air ions. Captured virus were detached from the filter by sonification and the antiviral efficiency of the air ions was determined. They found out that the antiviral efficiency increased with ion exposure time and ion concentration. At positive air ions concentrations of 10^7 ions/cm^3, the antiviral efficiencies were 46.1, 78.8, and 83.7% with exposure times of 15, 30, and 45 mins, respectively. They further reported a further increased antiviral efficiency of the ionizer when a bipolar mode of the ionizer was operated (both negative and positive ions generated simultaneously). At number concentrations of positive and negative ions of 6.6×10^6 and 3.4×10^6 ions/cm^3 respectively (total of 10^7 ions/cm^3), the antiviral efficiencies of 64.3, 89.1, and 97.4% with exposure times of 15, 30, and 45 mins, were obtained respectively.

2.6 Numerical modelling of Air Ionization

2.6.1 Corona discharge

Most research studies on modelling the processes involved in corona discharge have been focused on describing the mechanisms of electrostatic precipitators (Lami et al. 1997; Kim and Lee 1999; Park and Chun 2002; Schmid 2003; Nikas et al. 2005; Skodras et al. 2006; Long and Yao 2010 ; Farnoosh et al. 2011). A demerit of the techniques used in modelling the electrostatic precipitation is the determination of the space charge density on the surface of the electrode. A trial and error iterative technique is commonly used to predict the charge density on the electrode until the values obtained can be correlated to the electric field intensity predicted by Peek's criteria. Consequently, the boundary conditions set for the charge density are often inaccurate. Moreover, modelling the performance of an electrostatic precipitator requires solving coupled equations of

the space charge density, gas flow and particle migration. The complexity involved often requires combining several analytical and numerical techniques to predict the particle removal processes.

Few studies have attempted to model corona discharge with known concentrations of ions at the electrode boundaries from where the ions are introduced into the system. Mayya et al. (2004) developed a technique for modelling unipolar air ionization mostly based on analytical methods. Ions were introduced into the chamber at a generation rate of 3.125×10^{12} ions per second. They successfully simulated the ion distribution within the chamber and subsequently predicted the removal of airborne particulates from the space. Results from the study were compared to experiemental data reported in literature and a close agreement was obtained. The model however fell short to describe the nature of the gas flow and spatial distributions of the ion concentrations over time. Noakes et al. (2007) presented a two-dimensional (2D) numerical model for corona generated by a negative ionizer. Ions at generation rates between 7×10^6 and 7×10^{10} ions/s were introduced from a point source into a chamber. They successfully simulated the transport of ions within the system. However, the model was not validated with experimental study. While these studies have attempted to model corona discharge with known concentrations at electrode boundaries, further studies are required to enhance our understanding of the mechanisms that govern the air ionization process.

2.6.2 Numerical techniques

The physical processes governing air ionization can be described using partial differential equations (PDE's). Solving sets of coupled PDE's can be complex and challenging, and therefore approximate solutions are often sought. The most common methods used for solving PDE's in the

study of ion generation and movement in enclosed spaces are Boundary Element Method (BEM), Finite Element Method (FEM) and Finite volume method (FVM).

2.6.3 Boundary Element Method (BEM)

The Boundary Element Method (BEM) is a very useful method in simulating ion movement from electrodes by providing solutions to the partial differential equations governing flows of the ions (Yamashita et al. 1988). Typically, in a corona discharge, a strong electric field surrounds the ion emitting electrodes and therefore simulation requires generating a mesh to discretize a small region of the domain around the electrodes and the entire flow field (Adamiak 1991). BEM requires only the electrode to be discretized, hence resulting in a reduced number of nodes and consequently quicker estimation of the ion flow around the electrode (Adamiak 1994). However, BEM is less efficient in estimating corona discharge within the domain of flow field and often must be coupled with another method to estimate ion movement (Potrymai and Perstnov 2014).

2.6.4 Finite Element Method (FEM)

The Finite Element Method perhaps is the most commonly used method for solving PDE's which govern physical problems. In its basic form, FEM requires the domain of interest to be split into small parts (elements) which can be interconnected to each other by means of nodes. This arrangement subsequently allows a mesh to be formed over the domain. FEM offers the flexibility of generating meshes of different shapes and sizes to fit the study area/volume (Butler et al. 1989). When FEM is employed in studying corona discharge, the mesh generated in the immediate surroundings of the electrode must be finer due to the intensive electric field present (Levin and

Hobur 1990). A mesh with larger element sizes can be used to study ion movement in areas far away from the electrodes (Davis and Hoburg 1983). Although FEM can be used to estimate fluid flow; it is best suited for modelling solid particles (Potrymai and Perstnov 2014).

2.6.5 Method of Characteristics (MoC)

The method of characteristics (MoC) is a numerical technique that can be used for reducing a partial differential equation to a family of ordinary differential equations along which the solution can be integrated from some initial data given on a suitable hypersurface (Adamiak 1991). MoC is suitable for solving the space charge density problems and is often used to obtain approximate solutions when ion diffusion into space can be neglected (Potrymai and Perstnov 2014). In its application, characteristic lines are traced from points on the corona electrode surface where electric charges are injected. The charge from the initial point with a determined value on the corona electrode decays as it approaches the collecting electrode along the characteristic field line (Butler et al.1989).

2.6.6 Finite Volume Method (FVM)

In Finite Volume Method (FVM), the domain of interest is discretized into control volumes. To maintain conservation of mass, momentum and energy within the domain, conservation principles are applied to each control volume (Versteeg and Malalasekra 2007). Transport equations are integrated over each control volume to yield sets of algebraic equations for each control volume (Long et al. 2009). The value of each variable is then stored in the node in the

centre of the cell or the mesh vertices. FVM offers the flexibility of creating unstructured grids and decreased computation time (Versteeg and Malalasekra 2007).

2.7 Model Validation

A model is an abstraction of reality. Model validation is the process of determining the degree to which a computer model is an accurate representation of the real world from the perspective of the intended model applications (ASME 2006) . A model may be valid for one set of experimental conditions and invalid in another (Johansson et al. 2010). The type of model validation often depends on the scope of application. Model validation is often discipline specific (e.g., air quality models, weather prediction models, water quality models etc.). "Depending on the intended goals associated with each discipline, the focus and approach are also different (Chang and Hanna 2004)".

Statistical approaches are often used to validate the performance of air quality models. The America Society of Testing and Materials (ASTM 2008) proposed some model validation techniques for air quality models. Measures such as the normalized mean square error, the geometric variance, the geometric mean, fractional bias, the correlation coefficient, and the fraction of predictions within a factor of two of observations are recommended. Models having a value of 1 for geometric variance or the correlation coefficient (R) are deemed to be perfect models. The systemic bias is often evaluated by geometric mean bias and fractional bias. A value of 0 obtained for geometric mean bias or fractional bias means the model predictions are unbiased and are in the direction of the observed data. For this study, the accuracy of the model was evaluated using the 95-confidence interval, and a one-one regression was used to determine the

co-efficient of determination (R^2) and the slope. The regression was also used to determine the overall percentage of the predicted values which fell within the 95-confidence interval of the measured data. Fractional bias as calculated in equation (2.1) was used to evaluate the bias in the model predictions. Other methods such as probability density functions, Turin test and some subjective methods have also been proposed for model validation however they were not used in this study.

$$FB = 2\frac{(C_{pre} - C_{Obs,average})}{(C_{pre} + C_{Obs,average})} \quad (2.1)$$

where:

FB = Fractional Bias

C_{pre} = predicted bioaerosol concentration (#/cm^3)

C_{Obs} = observed (measured) bioaerosol concentration (#/cm^3)

$C_{Obs,average}$ = averaged measured bioaerosol concentrations (#/cm^3)

The FB values range from 2 to -2 being acceptable, with zero (0) being the perfect agreement between the predicted and the measured data (ASTM 2008).

2.8 Application of numerical techniques for study of corona discharge

Due to the complex processes involved in corona discharge, a combination of two or more numerical techniques are often employed to study the phenomenon. Davis and Hoburg (1983)

presented a model for computing space charge density and electric field structures in wire duct-electrostatic precipitators. FEM was used to compute the electric potential and MoC used to predict charged density distribution. Their results showed that the predicted potential values agreed excellently with experimental data. Adamiak (1991) presented a combination approach of BEM and MoC to model the space charge density and the electric field in monopolar dc corona discharge areas. BEM was used to calculate the potential distribution (on assumption of known charge density) while MoC used for estimating the charge density from a given potential distribution. Both methods were used iteratively until a self-consistent solution is obtained. Davidson et al. (1996) employed a combination technique of FEM and MoC to develop a 3-D model for predicting the space charge density, current density, electric potential and electric field in three unique electrostatic configurations (point-to-plane, single-barb plate-to-plane, and hexagonal multiple-barbed plate-to-plate) electrostatic precipitator (ESP) geometries. Their initial results revealed that the model prediction of the total current (based on Peek's formula) did not agree with measured values. They further reported that the FEM-MoC approach could not specify the shape and size of the corona sheath. Zhao and Adamiak (2008) employed a hybrid FEM-MoC approach to study the flow regime during corona discharge and modelled the relationship between electrohydrodynamics (EHD) and Reynolds numbers (Re) in a single wire electrostatic precipitator. They reported that at very low Re (15) and high EHD (2000), the EHD dominated the flow in the channel. At higher Re (50) and low EHD (500), it was observed that the EHD flow decreased in the channel. Long et al. (2009) presented a model based on FVM for the computation of electrical conditions inside wire-plate electrostatic precipitators. The potential equation was discretized using a second-order

scheme and the space–charge density equation was discretized using a second-order upwind scheme. The discretization scheme was carried using unstructured cell meshes. They showed that the predicted results agreed well with the experimental data. Wu et al. (2013) utilized FVM to simulate complex geometries to accurately capture the charge density distribution. The numerical technique was applied to a blade-plane configuration. Their results were subsequently compared to values obtained from a combined FEM and MoC model and a good agreement was obtained. Illias et al. (2015) studied corona discharge between high voltage electrodes of different configurations (sharp, flat, sphere) and grounded surfaces using FEM. They successfully predicted the electric field distribution at distances up to four metres away from the electrodes. Wang (2016) employed a combination of FVM and FEM to study three ionic species, namely, positive ions, negative ions, and electrons. FEM was used to solve the Poisson's equation while FVM was used to solve the charge transport equation. Different time steps were applied to improve the computational efficiency when solving the charge transport equation. Density distributions of the three ionic species and the electrical field strength were further used to study Trichel pulses. Good agreements were obtained between the simulated results and experimental data.

2.9 Computational Fluid Dynamics (CFD) modelling of airborne disease transmission

Computational Fluid Dynamics (CFD) is a numerical method used to simulate fluid systems in either an open or closed space. The method is based on the governing physical laws of energy, mass and momentum conservations to predict the temperature, velocity, pressure of fluids. The first step in CFD involves the characterization of the domain (space) that contains the fluid system. Subsequently, the domain is divided into discrete elements (volumes) known as meshing

and the mesh size depends on the size of the domain and accuracy required. To a certain degree, the finer the mesh, the more accurate results, however, fine meshes come at higher computational cost (Tang et al. 2011). After mesh creation, the next step is simultaneously solving both the Navier-Stokes equation (a mathematical description of the conservation of momentum) and the mass conservation equation, with appropriate boundary conditions imposed, to simulate the flow regime.

CFD can be a useful method for predicting bioaerosol generation, distribution and airborne disease transmission when combined with other methods. Hathway et al. (2011) used CFD to investigate the risk of bioaerosol generation of some non-respiratory disease pathogens. A validation experiment for the simulation showed that the transport of airborne pathogens could be studied using either a particle tracking approach or a passive scalar technique. This would allow for prediction of the pathogen concentrations in air and at the point of deposition. Redrow et al. (2011) combined CFD and probability density techniques to simulate cough jets and droplet nuclei in confined spaces. Their results showed that a 10 μm droplet evaporated to become a 3.5 μm nucleus in in 0.55 s at 80% RH, in 0.3 s at 50% RH, and in 0.25 s 20% RH. They also showed that the droplet temperature decreased rapidly from human body temperature to room temperature, which might affect the viability of any contained virus. Li et al. (2018) demonstrated that supersaturated air exhaled from the respiratory track formed vapor plumes in front of the respiratory track which significantly impeded the evaporation of droplets contained in it. They further showed that in situations where the droplet sizes were reduced by evaporation, both the number and mass concentrations of inhalable pathogens significantly increased and hence posed

an increase in the risk of infection. King et al. (2012) used CFD to simulate the spatial distributions of bioaerosol deposition in indoor environments and also investigated the effects of different room configuration on deposition patterns. They demonstrated that small particle bioaerosols were deposited throughout the room with no clear correlation between the surface concentrations and distance from the source. They further showed that a physical partition separating patients was an effective way to reduce contamination of neighboring spaces. Lai et al. (2012) used CFD to study the deposition of three different groups of bioaerosols with sizes ranging from 1 to 10 μm and experimentally validated their results. They showed that the larger the size of aerosols, the shorter the deposition distance away from the inlet.

Zhu et al. (2011) coupled a CFD-based model with the Wells-Riley equation to numerically assess the risk of airborne influenza infection in public transportation. They showed that air recirculation model with high efficiency filtration posed similar infection risk as non-recirculation in a bus with traditional ventilation bus configuration. They also demonstrated that the risk of infection was significantly lower in a novel ventilation system they proposed. They further showed that air distribution, location of exhaust and seat arrangement affected transmission of influenza between passengers for commonly used mixing ventilation. Li et al. (2015) coupled CFD and a multizone model to simulate the transport and dispersion of pollutants from a bus exhaust to the cabin of a school bus. They reported that concentrations of pollutants were highest when the bus was driven at a medium speed (64 km/h).

So far it has been demonstrated that CFD can be a useful technique to model the generation, transport, distribution and deposition of bioaerosols. However, not much has been reported about

the application of CFD in simulating the behavior of airborne pathogens contained in bioaerosols. Noakes et al. (2004) coupled CFD with a micro-organism inactivation equation to predict the aerosolized concentrations of *Pseudomonas aeruginosa* in UVGI treatment. A good agreement was obtained with experimental data.

So far, the review of literature has shown air ionization as a useful technology for air purification. Its usefulness has been proven by the numerous applications for the removal of particulates from air. However, not much is known of the technology's effectiveness for rendering bioaerosols non-infectious. The effects of different types ions on different types and concentrations of bioaerosols (virus, bacteria, fungi) are still yet to be completely understood and requires further investigation. Specifically, the time dosage of ions required to inactivate bioaerosols remains relatively unknown. Furthermore, the contributory effects of ions towards infectivity reduction either through bioaerosol removal from air or through unique biocidal actions of the ions on the virus is yet to be understood. Additionally, the specific mechanisms by which the ions produce biocidal effects on the bioaerosols remains a gap in knowledge and provides opportunity for research. To help understand the role of ionization in deactivating bioaerosols, this study aims to conduct chamber experiments to determine the effects of ionization on aerosolized virus (Reovirus). A time dosage approach will be utilized to study the effects of negative ions on viral infectivity and airborne virus concentrations. A CFD model will also be used to understand the behavior on bioaerosols subjected to air ionization.

3. Methodology

3.1 Numerical Modelling of Air Ionization and Bioaerosol Behavior

3.1.1 Overall Modelling Processes

Modelling of air ionization is built on the physical processes that govern gas flow, particle (bioaerosol) flow, electric field distribution and charge (ion) transport. These processes interact (or are coupled) with each other during air ionization (Fig. 3.1). Application of a high voltage potential to the corona points produces corona discharge and releases (negative) ions into the air. Collision among the ions produces an electric field while the collision of the ions with neutral molecules generates an electric wind referred to as an electrohydrodynamic/ionic wind (Farnoosh et al. 2011; Vaddi et al. 2020). Ionic wind often occurs near the corona points and the impact of its velocity noticeable near the corona points (Lee et al. 2003). Hence in a large space (drift zone), the ionic wind is not expected to significantly affect the airflow velocity. When bioaerosols are introduced into an air stream, they will collide with ions and become charged. At high electric field intensities, the charged bioaerosols will also follow electric field lines. If the bioaerosols have a velocity less than the air velocity, the air velocity will drive the bioaerosol movement. Furthermore, as the generated ions from the corona points move into the drift zone and attain a steady condition, electrostatic forces are generated, and these forces further act on both the bioaerosols and the gas molecules to alter their trajectories and velocities. In situations when the bioaerosol velocity is higher than the air velocity, the bioaerosols impact the gas molecules, causing increases in the velocity of the air (momentum exchange occurs).

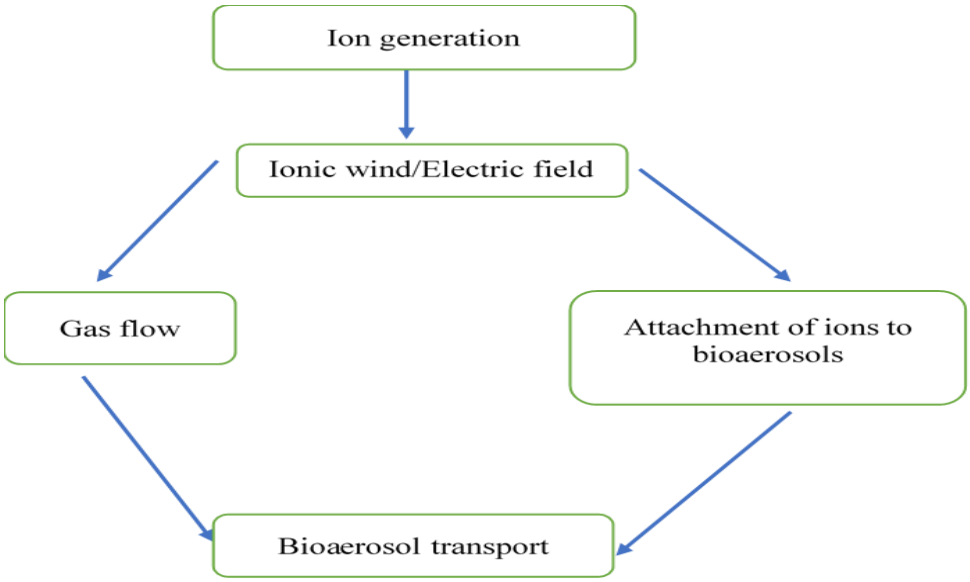

Fig. 3.1 Schematic illustration of the mechanisms involved during air ionization.

Each of the above processes may be described by a governing equation and simultaneous solutions to these equations define the overall behavior of air ionization. Different numerical solution techniques exist for solving coupled systems of equations. For this study the finite volume method (FVM) was chosen to solve the four process equations involved. The FVM was chosen because the technique has been proved to be capable of solving the complex coupled equations. For example, Lobov (2012) employed FVM to study corona discharge electrostatic for the removal of airborne pathogens and recommended it as an efficient method for studying electrostatic charging and its effect on pathogens. A commercial software ANSYS FLUENT (ANSYS, Inc., Canonsburg, PA, USA) was chosen to implement the FVM models in this study. The software was chosen because it is one of the mostly used CFD software packages based on the principles of FVM. ANSYS FLUENT offers an integrated approach for solving the gas phase, the discrete (bioaerosol) phase, the ion transport simultaneously without requiring coupling with another

programs to simulate the overall process of ionization (Skodras et al. 2006; Noakes et al. 2007; Toljic et al. 2012).

3.1.2 Gas Phase Modelling

The first module in modelling the ionization processes is the flow field (gas phase). An accurate representation of the flow field is necessary to determine the behavior of the air flow and its effect on the movement of the ions and the aerosols in air. For this study, the gas (air) phase is considered as an incompressible Newtonian fluid because the pressure changes in the spaces where bioaerosols spread are generally negligible. Consequently, a constant density and viscosity can be assumed. When a gas phase satisfies these stated conditions, the Navier–Stokes and continuity equations can be used to describe the gas flow. The Navier–Stokes equations states that the rate of change of momentum equals the sum of forces on a fluid particle (3.1) (Schneiderbauer and Krieger 2013);

$$\rho_f \left[\frac{\partial \vec{u}}{\partial t} + \vec{u}.\nabla\vec{u}\right] = -\nabla P + \mu\nabla^2\vec{u} + S_T \tag{3.1}$$

where:

P = pressure (Pa)

$\vec{u}$ = gas velocity (m)

μ = viscosity of the gas (m^2/s)

ρ_f = density of the gas (kg/m^3)

S_T = source/sink of the momentum

For an incomprehensible fluid, its density is considered to be constant and therefore conservation of mass can be predicted using equation (3.2) (Schneiderbauer and Krieger 2013);

$$\nabla . \vec{u} = 0 \qquad (3.2)$$

It should be noted that, the gas density is assumed to be not affected by introduction of ions into the chamber because the ion concentration is several orders of magnitude lower than the concentration of gas molecules (under the atmospheric pressure at the sea level, there are approximately 2.5×10^{25} gas molecules per cubic meter of air, while the ions concentration is 10^{14} ions/m^3). Furthermore, air ionization causes little changes in the temperature of the air in the space (chamber), and therefore, the effect of temperature due to ionization is not considered in modelling the fluid behavior. This means that the energy changes due to ionization do not need to be included in modelling.

The rapid and continuous motion of ions into the drift zone creates electrostatic (Coulomb) forces between the ions. Depending on the concentration of the ions generated into the drift zone, the forces generated may be strong enough to affect the airflow (gas phase). In such situations, the electrostatic forces alter the velocity profile of the gas phase. The electrostatic force generated at a location is the product of the ion concentration (C/m^3) and the electric field intensity at the location (N/C) (Choi and Fletcher 1997). In ANSYS FLUENT, this influence on the gas phase can be modelled as a body force and included in the momentum equation (3.1) as source term by means of a user defined function.

3.1.3 Electric Field Modelling

The movement of the ions in the drift zone induces space charges which result in an electric field in the domain. The electric field can be described by Gauss's equation (3.3)(Nikas et al. 2005);

$$\nabla . \vec{E} = \frac{q_e}{\varepsilon_0} \tag{3.3}$$

where:

q_e = space charge density (C/m^3)

ε_0 = permittivity of space (F/m)

$\vec{\mathrm{E}}$ = electric field strength (V/m) or (N/C)

The vector electric field when expressed in terms of the scalar electric potential yields the Poisson's equation (3.5)(Nikas et al. 2005);

$$\nabla^2 \emptyset = -\frac{q_e}{\varepsilon_0} \tag{3.4}$$

$$\vec{\mathrm{E}} = -\nabla \emptyset \tag{3.5}$$

where:

$\emptyset$ = electric potential (V)

Mathematically, the amount of charges acquired by an aerosol particle can be calculated using equation (3.6) (Hinds 1999);

$$q_a = n_c e \tag{3.6}$$

where:

q_a = total charge on the aerosol (C)

n_c = integer number of elementary charges

e = charge an electron carries, which has a value of 1.6×10^{-19} (C)

3.1.4 Ion Transport Modelling

The distribution of ions in the domain (chamber) is dependent on the convective and diffusion components of ion transport. The convective component is mainly due to the ion drift velocity and the gas velocity (Toljic et al. 2012). The ions drift velocity is dictated by the electric field strength and the ion mobility. As the (negatively) charged bioaerosols and negative ions move towards the ground surfaces, an electric current is created with a density defined by equation (3.7)(Noakes et al. 2007, Toljic et al. 2012);

$$\vec{J} = C_0\left(b\vec{E} + \vec{u}\right) - D_i\nabla C_0 \qquad (3.7)$$

where:

$\vec{J}$ = current density (A/m^2)

C_0 = concentration of negative ions (#/m^3)

D_i = diffusion coefficient of the ions (m^2/s).

$b =$ mobility value (m^2/V/s).

Under the steady state conditions, the current density must satisfy the charge conservation law (Equation (3.8).

$$\nabla.\vec{J} = 0 \qquad (3.8)$$

Hence equation (3.7) becomes:

$$\nabla . C_0\left(b\vec{E} + \vec{u}\right) - \nabla . (D_i \nabla C_0) = 0 \tag{3.9}$$

When the concentration of ions produced by a corona electrode is unknown, a way to estimate the charge concentration produced on the surface of a corona wire is by using Peek's formula (Equation (3.10)(Skrodas et al. 2006);

$$E_P = 3.1 \times 10^6 \left[1 + 0.0308 \left(\frac{\delta}{r_o}\right)^{1/2}\right] \tag{3.10}$$

$$\delta = \frac{T_O}{T} \times \frac{P}{P_O} \tag{3.11}$$

where:

E_P = Peek's electric field value for inducing corona discharge (V/m)

r_o = radius of corona wire (m)

T_O = standard temperature (293K)

P_O = standard atmospheric pressure (101325 Pa)

T = gas temperature (K)

P = gas pressure (Pa)

The procedure of using Peek's law for estimating the concentration of ions produced by a corona electrode is outlined as follows. An initial guess is made for the concentration of ions on the electrode at the start of simulation, while the value of the space charge is taken to be zero at all locations within the drift zone. As simulation progresses, the value obtained for the space charge density on the electrode surface is iterated until the electric field on the electrode is sufficiently close to Peek's value. However, in situations where the ion concentration produced at the electrode

is known, the ion concentration can be imposed as a boundary condition while the transport of the ions from the electrode into the drift zone can be modelled using a transport equation (Noakes et al. 2007). In this study, A Neumann boundary condition was imposed to generate a constant ion generation rate (flux) at the electrode boundary. The Neumann boundary condition specifies the values in which the derivative of a solution is applied within the boundary of the domain. This imply fixing the derivative of the unknown at specific nodes (Galbusera and Niemeyer 2018). For this study, a constant concentration of ions was generated per unit time at the ionizer into the chamber and therefore for simulation purposes, the ion generation into the chamber was modelled as a Neumann boundary condition. With the concentrations at the ionizer boundary determined, the transport of the ions into the drift zone was modelled using equation (3.12). Specifically, the electric potential distribution in the domain was modelled using a scalar transport equation in ANSYS FLUENT through a User Defined Scalar (UDS) to implement equation (3.12) in the CFD model (ANSYS FLUENT 2009).

$$\frac{\partial \emptyset_k}{\partial t} + \frac{\partial}{\partial x_i}\left(\rho u_i \emptyset_k - \Gamma_k \frac{\partial \emptyset_k}{\partial x_i}\right) = S_{\emptyset_k} \tag{3.12}$$

where:

$\emptyset_k$ = scalar quantity to be determined (in this case electrical potential)

$S_{\emptyset_k}$ = source term for the scalar (potential value at the boundary, -28 kV in this study)

Γ_k = diffusion coefficient

Equation (3.12) represents one directional flow. The first term is on the left-hand side of the equation represents the variation of the electrical potential with time. The first term in the brackets

is the convection (flux) term and the second term the diffusion term. The term on the right-hand side is the source term, which is the applied voltage of -28 kV in this study.

To use ANSYS FLUENT to simultaneously model the transport of ions equation (3.12) and electric potential equation (3.5), two UDF's (sub-routines) were written in a programmable language (C, C++) and incorporated into the program by means of macros (shown in Appendix A). It should be noted that the modified flux terms in equation (3.12) is not in the built-in equations in ANSYS FLUENT and therefore must be incorporated into the program through a UDS to predict the distribution of ions in the domain (The details for adding terms are described in section 3.1.8).

3.1.5 Aerosol Charge and Movement Modelling

An aerosol acquires charges (become charged) by means of collision with the negative ions in the air. As charges build up on the aerosol, a local electric field is formed around the aerosol that tend to repel ions. As time progresses, the local electric field becomes stronger and fewer ions would have enough velocity to overcome the electric field force; hence the aerosol charging rate reduces significantly with time, and the number of charges acquired by an aerosol eventually reaches a maximum value. The ion velocity is dependent on the strength of the electric field in the vicinity of the aerosol. "Field charging" occurs when there is a very strong electric field (greater than 500 kV/m) in the proximity of the aerosol and with ion concentrations greater than 10^{13} (Hinds 1999), whereas "diffusion charging" occurs at lower electric field intensities (Hinds 1999). Saturation charging under field charging occurs in 3 s (Hinds 1999). In this study, the number of ions attracted to an aerosol is modelled by using the field and diffusion charging models presented

by Hinds (1999), with equation (3.13) for diffusion charging and equation (3.14) for field charging.

$$n_o = \frac{d_p kT}{2K_E e^2} \ln\left[1 + \frac{\pi K_E d_p \bar{c_i} e^2 C_o t}{2kT}\right] \tag{3.13}$$

$$n_o = \left(\frac{3\varepsilon_o}{\varepsilon_o + 2}\right)\left(\frac{\vec{\mathrm{E}} d^2}{4K_E e}\right)\left(\frac{\pi K_E e b C_o t}{\pi K_E e b C_i t + 1}\right) \tag{3.14}$$

where:

n_o = number of ions attached to a bioaerosol (#)

d_p = diameter of the bioaerosol (m)

t = resident time of bioaerosol (s)

C_o = ion concentration (#/m^3)

$\overline{c_i}$ = mean thermal speed of ions (240 m/s at STP)

k = Boltzmann constant (1.38064852 × 10^{-23} m^2 kg s^{-2} K^{-1})

K_E = constant of proportionality (9×10^9 N.m^2/C^2).

$\vec{\mathrm{E}}$ = electric field intensity (V/m)

e = charge on an electron (1.602 x 10^{-19} C)

ε_o = Permittivity of space (8.85418782 × 10^{-12} F/m)

Hinds compared the predictions of his models to a more complex aerosol charging model presented by Lawless (1996) and observed that, for aerosols with aerodynamic diameters between 0.05 to 40 μm and ion concentrations greater that 10^{12} ions/m^3, the model predictions agreed

closely. Furthermore, although other charging models have been presented by several investigators (Pauthenier and Moreau-Hanot 1932; White 1963; Cochet 1961; Fuchs 1963 ; Chang 1981; Fjeld and McFarland 1989 ;Lawless 1996; Talaie 2005), the output from those models is the total amount of charge accumulated on a particle and therefore requires a further conversion to obtain the number of ions (charges) acquired by an aerosol. Hinds models directly predict the total number of ions attached to an aerosol at a specified time.

Bioaerosol movement tracking in this study was performed using the Lagrangian approach. Specifically, large number of particles which are dispersed in a flow field is tracked by computing the individual particle trajectories at specified time intervals (Grigoriadis and Kassinosa 2009). Considering three forces (gravitational, drag and electrostatic forces) acting on a charged bioaerosol, the trajectory of the bioaerosol can be predicted using equation (3.15) (ANSYS FLUENT 2009);

$$\frac{d\vec{u}_a}{dt} = \vec{F}_D + \frac{\vec{g}_i(\rho_p - \rho_f)}{\rho_p} + \vec{F}_x \qquad (3.15)$$

where:

$\vec{u}_a$ = velocity of the bioaerosols (m/s)

$\vec{F}_x$ = external force exerted on bioaerosol (electrostatic force in this case) (N)

$\vec{F}_D$ = drag force per unit particle mass due to relative velocity between the aerosols and gas phase ($\vec{u} - \vec{u}_a$).

For particle Reynolds numbers much smaller than unity (in the Stokes drag regime), the modified Stokes drag force can be calculated by equation (3.16) (Ounis et al. 1991):

$$\vec{F}_D = \frac{3\pi\mu d_p}{C_c}(\vec{u} - \vec{u}_a) \tag{3.16}$$

where:

μ = viscosity of gas

C_c = Cunningham slip factor to account for the discrete molecular nature of gas at the submicron level.

In ANSYS FLUENT (2009), the Cunningham factor is calculated by equation (3.17):

$$C_c = 1 + \frac{2\lambda}{d_p}\left[1.257 + 0.4e\left(\frac{-0.55d_p}{\lambda}\right)\right] \tag{3.17}$$

where:

λ = the molecular mean free path of the gas phase.

The electrostatic force acting on a bioaerosol is calculated by equations (3.18)(Noakes et al. 2007);

$$\vec{F}_x = q_a\vec{\mathrm{E}} \tag{3.18}$$

where:

q_a is as defined in equation (3.6)

3.1.6 Simulation implementation in Fluent

The domain (chamber) to be modelled was first discretized using a 3-D mesh to obtain control volumes of different sizes (hexahedral cells) (Table 3.1). The domain dimensions matched exactly the physical size of the chamber used for the experiment (0.3 m × 0.8 m ×0.55 m) (x, z and y respectively) (Fig.3.2). Simulation tests were conducted to determine the effect of the control

volume size (meshing) on the average air flow in the chamber. For all the control volume sizes evaluated, the same inlet velocity of 1.5 m/s was used. The average gas velocity in the chamber at the steady state condition was compared among the different sizes of the discretized control volumes. The control volume size at which the average velocity in the chamber began to converge towards a value was chosen as the optimal control volume (meshing) to be used for this study. The results showed that for all the simulations conducted; the average chamber velocities began to converge to a value for a control volume size of 1×10^{-6} m^3 (1 cm^3) (Table 3.1). Therefore, a control volume of 1×10^{-6} m^3 was selected for all the simulations. With this control volume, the domain (chamber) was discretized into a total of 132,0000 cells .

Table 3.1 Discretized chamber (domain) showing control volume sizes and corresponding average gas velocities obtained in the chamber for simulations with inlet velocity of 1.5 m/s.

Mesh element size (m)	Control volume size (m^3)	Total number of control volumes obtained for the chamber	Average gas velocity obtained in the domain at the steady state
7×10^{-3}	3.43×10^{-07}	384840	0.11
9×10^{-3}	7.29×10^{-07}	181070	0.11
1×10^{-2}	1.00×10^{-6}	132000	0.12
3×10^{-2}	2.70×10^{-5}	4889	0.28
5×10^{-2}	1.25×10^{-4}	1056	0.35
7×10^{-2}	3.43×10^{-4}	385	0.53
1×10^{-2}	7.29×10^{-4}	181	0.54
1×10^{-1}	1.00×10^{-3}	132	0.72

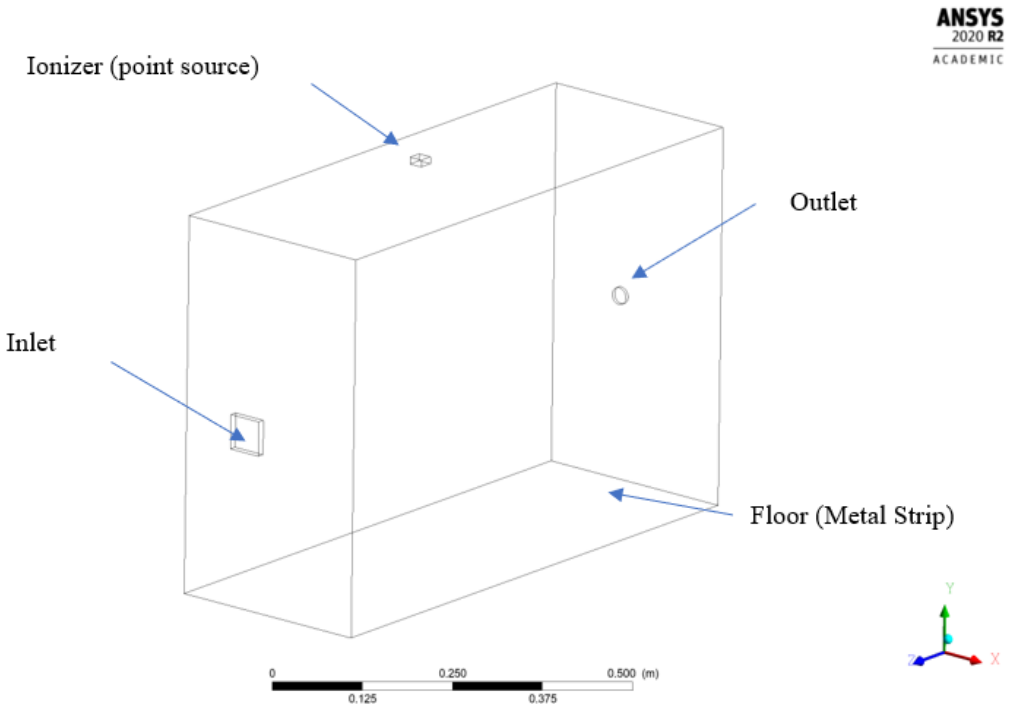

Fig.3.2 Schematic of chamber used for simulation (drawn to scale). x, y, and z represent the width, height and length directions, respectively.

The quality of meshing used to discretize the domain is critical to obtaining accurate solutions of CFD simulations of airflow. For this study, two criteria; namely skewness and orthogonality, were used to evaluate the mesh quality (Moraes and Lage 2013). Skewness determines how close to ideal (equilateral or equiangular) a face or cell is. Table 3.2 shows the criteria used for evaluating the skewness.

Table 3.2 Criteria used to evaluate the skewness of the generated mesh.

Value of Skewness	Cell Quality
1	Degenerate
0.9 - <1	Bad
0.75 - 0.9	Poor
0.5 – 0.75	Fair
0.25 – 0.5	Good
> 0 -0.25	Excellent
0	Equilateral

Source: ANSYS FLUENT (2016)

Orthogonality relates to how close the angles between adjacent cell faces (or adjacent cell edges). The metric relates the angle between the vector that connects two control volume nodes (or mesh) and the normal vector for each integration point surface associated with that edge. The worst cells have orthogonal values closer to zero and the best cells have values closer to one (ANSYS FLUENT 2016). The obtained skewness values ranged from 0.17 to 0.33, with the highest value of 0.33 in just one cell near the corona point (Fig. 3.3). An orthogonality value of 1 was obtained in all cells within the domain. Based on the skewness and orthogonality values obtained, it was concluded that the mesh was sufficiently good to be used for the simulations.

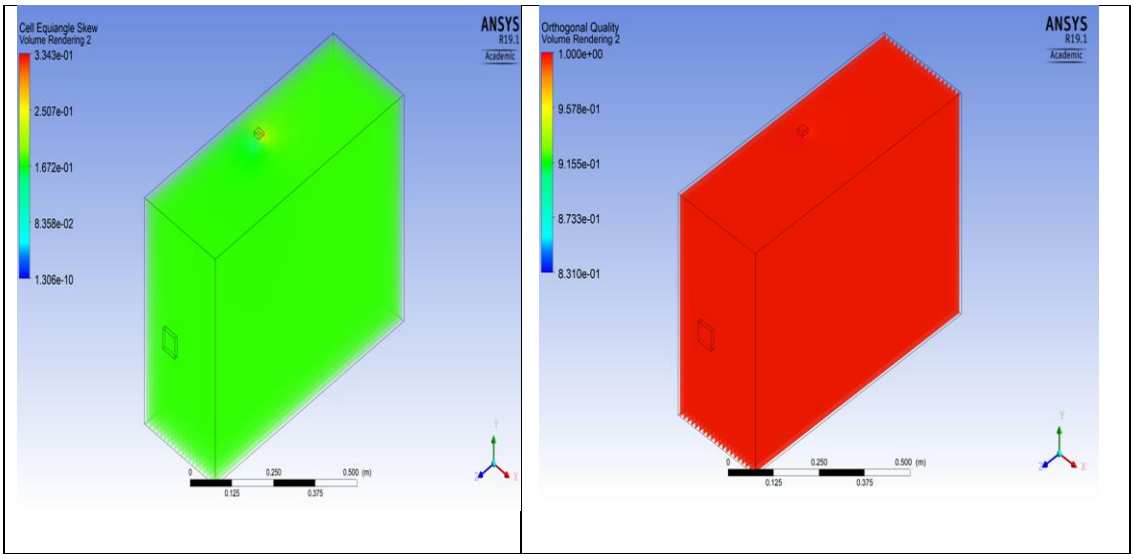

Fig. 3.3 Skewness and orthogonality values obtained for the mesh generated (132, 000 cells).

3.1.7 Boundary conditions

Five boundaries, namely the inlet, the outlet, the ionizer source, the chamber walls, and the grounded electrode, were assigned certain conditions for the simulations based on the physical conditions of each boundary in the test chamber. The defined boundary conditions included the air velocity, the electric potential, the bioaerosol fate, and the ion flow (Table 3.3). Air entered the test chamber at a fixed rate, and therefore the inlet was assigned a constant gas velocity. The outlet was exposed to the atmosphere and was assigned a constant pressure (10100 Pa). This outlet was created to closely match the location around the entry point of the ionizer ground cable into the chamber. The ionizer was energized by a -28kV power source to produce ions by corona discharge and therefore, it was defined as a point of constant electric potential (-28 kV) for the electrical field and a measured ion source (1.9×10^{14} ions/s) for ion flow. The electric potential and ion flow at all other boundaries were specified to be zero. The grounded electrode covered the floor area of the

chamber (0.24 m^2) and it was considered to be a bioaerosol sink (trap), while all the chamber walls were considered to be reflective to bioaerosols (bioaerosols would bounce back to the air when they hit the walls). No slip velocity condition was imposed on the walls of the chamber, meaning the gas velocity at the walls was zero. The inlet velocity, the electric potential, the bioaerosol concentrations and the ion generation rates used for the simulations were based on values obtained from the actual tests conducted in the chamber.

Table 3.3 Boundary conditions for simulations of air ionization in the simulated chamber

	Velocity(m/s)	Electric potential	Bioaerosol Fate	Ion Flow
Inlet	X=1.5 m/s	$\partial\emptyset/\partial n = 0$	Reflect	$\partial C_0/\partial n=0$
Walls	0	$\partial\emptyset/\partial n = 0$	Reflect	$\partial C_0/\partial n=0$
Ionizer Source	0	$\emptyset$=28kV	Reflect	$\partial C_0/\partial n= 1.9\times10^{14}$ (Ion flux)
Grounded Electrode	0	$\partial\emptyset/\partial n=0$	Trap	$\partial C_0/\partial n=0$
Outlet	Pressure	$\partial\emptyset/\partial n=0$	Reflect	$\partial C_0/\partial n=0$

3.1.8 User Defined Functions

As discussed in 3.1.4, some physical processes involved in air ionization are not standard processes in ANSYS FLUENT, and therefore they must be incorporated into the simulation model by means of UDF's. Table 3.3 summarizes the UDF's and the complete source codes are attached in Appendix A. Specifically, the UDF's were coded in a programming language (C++) and subsequently compiled. After compilation, the UDF's were integrated into the ANSYS FLUENT model to simulate all sub-processes during ionization. The various UDF's could be activated or deactivated through either the Graphical User Interface (GUI) or Text User Interface (TUI) of the program. UDF's were written to perform the following functions:

i. Calculate the momentum source terms (Equation (3.1)

ii. Calculate the source terms for the electric potential (Equation (3.4)

iii. Predict the electric field intensity (Equation (3.5)

iv. Calculate the ion concentration (Equation (3.9)

v. Calculate the electric potential (Equation (3.12)

vi. Calculate the number of charges acquired by a bioaerosol (Equation (3.13)

Table 3.3 UDF's compiled for the simulation of air ionization

UDF's	Function
DEFINE_ SOURCE	Estimate the x, y, z source term for the momentum equation. Estimate the source terms for the Poisson equations
DEFINE_INIT	Initialize bioaerosol memory and create names
DEFINE_DPM_INJECTION_INIT	Initialize bioaerosol velocity and temperature equal to the gas phase
DEFINE_ADJUST	Estimate x, y, z electric field intensity Estimate Eulerian variables from Lagrangian (steady state situations)
DEFINE_DPM_SCALAR_UPDATE	Estimate the number of ions attached to a bioaerosol
DEFINE_DPM_BODY_FORCE	Estimate the electrostatic forces acting on the aerosols
DEFINE_EXECUTE_ON_LOADING	Set user defined scalar and memory names

3.1.9 Bioaerosol injection

In ANSYS FLUENT simulations, the bioaerosol transport was implemented using the Discrete Phase Model (DPM) function, which is based on the Lagrangian dispersion theory (Equation (3.15). The bioaerosols introduced into the domain were assumed to be monodispersed

with an aerodynamic diameter 0.5 μm, which was based on the distribution of aerosol sizes measured in the chamber experiments. A narrow range of size distribution (0.3 to 0.8 μm) was measured in the chamber tests, with a mean of 0.5 μm. The file injection feature of ANSYS FLUENT was used to inject bioaerosols at the discretized nodes of the chamber. This was achieved by creating a text file in which the concentrations of the bioaerosols were specified at the nodes. The file was subsequently coupled to DPM to first set the initial concentrations of bioaerosols in the domain, and then, the DPM was used to track the bioaerosol trajectories during the simulation. A single file injection was made to attain a uniform initial concentration of 9.02×10^8 bioaerosols/m^3 (902 #/cm^3) within the domain. The stochastic tracking (random walk) feature of DPM was enabled to model the effect of instantaneous turbulent velocity fluctuations on the particle trajectories. A time step of 0.001s was selected based on the Courant (CFL) condition (Equation (3.19). The CFL condition expresses that, the distance that any information travels during the timestep length within the mesh must be lower than the distance between mesh elements (ANSYS FLUENT 2009);

$$\Delta t \leq u/\Delta x \tag{3.19}$$

where:

Δt = time step length (s)

u = bioaerosol velocity (m/s)

Δx = distance between mesh element (m)

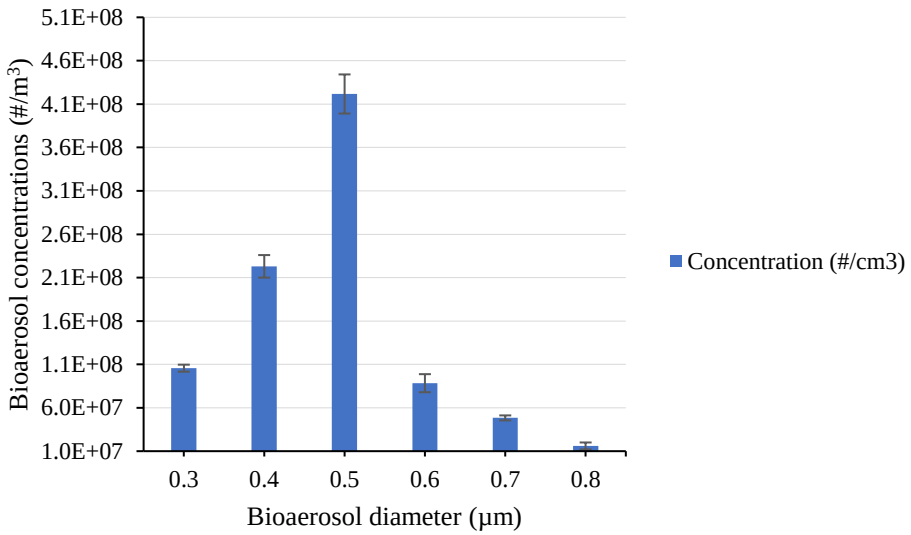

Fig. 3.4 Bioaerosol size distribution obtained from the bioaerosol generation test

3.1.10 Ion transport

The ionizer was modelled as a point source with an ion generation rate of 1.9×10^{14} ions$cm^{-3}s^{-1}$, based on the measured value in the chamber experiment. For the validation tests, an ion counter (AIC 200 million model, AlphaLab Inc., Salt Lake City, Utah) was placed about 1 cm away from the tips of the ionizer (there were only six corona points attached to an electrode) and the concentration of ions was recorded every five seconds over a five-minute period. An average generation rate of 1.9×10^{14} ions$cm^{-3}s^{-1}$ was obtained. As the ions were generated into the domain, they induced space charge and consequently set up an electric field which were calculated by means of UDF (Equations (3.4) and (3.5)) with a potential of -28 kV imposed on the boundary of the ionizer (Dirichlet boundary).

3.1.11 Simulation procedure

The simulation procedure is illustrated in Fig. 3.5. The discretization of the domain (chamber) was performed by using ANSYS Workbench and the discretized domain (mesh) was then input into ANSYS FLUENT. All the UDF'S and UDM'S were defined and linked to the ANSYS FLUENT solver through the Graphic User Interface (GUI). The UDF'S were subsequently compiled. After successful compilation of the UDF'S, the boundary conditions for the gas phase, the electric potential and the ion concentrations were set. The file for the initial bioaerosol distribution in the domain was subsequently hooked to the DPM feature of ANSYS FLUENT. The solver was set to simultaneously solve for velocity of gas flow, the ion concentration and the electric potential within the domain. A convergence criterion was set to 1×10^{-6} for the residuals of the velocity, continuity, electric potential, and ion concentration. The spatial concentrations of the bioaerosols (discrete phase) were monitored over time using the GUI and the simulation ended when all the bioaerosols were removed from the air space. It took about nineteen weeks to simulate a 180-s ionization process on a computer with 4 GB of RAM and a quad-core processor.

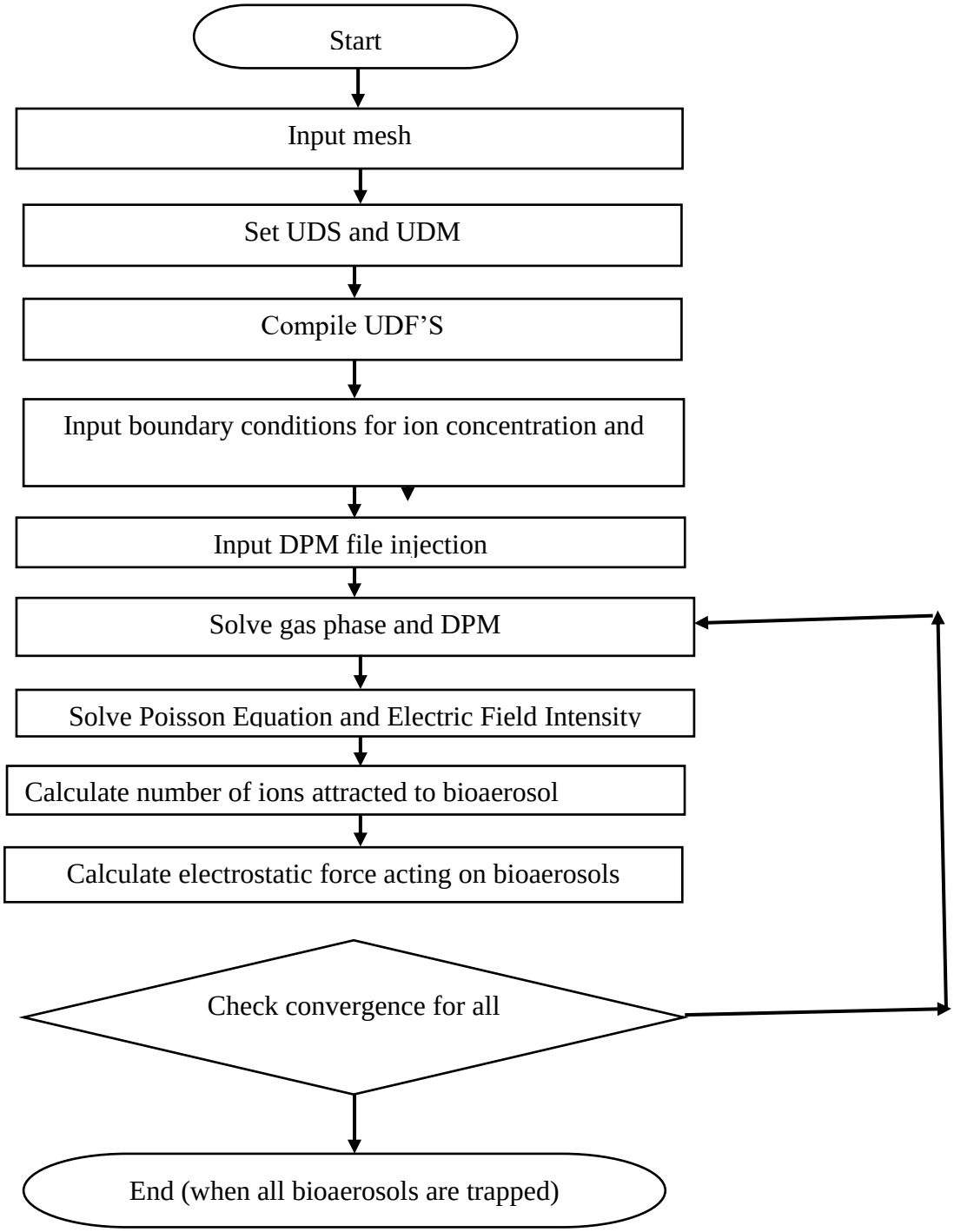

Fig. 3.5 Flow chart used for simulating air ionization for bioaerosol removal

3.2 Chamber Experiments

A chamber experiment was conducted to study the physical removal of bioaerosols from air by air ionization and the biological effect of ionization on viruses. A bioaerosol chamber with internal dimensions of 0.3 m ,0.8 m, and 0.55 m in width (x), length (z) and height (y), respectively, giving a total volume of 0.132 m^3 (132 litres), was built for this study (Fig. 3.8).The chamber was built with Plexiglass while an aluminum sheet was placed on the floor of the chamber and grounded to conduct ions away. A removable door was installed at the front of the chamber for chamber access. A Tygon tubing was installed at the left side of the chamber to serve as the inlet for introducing the bioaerosols into the chamber. A probe was placed inside the chamber to record temperature and relative humidity levels during experimentation. The chamber was placed under the hood of a biosafety cabinet in a virology laboratory (Biosafety level 2) located at the University of Manitoba. The chamber was not ventilated. Air movement in the chamber was caused by a stream of compressed air that delivered aerosols to the chamber and by re-circulation fans. Two sets of chamber experiments were conducted: (i) natural decay of bioaerosols; and (ii) ionization. For the natural decay tests, the ionization system was turned off.

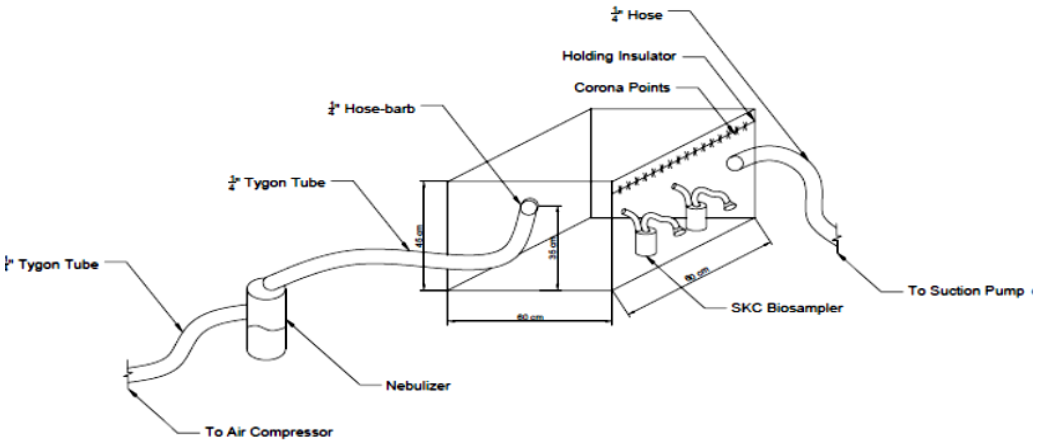

Fig. 3.6 Schematic of the set-up used to conduct experimental chamber tests.

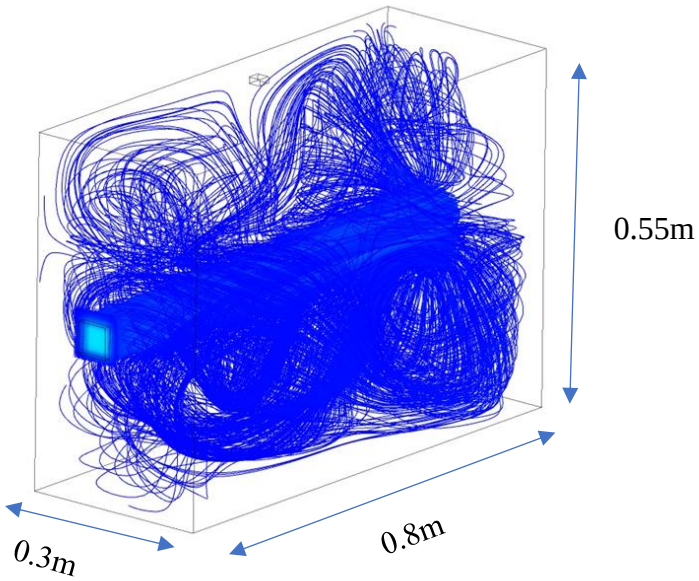

Fig. 3.7 Schematic showing the nature of air mixing in the chamber (Drawn to scale).

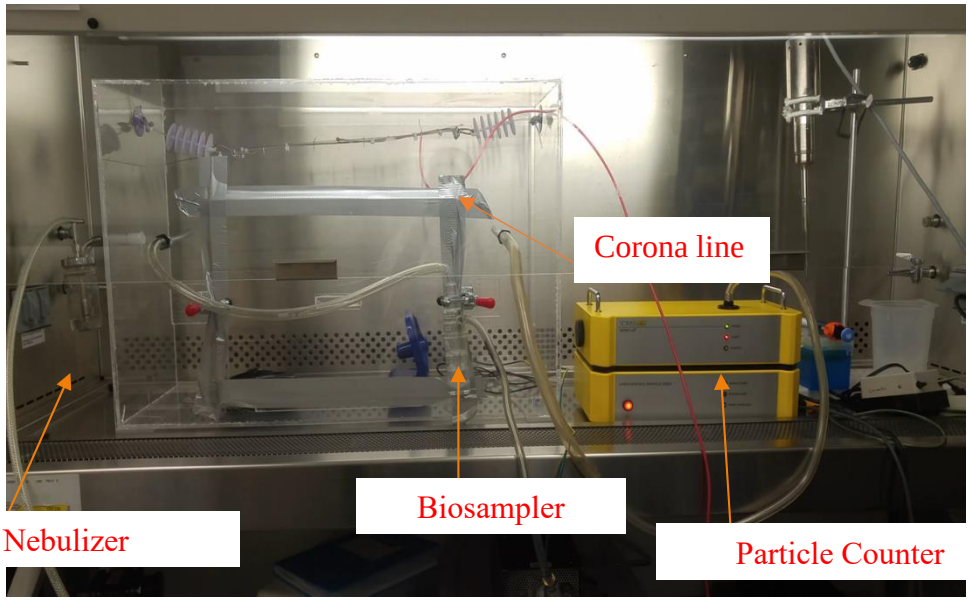

Fig. 3.8 Set-up of the actual chamber used to conduct ionization tests.

3.2.1 Bioaerosol generation

A 6-jet collision nebulizer (CN25, BGI Inc., Waltham, MA) was used to generate liquid bioaerosols in this study. The nebulizer was driven by compressed air from an air compressor and the aerosol generation rate was controlled through a pressure regulator that regulated the pressure of the compressed air. Mammalian Reovirus (MRV) (type 1 Lang) was mixed in the liquid feeding to the nebulizer to create bioaerosols. MRV is a non-enveloped virus which belongs to the Reoviridae family of virus. Although some viruses in the Reoviridae family such as rotavirus are associated with gastroenteritis in infants and younger children, the MRV used in this study was an orphan virus and known not to cause any diseases. Structurally, the MRV is icosahedral in shape and approximately 70 nm in diameter, which could be easily "encased" in aerosols of 500 nm. There are multiple concentric protein capsids in the virus. The innermost capsids serve as transcriptase complex and outermost serve as gene delivery system (Leary et al. 2002). For genome

characteristics, the virus is a double stranded RNA with a genome size between 18-29 kbp. Each virion has 10 segmented genes (Leary et al. 2002). MRV was chosen for this study due to it metastability in air. At room temperature and under the normal atmospheric conditions, the virus does not easily lose its infectivity. MRV was prepared using a standard protocol. On the first day, L929 (mouse) cells were seeded into T75 and incubated at 37 °C in 5% CO_2 flask to attain 60% confluency. After 24 hours, the cells were infected with MRV stock of known titer using a multiplicity of infection (MOI) of 10^{-4}. Infection was carried out by diluting the stock virus in a gel saline. Another cell flask was mock infected using only gel saline to serve as a control for the confirmation of cytopathic effect (CPE) post viral infection. The mock flask also served as a confirmation of successful infection of cells. After infection, cells were incubated at room temperature for 1 hour with a gentle shaking of flask every 10 to 15 minutes. After 1 hour of room temperature incubation, cells were overlaid with Minimum Essential Medium (Eagle Joklik's Formulation) supplemented with 2.5% fetal bovine serum, 2X L-glutamine, amphotericin B and gentamicin. Cells were kept at 37 °C in 5% CO_2 and observed daily until 90% cell death was observed in the infected flask. This was achieved by comparing to the mock flask. The infected flask was freeze thawed twice at -80°C to harvest infectious viral particles from the culture supernatant. The virus was further purified and concentrated by ultracentrifugation in cesium chloride gradients to a concentration greater than10^{11} PFU/mL and subsequently diluted to various concentrations into PBS. Plaque assays were conducted to determine the titers of the diluted concentrations.

Bioaerosols were generated by filling a nebulizer with 40 mL of MRV solution and then air pressure was applied to the nebulizer at 344.7 kPa (50 PSI). The nebulizer was turned on for approximately 7 minutes in each test. At a pressure of 344.7 kPa, an average volume of 4 mL of liquid MRV solution was generated into the chamber. This yielded a bioaerosol generation rate of 34.3 mL/hr, resulting in a nominal bioaerosol concentration of 902 #/cm^3 in the chamber. The aerodynamic diameter sizes obtained ranged from 0.3 to 0.8 µm (Fig. 3.4). The volume of liquid virus remaining in the chamber over time was predicted using the percentage of bioaerosol concentrations measured in the chamber over the same time points. Two small battery-operated fans were placed inside the chamber to circulate both the bioaerosols and ions in order to achieve a uniform distribution. The air velocity at chamber inlet was measured during the introduction of bioaerosols into the chamber with an air velocity meter (TSI 9515 VelociCalc). A velocity of 1.5 m/s was measured at the point of introduction of the bioaerosols. A velocity of 0.2 m/s was also measured at about 5 cm near each speed fan.

A laser particle size spectrometer (particle counter) (APSS; LAP 322, Topas GmbH, Germany) was used to monitor the bioaerosol concentrations within the chamber. The particle counter could measure aerosols with aerodynamic diameters ranging from 0.19 to 40 µm and concentrations up to 10^{11} particles/m^3.

It must be noted that the total bioaerosols measured by the particle counter were less than theoretically estimated (Equations (3.20 and (3.21):

$$B_T = \frac{V_L}{V_{BA}} \tag{3.20}$$

$$B_{TC} = \frac{B_T}{V_C} \tag{3.21}$$

where:

B_T = total number of aerosols generated into the chamber (#)

V_L = volume of liquid generated into the chamber (m^3)

V_{BA} = volume of a single bioaerosol (m^3)

B_{TC} = bioaerosol concentration in the chamber (#/m^3)

V_C = chamber volume (m^3)

With a volume of 4 mL (4×10^{-6} m^3) of viral solution generated into the chamber, a total of 6.1×10^{13} bioaerosols with an aerodynamic size of 0.5 µm were expected in the chamber, and thus a number concentration of 4.6×10^{14} #/m^3 was expected to be measured in the chamber. However, a concentration of 9.02×10^8 #/m^3 (902 #/cm^3) was actually measured in the chamber at steady state. This represented about 6.0 $\log_{10}$ reduction in measured bioaerosol concentrations in comparison with the theoretical calculation. The reduction in measured concentrations could be attributed to several reasons, including the cut-off size of the particle analyzer used in the study. The particle analyzer used in this study had a detection limit as low as 0.2 µm and hence was capable of detecting all particles bigger than 0.2 µm. However, it was possible that a significant

portion of bioaerosols generated into the chamber was below the detection limit of the device and they would not be “measurable” by the particle analyzer. Indeed, the results from the PCR analysis (section 4.6.1) showed that there were no significant losses of virions when air samples taken by the biosampler was used for PCR analysis. This confirmed that the some bioaerosols were not measured by the particle analyzer.

3.2.2 Air movement in chamber

To understand the behavior of the air in the chamber, compressed air was directly introduced through the chamber inlet at velocity of 1.5 m/s in the absence of bioaerosols. The same inlet used to introduce bioaerosols into the chamber was used to introduce the air into the chamber. Considering the relatively small size of the chamber, no ventilation fans were not installed. Hence, the effect of ventilation was not considered for this study. However, the air flow in chamber was enhanced by using two re-circulation speed fans to achieve better uniformation of aerosol distribution.

A smoke test using a Regin colored smoke cartridge was performed to assess the airflow uniformity in the chamber. The smoke cartridge was lit and placed in the chamber through the sampling port, which was sealed immediately after the cartridge was introduced. The movement of smoke was video recorded over a one-hour period. The video was played back on a computer and image frames were taken every five seconds and analyzed for the distribution of airflow patterns in the chamber. Video analysis showed that the smoke completely filled the chamber within 30 s and the smoke became uniformly spread in the chamber (Fig. 3.9).

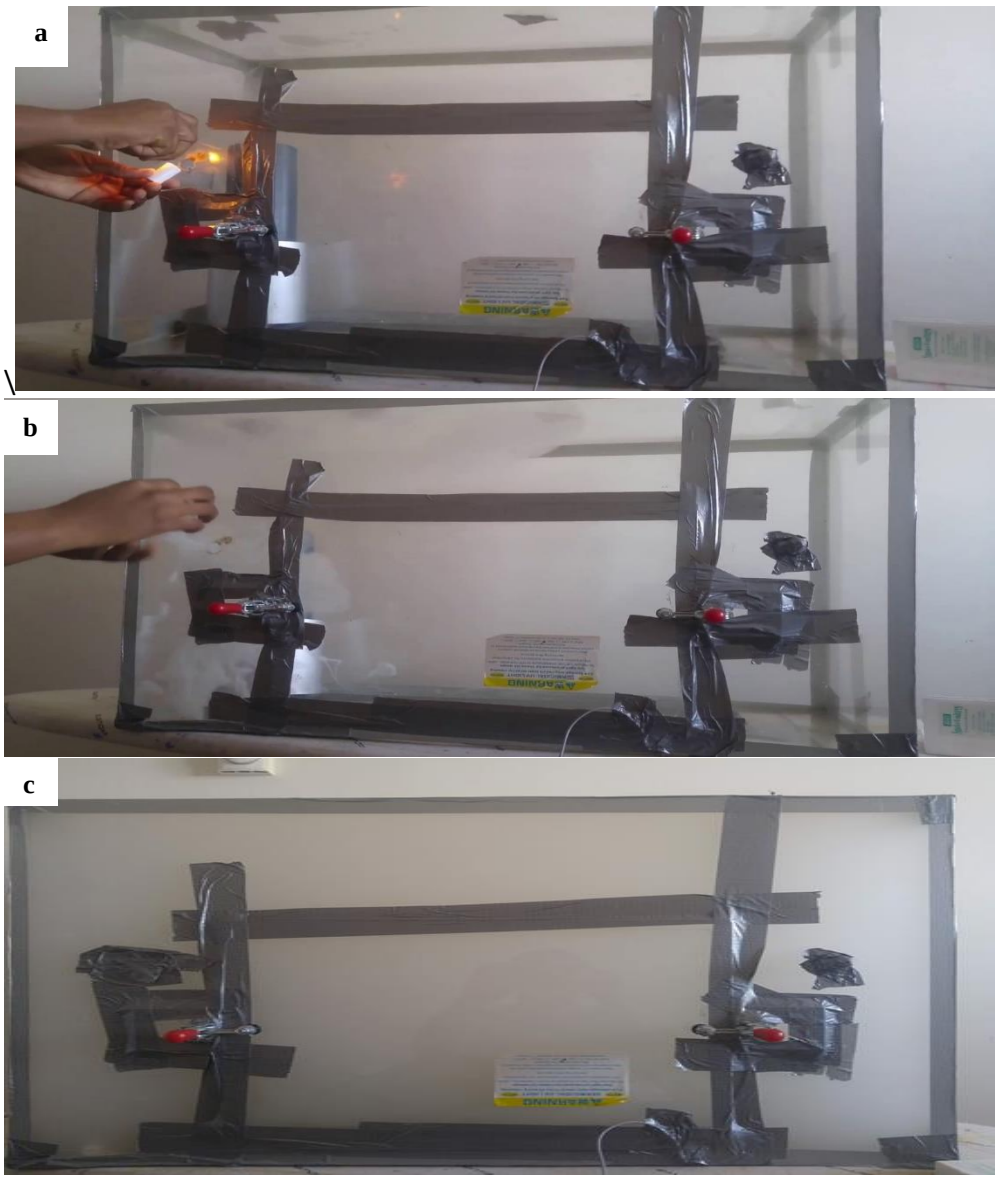

Fig. 3.9 Comparisons of chamber with (a) smoke being introduced (b) chamber partially filled with smoke (metal bowl inside chamber visible) and (c) chamber completely filled with smoke (metal bowl inside not visible)

3.2.3 Bioaerosol sampling

Sampling of the MRV bioaerosols from the chamber was performed using an all glass impinger SKC biosampler (Model No. 225-9594, SKC Inc. Eighty-Four, PA) at pre-defined time points. A Tygon tube was used to connect the biosampler to the sampling port on the chamber. Each biosampler was filled with 20 mL of phosphate buffered saline (PBS) and samples were taken from five pre-determined locations (A1- A5) within the chamber (Table 3.4). Location A1 was located in the center of the chamber; A2 close to the inlet where bioaerosols were introduced into the chamber; A3 the furthest point away from the bioaerosol inlet; A4 near the ionizing source; and A5 near the ground electrode. The reference co-ordinate system used for the chamber experiments was the same as in simulations (Table 3.4). The biosampler was operated by turning on a suction pump (Model No. 228-9605, SKC Inc. Eighty-Four, PA) which drew air from the chamber, bubbling through the PBS solution in the biosampler. Prior to the start of experiment, the biosamplers were calibrated for sampling (flow) rate using a bubble airflow meter (*mini*-BUCK *Calibrator*™ : Model M-30 100cc/min-30LPM). Specifically, the bubble meter readings were taken over a ten-minute period after the suction pump was turned on at the beginning of each test. A sampling rate of 11.5 litres per minute (l/min) was obtained.

Table 3.4 Locations for bioaerosol sampling and ion concentration measurements.

Sampling location	X co-ordinate (m)	Y co-ordinate(m)	Z co-ordinate (m)
A1	0.14	0.27	0.40
A2	0.15	0.27	0.10
A3	0.15	0.27	0.70
A4	0.25	0.50	0.40
A5	0.25	0.10	0.50

3.2.4 Air ionization system

A commercial negative air ionization system EPI (Baumgartner Environics Inc., Olivia, MN) was used in this study. The system comprised of a corona rod electrode measuring 1.4 mm in diameter, with six stainless steel corona points (needles) each measuring 1 mm in diameter and 50 mm in length connected to the corona electrode. The corona line was placed along the chamber length at a height of 0.5 m from the bottom of the chamber and measured 0.6 m in length (Fig. 3.8). The corona line was connected to a power supply that provided -28 kV to the corona points (Fig. 3.10a).

The ion generation rate of the ionization system was measured using a charge plate monitor (CPM) (Model 288b, Monroe Electronics, Nyndonville, NY). The CPM uses voltage-time decay test to evaluate the ionization system. It operates on a start voltage range between 0 and 1000 V with a corresponding decay time up to 999 seconds. Either positive or negative decay tests can be conducted. For this study, a positive decay test was conducted to measure the ion density in the chamber. When the voltage plate of the CPM was turned on, it generated positive ions equivalent to 1000 V on its surface. The time that it took for the voltage of the CPM to reduce from 1000 V to zero was used as an indicator of the negative ion density in the chamber. The smaller the decay

time, the higher negative ion concentration (Alonso et al. 2016). For this study, a decay time of 1 s was obtained for ion generation of 1.9×10^{14} ions/m^3. An ion counter (AIC 200 Million Model, AlphaLab Inc., Salt Lake City, UT)(Fig. 3.10b) was also used to measure the ion concentrations directly at same locations where bioaerosols were sampled. The ion counter was capable of measuring air ions up to a concentration of 1.9×10^{14} ions/m^3. The ion counter was set to the balanced mode settings to enable the determination of the overall net charge present in the chamber (La 2014).

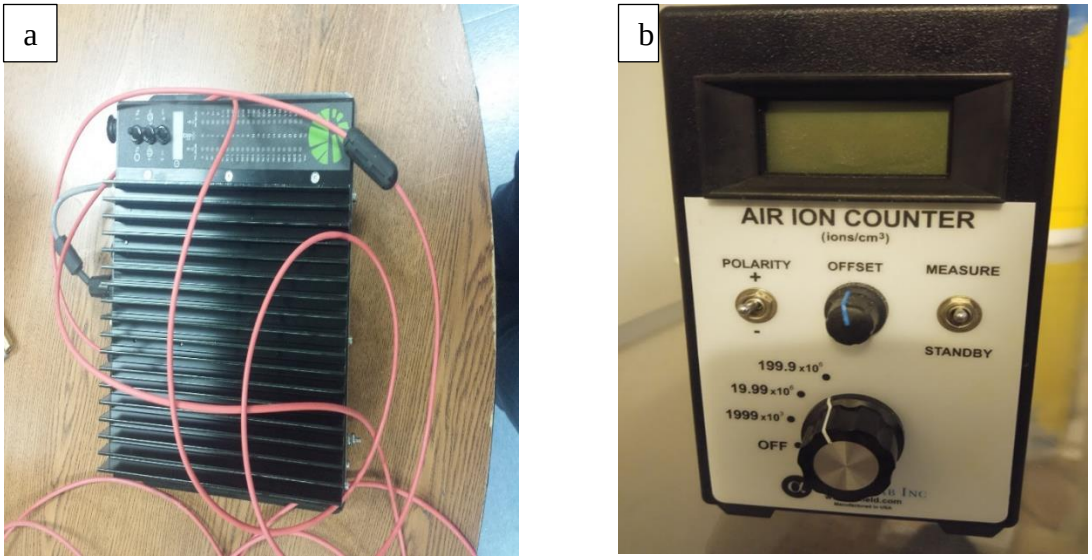

Fig. 3.10 (a) EPI power supply to provide -28kV to the corona points, (b) Air ion counter for measuring ion concentrations in the chamber.

3.2.5 Effect of aerosolization on virus infectivity

When bioaerosols were generated into the chamber, the viruses in PBS solution was pushed through a 6-jet Collison nebulizer at a pressure of 345 kPa. This process of aerosolization might affect the vitality of viruses. Viral plaque assays were performed and only a slight reduction (<7%) in virus infectivity of the stock solution was observed after aerosolization (Table 3.5). It was

therefore concluded that the nebulization (aerosolization) process did not produce any significant effect on the viral infectivity. (SEM indicate the standard error of the mean).

Table 3.5 Reduction in viral infectivity due to the aerosolization process.

Pre Aerosolization (PFU/mL)	Post Aerosolization (PFU/mL ± SEM)	Infectivity loss (%)
2.8×10^9	$2.8 \times 10^9 \pm 5 \times 10^8$	0
2.8×10^8	$2.7 \times 10^8 \pm 4 \times 10^7$	4
2.8×10^7	$2.7 \times 10^7 \pm 7 \times 10^7$	4
2.8×10^6	$2.6 \times 10^6 \pm 5 \times 10^5$	7

3.2.6 Procedures of ionization experiments

Three sets (A, B and C) of ionization tests were conducted to determine the effect of ionization on the bioaerosol infectivity. In each set of experiments, 4 mL of virus solution (in PBS) was generated into the chamber at a rate of 34.3 mL/hr, but different titers of virus stock solution were in three sets of experiments: 2.8×10^7, 2.8×10^8, and 2.8×10^9 PFU/mL for experiment set A, B and C, respectively. Each set of experiments was performed in triplicates. The nebulizer was turned on for 7 minutes to generate bioaerosols into the chamber to achieve the initial concentration of 902 #/cm^3, and then the ionizer was turned on and the measurements of concentration of bioaerosols in the chamber commenced. The aerosol concentration was recorded every five seconds until the concentration in the chamber reached zero. The SKC biosampler was used to take air samples from the chamber at the following concentrations of bioaerosols remaining in the chamber: 812, 631, 451, 90 and 9 #/cm^3. These concentrations respectively represented 90%, 70%, 50%, 10% and 1% of the initial bioaerosol concentration of 902 #/cm^3 (Fig. 3.11). The percentage of bioaerosols remaining in the chamber were also used to estimate the amount of virus solution

remaining in the chamber. For instance, at 90% of bioaerosols remaining in the chamber, a volume of 3.6 mL of the generated liquid (4 mL) virus was estimated to remain in the chamber.

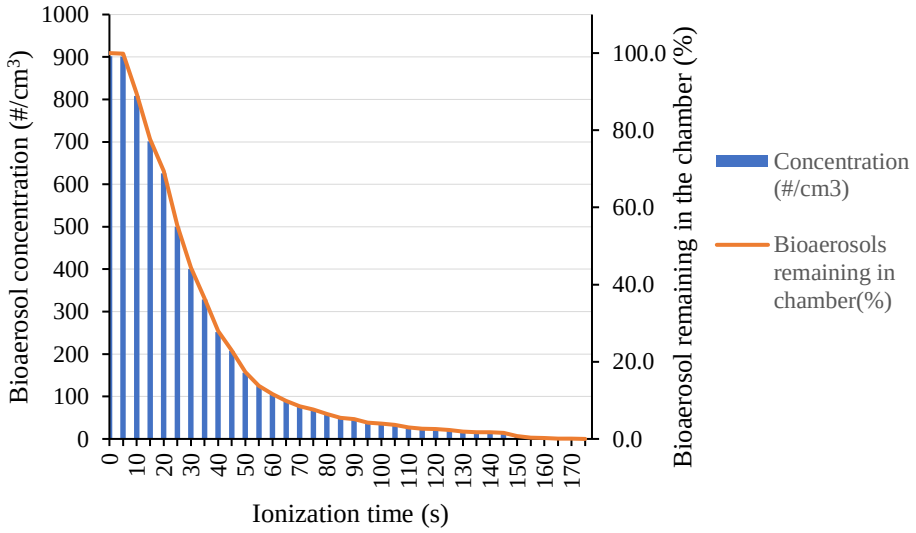

Fig. 3.11 Decrease in bioaerosol concentration in the chamber during ionization in a test with ion concentration of 2.4×10^{13} ions $s^{-1}m^{-3}$.

3.2.5 Cleaning of test apparatuses

All surfaces of the test chamber were sprayed with disinfectant (Virkon, DuPont Disinfectants, United Kingdom) after each experiment. The chamber was subsequently rinsed with water and cleaned with dried towels. Autoclavable items such as the nebulizer and biosamplers were sterilized in an autoclave. The charge plate monitor, the fans, the ion counter and other components that were placed inside the experimental chamber were wiped with a 70% solution of ethanol. The fans were also turned on in the chamber for about two hours after cleaning to aerate the chamber. This method has been shown to be effective in removing all bioaerosols from the

chamber (Zhao et al. 2012). The connecting tubes were washed with bleach (0.53% sodium hypochlorite solution) and rinsed with water afterwards.

3.3 Biological Analysis of Bioaerosols

3.3.1 Viral plaque assays

Viral plaque assays were performed to determine the infectivity of viruses captured from the air in the PBS of the biosampler. During ionization, the change in the measurable bioaerosol concentrations (902, 812, 631, 451, 90, 9 #/cm^3) of the 0.5 µm sized bioaerosols were used as sampling points. The bioaerosol concentration sampling points were used as a clue to detect the total physical percentage of MRV present (100, 90, 70, 50, 10 , 1 %). Plaque assay analysis of air sampled from the sampling points were conducted to determine the viral infectivity at the sampling points. Aliquots of air samples collected by the biosampler from the chamber were kept in 1.8 mL cryogenic tubes and stored in a freezer at -80 ^oC until all the chamber experiments were completed. Plaque assays were subsequently conducted to determine virus titers of the air samples. A 100 µL volume of solution from a cryogenic tube was diluted in 900 µL of gel saline to obtain a tenfold tube dilution. A serial dilution was conducted until a final dilution of 10^{-8} was obtained. A 100 µL volume each from the 10^{-2} to 10^{-8} dilutions was used to infect L929 cells (Leary et al. 2002) in 6 well-plates. After an hour of exposure, the infected cells were overlaid with a mixture of 2x media 199 (supplemented with 5% fetal bovine serum and 4 mM L-Glutamine) and equal volume of agar. The plates were incubated at 37^oC and 5% CO_2 for two days. After two days of incubation, the plates were fed with same mixture and incubated under same conditions for four more days. After

six days, the plates were stained with a mixture of 1x PBS in agar containing a final concentration of 0.04% neutral red and supplemented with streptomycin and amphotericin B. The plates were kept in the incubator overnight and the number of plaques formed were counted on the 7th day after infection. The expected titers from the plaque assays were theoretically estimated from the remaining virus stock solution (determined as % of the initial amount of 4 mL from the aerosol concentration measurement) as follows:

$$V_{iTC} = \frac{V_{BC} \times V_{iST}}{V_{TC}} \quad (3.22)$$

$$V_{AS} = B_R \times T_S \quad (3.23)$$

$$V_{iS} = V_{AS} \times V_{iTC} \quad (3.24)$$

where:

V_{iTC} = virus concentration in the chamber (PFU/m^3)

V_{BC} = volume of viral stock solution remaining in chamber (mL)

V_{iST} = virus stock titer (PFU/mL)

V_{TC} = chamber volume (m^3)

V_{AS} = volume of air sampled (m^3)

B_R = air sampling rate of biosampler (L/min)

T_S = sampling time (min)

V_{iS} = amount of viruses sampled (PFU)

The virus concentration in 20 mL of PBS in the biosampler was determined as follows:

$$V_{iB} = \frac{V_{iS}}{20} \quad (3.25)$$

A volume of 100 µL from the biosampler solution (PBS) was used for plaque assay, resulting a titer as follows:

$$V_{iP} = V_{iB} \times 0.1 \quad (3.26)$$

where:

V_{iB} = virus titer concentration in biosampler PBS (PFU/mL)

V_{iP} = Virus titer obtained from final plaque assay test (PFU/mL)

3.3.2 Virion concentration

RT-PCR analyses were performed to determine the concentrations of viruses captured from the air in the PBS of the biosampler. As discussed in section 3.2.1, it appears most of the bioaerosols generated quickly underwent evaporation and became reduced in size (droplet nuclei). Consequently, significant concentrations of the aerosolized viruses in chamber were below the size detection limit (0.2 µm) of the particle counter used in this study. Therefore, it became necessary to use qRT-PCR to measure the concentrations of the viral RNA as an estimation of the total virions present. The virion concentrations were evaluated at determined time points (10, 20, 30 s).

First, a standard curve was developed to relate the viral concentration to the cycle threshold. A 100% efficient qRT-PCR reaction means the RNA templated doubles after each cycle and has a slope of -3.32. A standard curve with slope between -3.58 to -3.10 is acceptable for a qRT-PCR reaction. To develop the standard curve for MRV in this study, a virus stock solution with a titer of 2.8×10^{10} was serially diluted until a titer of 2.8×10^{6} (PFU/mL) was obtained. For this study, an equivalent VGCN-PFU ratio of 450:1 was used to convert the viral titers to viral

particle concentration in each plaque (VGCN: viral genome copy number). This value is the average of particle-to-PFU ratios obtained over the past few decades in the lab used for this study, where also MRV was cultured. The precise value could not be determined for this study because the required instruments were no longer operational. Based on VGCN-PFU ratio of 450:1, viral particle concentrations of between 1.3×10^9 VGCN/mL and 1.3×10^{13} were obtained. A slope of – 3.25 and an R^2 value of 0.985 were obtained.

3.3.3 RNA extraction and qRT-PCR procedure

A commercially available kit (QIAamp Viral RNA minikit, Qiagen, Netherlands) was used to isolate RNA from the samples. The kit consisted of spin columns, carrier RNA, collection tubes and RNase free buffer. Prior to start of RNA extraction, the working surface of the biosafety hood was disinfected. The RNA extraction process included: (i) addition of a lysis buffer to isolate viral RNA and to inactive RNases which might be present; (ii) addition of alcohol (adjustment buffer) to ensure viral RNA bind to the spin column membranes; (iii) addition of washer buffer to remove contaminants from the membrane; and (iv) addition of an elution buffer to remove RNA from spin column membrane into a solution that was used for RT-PCR. For each sample, 140 µL from the biosampler PBS was added to the reaction mix for RNA extraction. The purity of the isolated RNA was determined using a nano drop spectrophotometer (Thermo Scientific™ NanoDrop 2000). Purity was evaluated based on the absorbance ratio at 260 nm and 230 nm (Desjardins and Conklin 2010). RNA with ratios between 2.0 and 2.2 were deemed pure to be used for the RT-PCR. A volume of 5 µL of the extracted RNA was used for the qRT-PCR analysis. A commercial kit, iTaq™ Universal SYBR® Green One-Step Kit bought from Bio-Rad was used for the qRT-PCR.

The kit consisted of a SYBR® Green dye (reverse transcriptase) and RNase inhibiters. The kit has a successful history for conducting qRT-PCR (Zhang et al. 2011; Picard-Meyer et al. 2015; Bradford et al. 2017). The kit was also chosen because it offers a broad instrument compatibility. Moreover, a one-step kit offers the convenience of PCR without the need of using a separate process to convert the RNA into cDNA. The primer used for the RT-PCR was designed to target the L1-gene segment of the MRV. The sequence for the forward and backward primers were 5'-GCATCCATTGTAAATGACGAGTCTG-3' and 5'-CTTGAGATTAGCTCTAGCATCTTCTG-3', respectively. After they were designed, the primers were ordered from a commercial manufacturer (Integrated DNA technologies, IA). A concentration of 400 nM of each primer was used for PCR. The positive control for the reaction was set up using RNA extracted of the MRV, while the negative control was set up using a nuclease free water. A total volume of 20 µL was used in each well. A 96-well plate was used for each reaction. The qRT-PCR was set up using a CFX Connect Real-Time System (BIO-RAD, Hercules, CA) instrument. The thermal cycle was set as follow: (i) 50 ˚C for 30 minutes (Reverse Transcription); (ii) 95˚C for 15 minutes (Enzyme Activation); and (iii) 40 cycles of 94˚C for 15 seconds (Denaturation) and 60˚C for 60 seconds (Combined Annealing and Extension). The generated standard curve related the cycle threshold value to the initial viral concentration. The threshold value was the cycle in which the concentration of the virus reached a certain level of fluorescence and amplification. The viral genome copy number (VGCN/mL) of each sample was determined using the cycle threshold of each sample and the standard curve (Fig. 3.10).

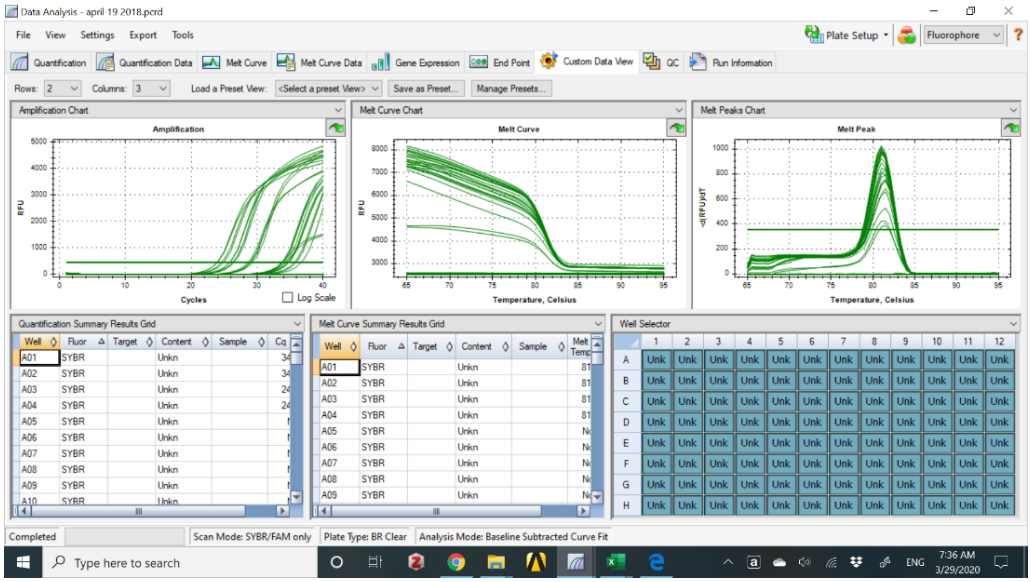

Fig. 3.12 A screen shot of PCR analysis for a MRV sample.

From the PCR results, the virus concentration in air (VGCN/m^3) in the chamber was estimated using the following set of equations.

$$V_{iGC} = \frac{V_{BC} \times V_{iSG}}{V_{TC}} \tag{3.27}$$

$$V_{AS} = B_R \times T_S \tag{3.28}$$

$$V_{GC} = V_{AS} \times V_{iSG} \tag{3.29}$$

where:

V_{iGC} = initial virus genome concentration in air in chamber (VGCN/m^3)

V_{BC} = volume of virus stock solution remaining the chamber (mL)

V_{iSG} = virus stock genome concentration (VGCN/mL)

V_{AS} = volume of air sampled (m^3)

B_R = air sampling rate of biosampler (L/min)

T_S = sampling time (min)

V_{BG} = virus genome in 20-mL of PBS in biosampler (VGCN/mL)

V_{GC} = virus genome copy number in a sample (VGCN)

V_{GC} = virus genome copy number in a sample (VGCN)

The viruses in the air drawn by the biosampler was stripped in 20 mL of PBS, and therefore the virus concentration in PBS was determined as follows:

$$V_{BG} = \frac{V_{GC}}{20} \tag{3.30}$$

where:

V_{BG} = virus genome in 20-mL of PBS in biosampler (VGCN/mL)

A volume of 5µL from the biosampler PBS was used for the RT-PCR, yielding a final viral concentration as follows:

$$V_{iCG} = V_{BG} \times 0.05 \tag{3.31}$$

where:

V_{iCG} = genome concentration obtained from PCR (VGCN/mL)

4. Results and Discussions

4.1 Simulations of Ion Transport

4.1.1 Simulations of airflow in chamber

Simulations were carried out to reflect the two scenarios (A and B) of airflow patterns in the chamber. Scenario A was modelled with an air inlet velocity of 1.5 m/s and without the effect of the recirculation fans. In the experimental study, only air from the compressor was driven into the chamber (scenario A). Scenario B was also modelled with an air inlet velocity of 1.5 m/s, coupled with injection of bioaerosols into the chamber at a velocity of 0.2 m/s and operation of recirculation fans. In the experimental study, bioaerosols were introduced into the chamber together with the air stream at a measured inlet velocity of 1.5 m/s. In the case of scenario B, the average chamber air velocity was measured when the bioaerosols attained steady state of 902 #/cm^3. To attain a similar distribution of bioaerosols in the chamber during simulation, the bioaerosols were introduced into chamber at the nodes of the cells and an initial concentration of 902 #/cm^3 injected at those locations. In the absence of the speed fans, an average air velocity of 0.1 m/s was measured when bioaerosol concentration of 902 #/cm^3 was measured. When the speed fans were introduced into the chamber, velocity values of 0.2 m/s were measured in the vicinity of the two recirculation fans and for simulation purposes, it was assumed that the momentum of the fans were transferred to the bioaerosols, hence bioaerosols were introduced at the nodes with an injection velocity of 0.2 m/s while an air velocity of 1.5 m/s was also imposed at the inlet. It must be noted that the recirculation fans themselves were not simulated due to mesh limitation of the ANSYS FLUENT version used

for this study However based on the measured fan speed value of 0.2 m/s, this velocity was imposed on the bioaerosols during simulation For scenario A, the distribution of air velocities obtained at steady state for most locations in the chamber ranged from 0.02 to 0.1 m/s. However, the air flow reached a peak velocity of 1.2 m/s in a section between the inlet and outlet of the chamber along the Z-axis (Fig. 4.1). For scenario B, the distribution of velocities obtained in most sections of the chamber ranged from 0.05 to 0.25 m/s. However, similar to scenario A, there was a spike in air velocity between the inlet and outlet along the Z-axis (Fig. 4.2), with a peak velocity of 1.5 m/s. An overall chamber average velocity of 0.16 m/s was predicted by the model for scenario B at steady state conditions. The increase in average chamber velocity predicted for scenario B was due to the fan effect. As explained earlier, the velocities of the fans were assumed to have been transferred to the bioaerosols in the chamber at the point of injection. An increase in the injected bioaerosols produced an exchange of momentum between the gas phase and the bioaerosols injected. Hence, the bioaerosols at the point of injection impacted the gas phase, with the momentum transferred from the bioaerosols to the gas molecules.

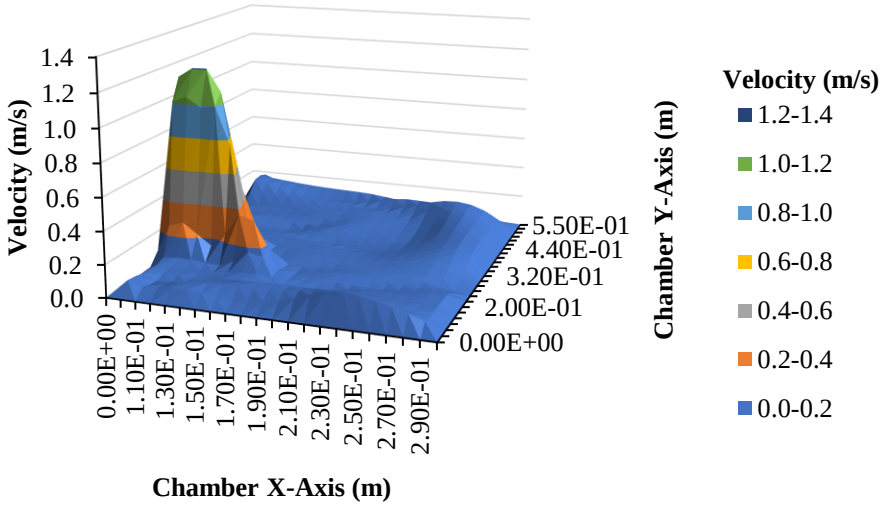

Fig. 4.1 Simulated velocity distribution in the chamber for scenario A on the plane z = 0.4.

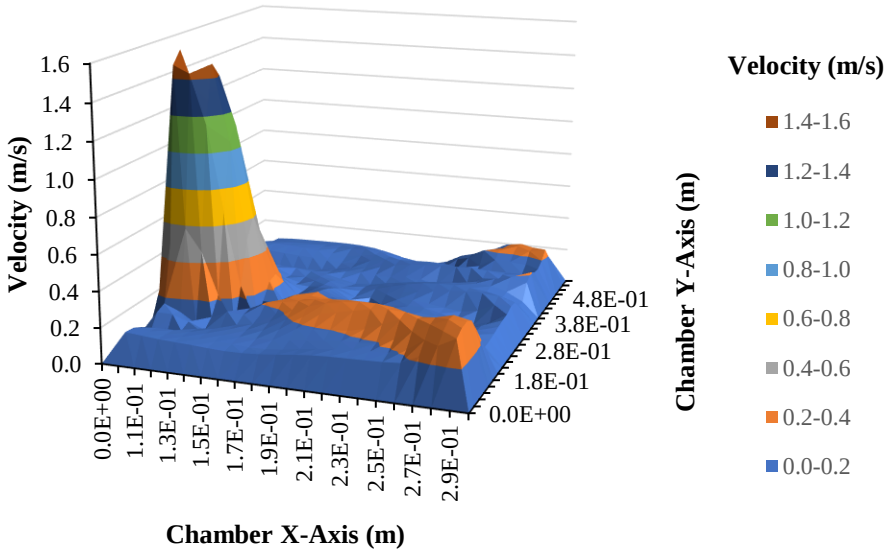

Fig. 4.2 Simulated velocity distribution in the chamber for scenario B on the plane z = 0.4.

The spike in velocity along the z-axis occurred due to the inlet air velocity. An inlet velocity of 1.5 m/s meant that the air travelled along the z-axis for a distance of 1.5 m every second.

However, the chamber length along the z-axis was 0.8 m and so the air introduced into the chamber traveled from the inlet to the outlet in less than 1 s, forming an “air jet” at 1.5 m/s from the inlet to the outlet while other areas in the chamber attained velocities less than 0.2 m/s. (Fig 4.3). The turbulence of the airflow was also investigated by estimating Reynold’s number within the chamber, and the flow was found to be rather laminar in all locations of the chamber (Fig. 4.4), with Reynolds numbers ranged from 1.0 $\times 10^1$ and 2.0 $\times 10^1$. The pressure balance in the chamber also showed that the airflow occurred at atmospheric pressure and there were no pressure losses (101 kPa)(Fig. 4.4)

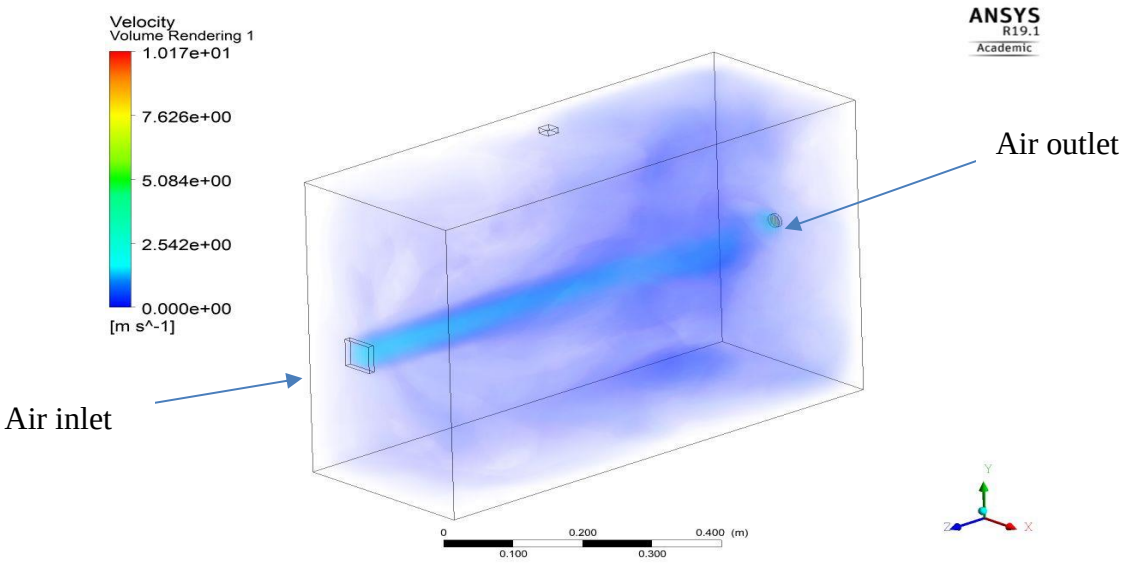

Fig 4.3 A volume rendering showing spatial distribution of air velocity in the chamber (Scenario A).

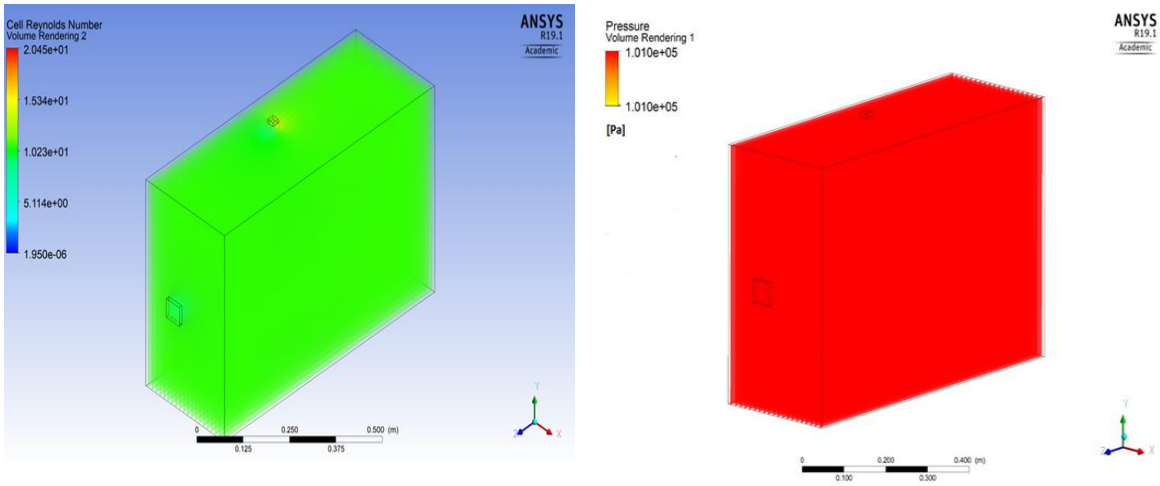

Fig. 4.4 Simulated Reynold's number showing laminar flow in the chamber and simulated pressure showing pressure balance in the chamber to be at atmospheric pressure.

4.1.2 Comparison of simulated air velocities with measurements

The measured velocity in the chamber had a peak value of 0.40 m/s for scenario A and 0.74 m/s for scenario B (Fig. 4.5). Both peak velocities occurred at location A3 (near the chamber inlet). The lowest velocity value of 0.02 m/s for scenario A occurred at locations A4 and A5 (near the ionizer and near the grounded floor of the chamber). In scenario B, the lowest velocity of 0.1 m/s was measured at location A2 (near the chamber outlet). The measured chamber average velocity was 0.10 m/s for scenario A and 0.24 m/s for scenario B. In comparison, the predicted peak velocity of 1.2 m/s was about 3 times higher than the measured value for scenario A; whereas, the lowest velocity predicted the model (0.02 m/s) was the same as the measured value. The difference in the peak velocity between the model prediction and the measurement might be due to the

convergence of the residual of the continuity equation. During the simulation, a steady state condition was imposed when the residuals for the momentum and continuity equations attained a value of 10^{-6}. However, for this simulation while the momentum residuals reached a convergence value of 10^{-6}, the residuals for the continuity never reached 10^{-6}. A decision was therefore taken to accept convergence for the continuity when the residuals reached a value of $10^{-4.}$ While an average velocity of 0.1 m/s was measured for all five locations, the simulated average velocity was 0.06 m/s for the entire chamber. A stricter convergence of 10^{-6} might have resulted in velocities closer to velocities measured in the chamber.

For scenario B, the peak velocity of 1.5 m/s predicted by the model was about twice the measured peak velocity of 0.74 m/s. Similarly, the lowest velocity of 0.1 m/s predicted by the model was twice the lowest velocity of 0.05 m/s measured in the chamber. Similar to scenario A, the residual for the continuity equation did not reach 10^{-6}. The predicted average velocity was 0.16 m/s, which was 67% of the measured velocity averaged over the five locations.

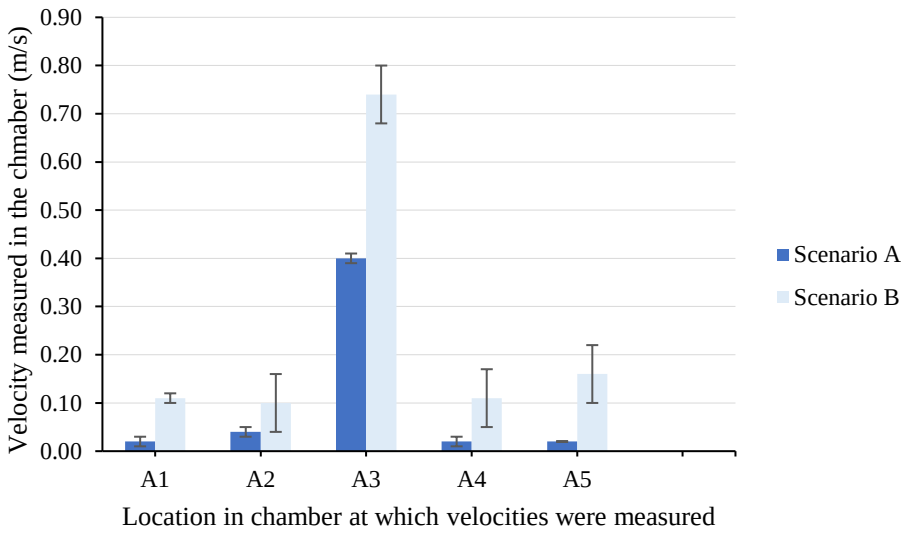

Fig. 4.5 Measured velocity at various locations in the chamber under steady state condition. *Error bars show the standard deviation obtained for three replicates.*

4.1.3 Simulated ion concentrations

Scenario A

The ions were dispersed away from the ionizer (Fig. 4.6). However, the ions clustered in the upper part of the chamber and did not reach the floor of the chamber. Specifically, the ions clustered between 0.1 and 0.3 m in the x-direction; between 0.3 and 0.6 m in the y-direction; and between 0 and 0.8 m in the z-direction. When the steady state condition was reached, an average ion concentration of 3.6×10^{13} ions/m^3 was predicted by the model at the clustered section of the chamber, while the ion concentrations were four orders of magnitude lower outside the clustered section. Given that low air velocities were predicted in the chamber in scenario A (Fig 4.3), ion transport in the chamber was mainly driven by the electrical field generated by the ionizer power source, which was not strong enough to disperse the ions throughout the whole chamber.

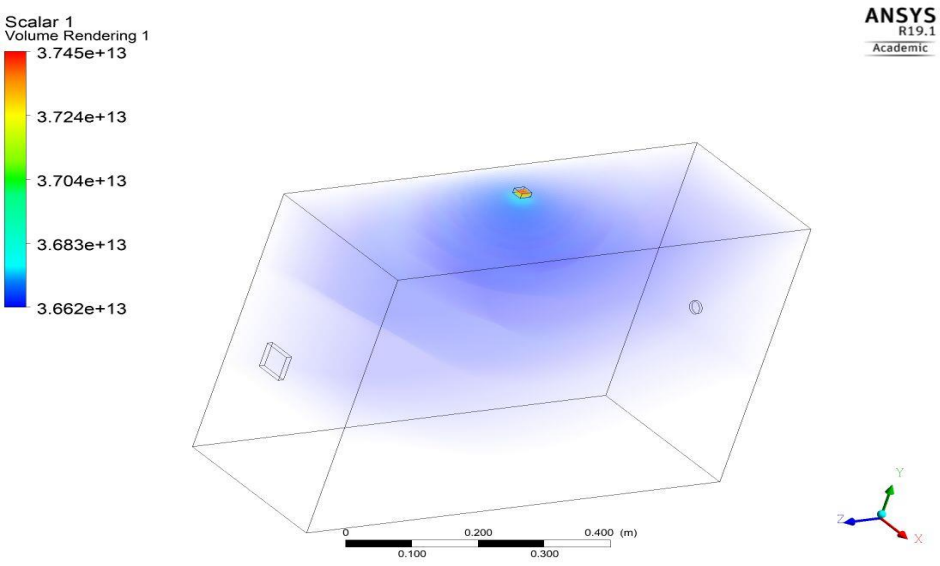

Fig. 4.6 Simulated ion concentration in the chamber at an ion generation rate of 1.9×10^{14} ions $m^{-3}s^{-1}$ in the absence of air circulation fans (Scenario A).

Scenario B

The steady state was reached in 22 s, which was longer than that for scenario A. The movement of the bioaerosols was modelled with an unsteady particle tracking technique and therefore the unsteady motion of the bioaerosols interfered ion movement. Consequently, a consistent flow pattern of the ions could not be established in the chamber at the beginning of ionization. When the steady state conditions were attained in the chamber, a fairly uniform distribution of ions was predicted by the simulation model, with an average ion concentration of 2.9×10^{13} ions/m^3 (Fig. 4.7).

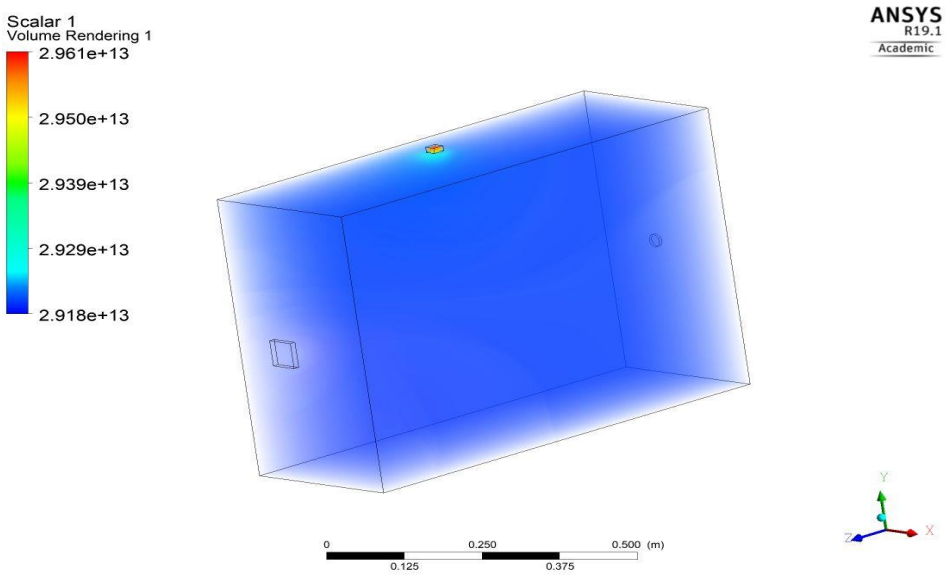

Fig. 4.7 Simulated ion concentration in the chamber at an ion generation rate of 1.9×10^{14} ions $m^{-3}s^{-1}$ for scenario B (with bioaerosols injection simulating air re-circulation fans effects).

4.2 Comparison of ion concentrations between model predictions and measurements

4.2.1 Scenario A

The numerical model was validated against the ion concentrations measured at five locations in the chamber over a time period of 30 s at 5 s intervals. (A concentration of 1.7×10^{14} ions/m^3 ions was measured at location A4 (near the ionizer) at 5 s of ionization and increased slightly to a concentration of 1.8×10^{14} ions/m^3 at 30 s. The concentration remained at 1.8×10^{14} ions/m^3 even after 30 s. Concentrations at other locations also stabilized immediately and did not significantly change afterwards. The ion concentration at location A1 was about an order of magnitude lower than that at location A4, while the concentrations at other locations were several orders of magnitude lower when compared to location A4. The maximum difference in ion

concentration among the locations was observed between locations A5 and A4, with the concentration at location A5 being five orders of magnitude lower than that at location A4 at all time points (Fig. 4.8). The differences in ion concentration among the locations might be attributed to low air velocity in the chamber, which was not strong enough to move ions from the ionizer (source) to other locations. An average air velocity of 0.1 m/s measured in the chamber seemed too low to disperse the ions further away from the ionizer. Overall, the model prediction did not agree closely to measured concentrations. At steady state, an average chamber concentration of 3.6×10^{13} ions/m^3 was predicted by the model however an average concentration of 5×10^{13} ions/cm^3 was measured; hence 28% higher than the predicted.

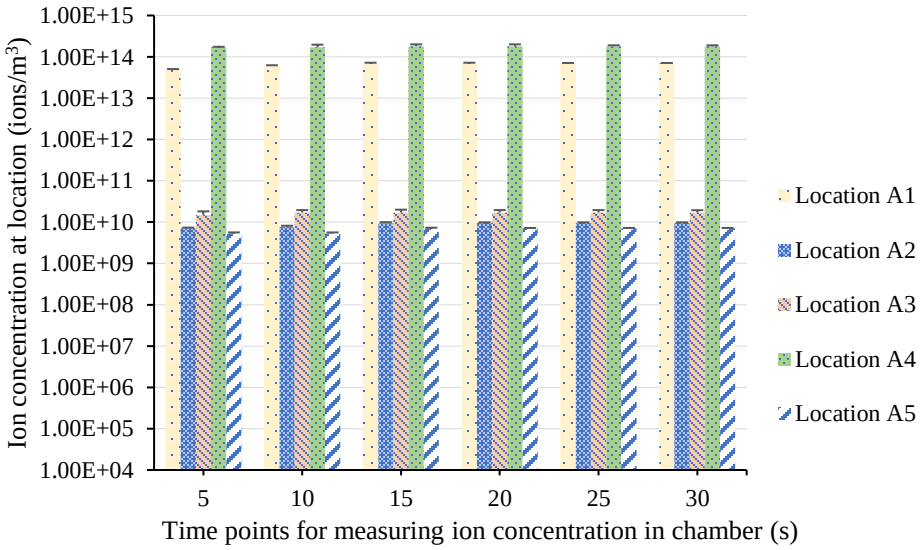

Fig. 4.8 Ion concentrations measured at five locations in the chamber without air circulation (in the absence of fans). *Error bars indicate standard deviation for three replicates.*

4.2.2 Scenario B

With bioaerosols injected into the chamber and two circulation fans to enhance air movement in the chamber, the ion concentrations at all locations steadily increased after ionization

commenced until 20 s when a steady state condition was attained in the chamber (Fig. 4.9). A fairly uniform distribution of ions was obtained after reaching the steady state, with an average concentration of 2.4×10^{13} ($\pm$ 4.5×10^{8} sd), the highest 2.5×10^{10} and the lowest 2.3×10^{10} ions/m^3. Variance analysis (ANOVA) was conducted to compare the ion concentrations between the measurement locations (A1-A5) at every measurement time point and it was found that there were no significant ($P>0.05$) differences in ion concentration between the locations after 20 s when the steady condition was reached.

The ion concentrations predicted by the model were generally in good agreement with the measured values. An average concentration of 2.9×10^{13} ions/m^3 was predicted by the model, while the measured average was 2.4×10^{13} ions/m^3 ($\pm$ 4×10^{9} sd). Although this represented a percentage difference of 21% numerically, the predicted concentration was in the same order of magnitude as the measured value. From the point of view of ion attachment to bioaerosols, this difference of 21% was considered not to be significant. Specifically, for the average bioaerosol concentration discussed in this study (further discussed in section 4.3), a total of 55 ions would be attached to a 0.5 μm bioaerosol for an ion concentration of 2.9×10^{13} ions/m^3, while 54 ions would be attached for the ion concentration of 2.4×10^{13} ions/m^3. From a practical point of view, a difference of one ion would not produce a significant biocidal effect on a bioaerosol. Hence, the model was considered to adequate for predicting ion transport.

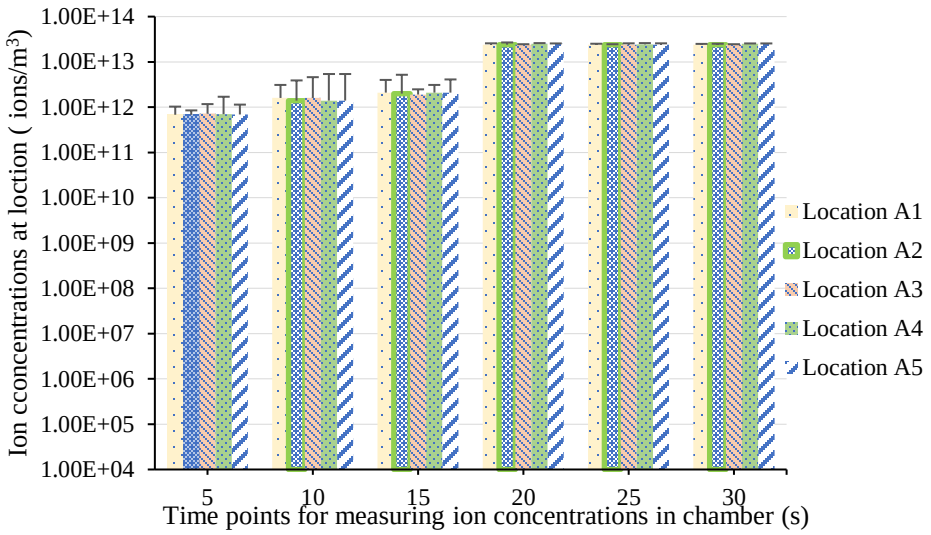

Fig. 4.9 Ion concentration measured at the five locations with bioaerosols present and circulation fans (scenario B). *Error bars indicate standard deviation for three replicates*.

4.2.3 Ion losses

Theoretically, the expected average ion concentration in the chamber at a specified time can be calculated using equation (4.1) if there are no ion losses of ions from the system:

$$C_{ion} = \frac{S_{gr} \times t_g}{C_{vol}} \tag{4.1}$$

where:

C_{ion} = average ion concentration expected in the chamber at a specified time (ions/m^3).

S_{gr} = source ion generation rate (ions/s)

t_g = time of continuous ion generation (s)

C_{vol} = chamber volume (m^3)

However, the measured ion concentrations were lower than the expected values and an example is shown in Fig. 4.10 for a sampling time of 30 s and source ion generation rate of 1.9×10^{14} ions/s. The average ion concentrations measured in the chamber were about four orders of magnitude lower than the calculated concentrations. For instance, at 20 s of ion generation, an average ion concentration of 1.4×10^{17} ions/m^3 was theoretically expected, but an average concentration of 2.0×10^{13} ions/m^3 was measured. This significant difference in ion concentration between the theoretical calculation and the measurement was mainly due to the life span of negative ions in the air. The half-life of negative ions generated by Lenard effect (from a water source) is 60 s and by corona discharge only several seconds (Iwama et al. 2002; Jiang et al. 2018). Futhermore, the ions in the chamber might also collide with the chamber walls and "adsorbed" by the walls. In a smoke test, it was clearly seen that charged smoke particles were deposited onto the chamber walls when the ionizer was turned on for 30 seconds (Fig. 4.11). The underlying mechanism for the deposition of smoke particles to the chamber walls was the attachment of the ions to the smoke particles and electrostatic forces drove the charged particles to the chamber walls.

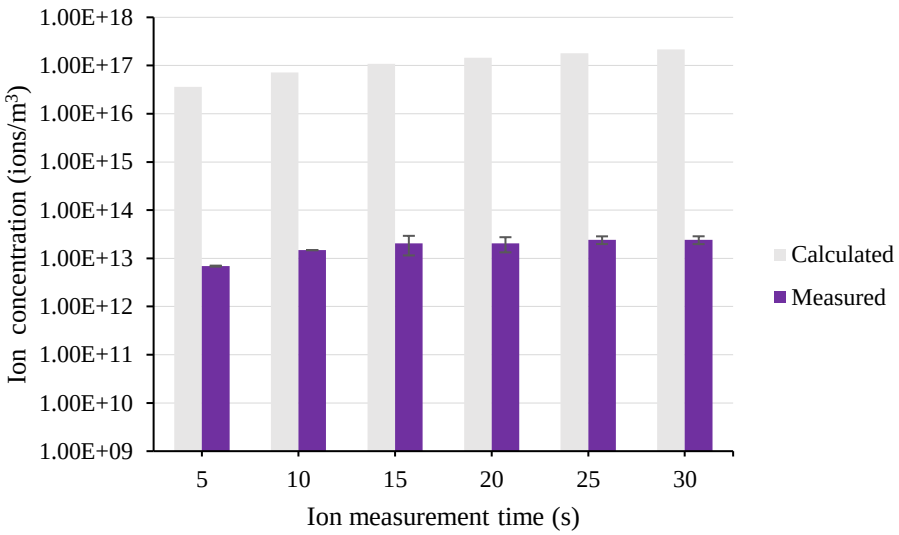

Fig. 4.10 Comparison of the measured ion concentration with the theoretically expected (calculated) ion concentration. *Error bars indicate standard deviation obtained from three replicates of measured ion concentrations.*

Fig. 4.11 Deposition of smoke particles on the chamber walls.

4.3 Electric field, charges of aerosols, and electrostatic forces

The simulated electric field intensity was non-uniform, varying from 3.8×10^{10} to 8.1×10^{10} V/m with the peak intensity at location A2 (near the ionizer) (Fig. 4.12). The non-uniformity of the field intensity within the chamber was expected because the electric potential applied at the ionizing point was modelled as a point source. Specifically, the voltage was fixed at the boundary with a constant value of -28 kV, causing a very high field strength near this point and an electric potential gradient within the chamber. An average predicted electric field intensity of 5.8×10^{10} V/m in the chamber. Based on observations reported in the literature, this field intensity was sufficient for removing airborne particles. Skrodas et al. (2006) modelled an electrostatic precipitator with three corona points which were imposed with boundary potential of 70 kV and the model predicted electric field intensities between 2.50×10^{3} and 5.05×10^{5} V/m at the steady state. They concluded that these field intensities were sufficiently strong to remove aerosols in the electrostatic precipitator.

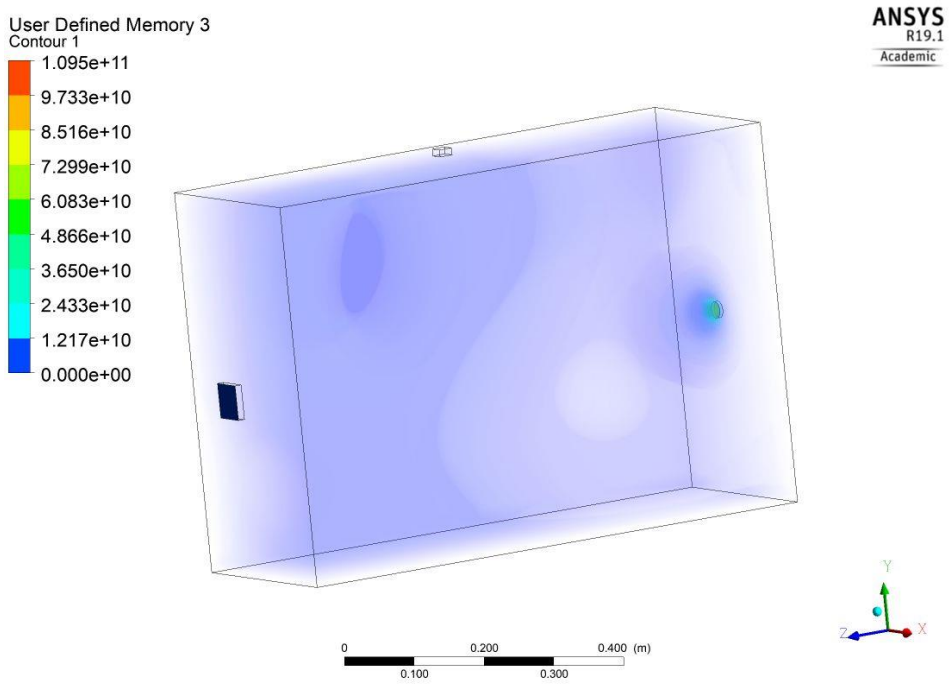

Fig. 4.12 Simulated electric field intensity (V/m) in the chamber.

The predicted electrostatic forces acting on a bioaerosol at a location in the chamber ranged from 3.6×10^{-7} to 6.6×10^{-7} N, with the maximum near the ionizer at 180 s of ionization. As indicated by equation (3.18), the magnitude of the electrostatic force is proportional to the product of the amount of charges acquired by a bioaerosol and the electric field intensity, while the amount of charge on a bioaerosol is the product of the number of ions attached to the bioaerosol and the charge of an ion (1.6×10^{-19} C). To determine if the electrostatic force was the primary underlying mechanism for bioaerosol removal from the chamber, simulation results for bioaerosol removal during ionization was compared to simulation results for bioaerosol removal under natural decay (Fig. 4.13). There was a rapid removal of bioaerosols under ionization than the natural decay. Within the first 5 s of ionization, the electrostatic forces generated drove the bioaerosols which

were located 1 cm away from the chamber walls to become attached to the chamber walls (grounded surface). This initial attachment resulted in 10% removal of bioaerosols from the chamber. During the same period, less than 1% of bioaerosols were removed under natural decay. By 30 s of ionization, about 50% of the bioaerosols had been removed from the chamber resulting in a concentration of 455#/cm^3. Comparatively, less than one percent had been removed under natural decay. At 195 s of ionization, about 90% of bioaerosols had been removed under ionization with a concentration of 10#/cm^3 remaining in the chamber. In comparison, under natural decay less than 3% of the bioaerosols had been removed from the chamber. 100% of bioaerosols were removed from the chamber at 175 s of ionization, whereas, less than 10% of bioaerosols were removed under natural decay. It could be concluded that the electrostatic forces were strong enough to drive the bioaerosols to the grounded surface.

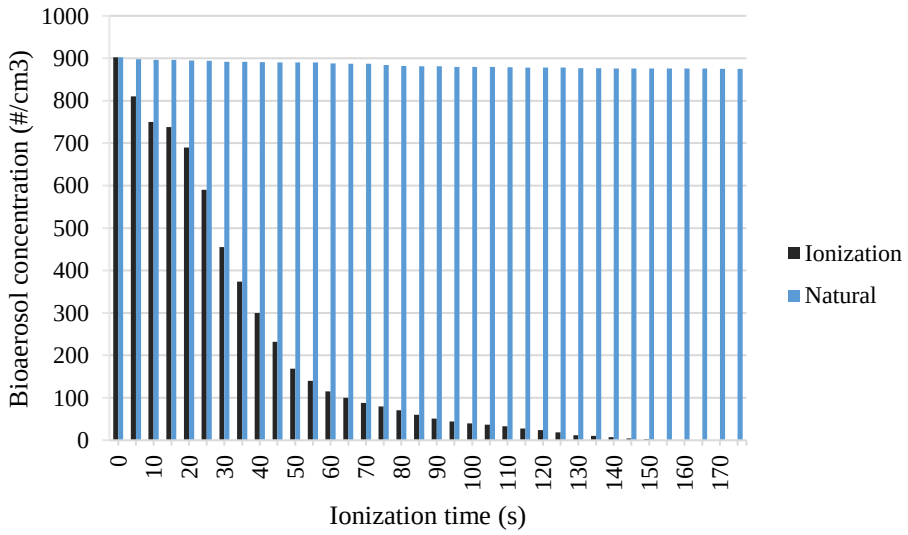

Fig. 4.13 Comparison of simulated bioaerosols concentrations in the chamber over time under natural decay and under ionization.

The number of ions which were predicted to have become attached to a bioaerosol ranged from 39 ions/aerosol at 5 s of ionization to 70 ions/aerosol at 175 s of ionization based on measured ion concentration of 2.4×10^{13} ions/m^3 (Fig. 4.14). Using the ion concentration of 2.9×10^{13} ions/m^3 from the simulations, the number of ions which were predicted to have become attached to a bioaerosol ranged from 39 ions/aerosol at 5 s of ionization to 71 ions/aerosol at 175 s of ionizations. The difference between using the simulated ion concentrations and measured data was negligible (just a single ion) during ionization (Fig. 4.14). This confirmed that even though the predicted ion concentration of 2.9×10^{13} ions/m^3 was 20% higher than the measured value, the difference did not significantly affect the number of ions attached to a bioaerosol. In other words, the steady state ion concentration predicted by the ion transport model was adequate for determining the ion attachment to bioaerosols.

It was observed that the number ions attached to a bioaerosol increased with time in a nonlinear fashion (Fig. 4.14). Ions became quickly attached to a bioaerosol during the first five seconds of ionizations, and then slowed. For the calculation based on the measured ion concentration, the fastest attachment (aerosol charging) rate of 7.8 ions/s occurred during the first five seconds of ionization. Between 5 and 10 s of ionization, the charging rate significantly decreased to 0.6 ions/s. The reduction continued until 45 s of ionization and thereafter where a charging rate of 0.2 s and lesser occurred. Similarly, the fastest charging rate predicted from the simulated ion concentrations occurred during the first five seconds of ionization, at 7.8 ions/s. The dropped to 0.8 ions/s between 5 and 10 s of ionization. At 45 s of ionization, the charging rate decreased to less than 0.2 ion/s. Attenuation of the charging rate was because when the ions

initially become attached to a bioaerosol, they set up an electric field around the bioaerosols which repel ions of the same polarity (negative ions) from becoming attached to the bioaerosol.

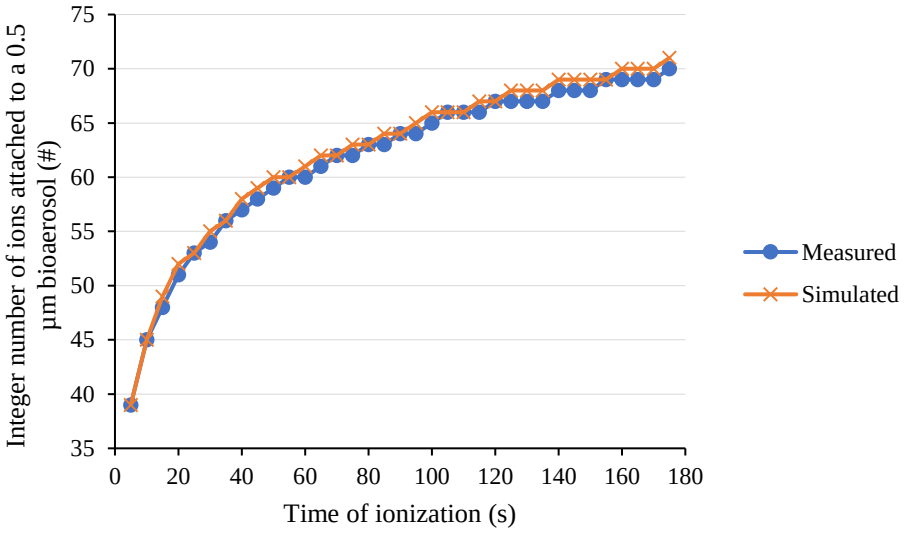

Fig. 4.14 Number of ions attracted to a bioaerosol of 0.5 µm (Note: the simulated ion concentration was 2.9×10^{13} and measured of 2.4×10^{13} ions/m^3) during diffusion charging.

The bioaerosol size was found to affect diffusion charging of bioaerosols (Fig. 4.15). Specifically, with increasing bioaerosol size, the number of ions which became attached to a bioaerosol increased. When the bioaerosol size doubled, the number of ions attached to the bioaerosols also doubled. An increase in bioaerosol size means an increase in the bioaerosol surface area A larger surface area increases the probability of an ion collision with a bioaerosol.For an example, a total of 40 ions became attached to a 0.4 µm bioaerosol at 20 s of ionization, while a total of 84 ions became attached to a 0.8 µm bioaerosol.

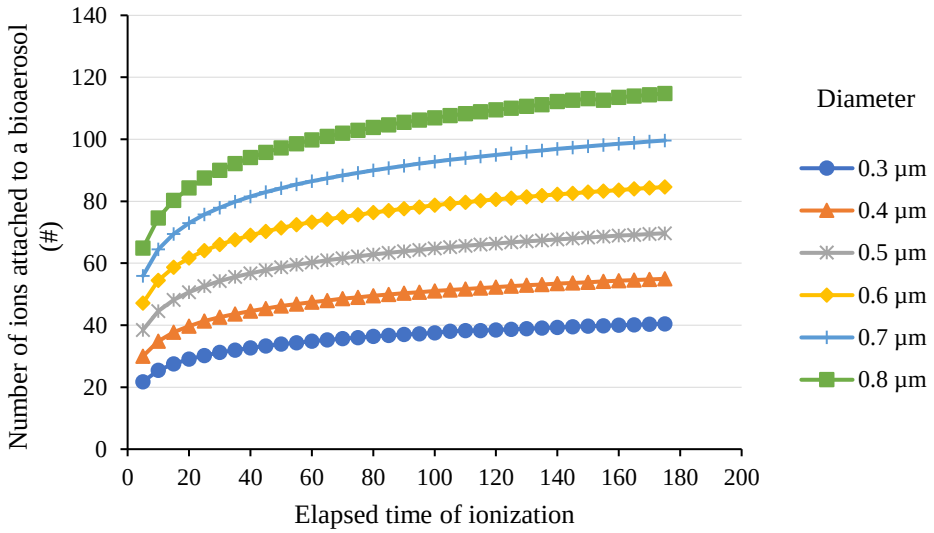

Fig. 4.15 The number of ions predicted to be attached to bioaerosols of different sizes at an ion concentration of 2.4×10^{13} ions/m^3.

4.4 Bioaerosol removal for model validation

The simulation model consisted of several key components, including airflow, aerosol transport, and electrical field, to simulate the various processes in ionization, and ultimately to predict the removal of bioaerosols from air. Validating the individual model components would be challenging, and therefore the most important overall outcome from the model simulations – the aerosol concentration in the chamber, was used to validate this integrated model. Specifically, the simulated bioaerosol concentrations were compared to the results obtained from the chamber tests for scenario B in which circulation fans were used to promote mixing in the chamber to achieve uniform bioaerosol distributions. Bioaerosol concentrations were measured at the five locations as shown in Table 3.4. ANOVA was first carried out to determine if the location had any effect on bioaerosol concentration. The concentrations at the five locations were compared to each

other for each sampling time interval (every 10 s during ionization). The details of ANOVA results are shown in Appendix B. It was found that the location had significant ($P < 0.05$) effect on the bioaerosol concentrations during the first 20 s of ionization, and no significant effect after 20 s (the differences in ion concentration among the five locations were not significantly different from each other after 20 s of ionization). Based on this result, one of the five locations was selected to take detailed bioaerosol measurements to represent the average concentration within the chamber for subsequent tests. Single location tests avoided the switch of sampling ports during test (because only one particle analyzer was available), allowing more frequent bioaerosol sampling. In each test, the bioaerosol concentration was monitored continuously until a stable level was established (902 #/cm^3), and then the ionizer was turned on. After ionization started, the concentration of bioaerosol began to reduce (Fig. 4.16), while an ion concentration of 2.4×10^{13} ions/m^3 was maintained in the chamber.

The effectiveness of ionization for removing bioaerosols from the chamber was determined by calculating the removal rate (Equation 4.2), determined as the number of bioaerosols removed per given time period of five seconds. The highest removal rate over a five second period was measured to be 25 bioaerosols $cm^{-3}s^{-1}$, which occurred between the 20 and 25 s. The lowest rate was 0 between 135 and 140 s. The effectiveness was also determined over a longer period of 30 s by averaging the bioaerosol removal data over a 30 s period of ionization. It was observed that the removal rate decreased with time. Over the first 30 s, a removal rate of 16 bioaerosols/cm^3 was obtained, it then decreased to 7 bioaerosols $cm^{-3}s^{-1}$ between 30 and 60 s, or a 50% reduction. The removal rate continued to decrease until 160 s to less than 0.5 $cm^{-3}s^{-1}$.

$$R_b = \frac{C_{tp} - C_{tc}}{\Delta t} \qquad 4.2$$

where:

R_b = bioaerosol removal rate (#cm^{-3}s^{-1})

C_{tp} = bioaerosol concentration at previous time (#/cm^3)

C_{tc} = bioaerosol concentration at current time (#/cm^3)

Δt = change in time (s)

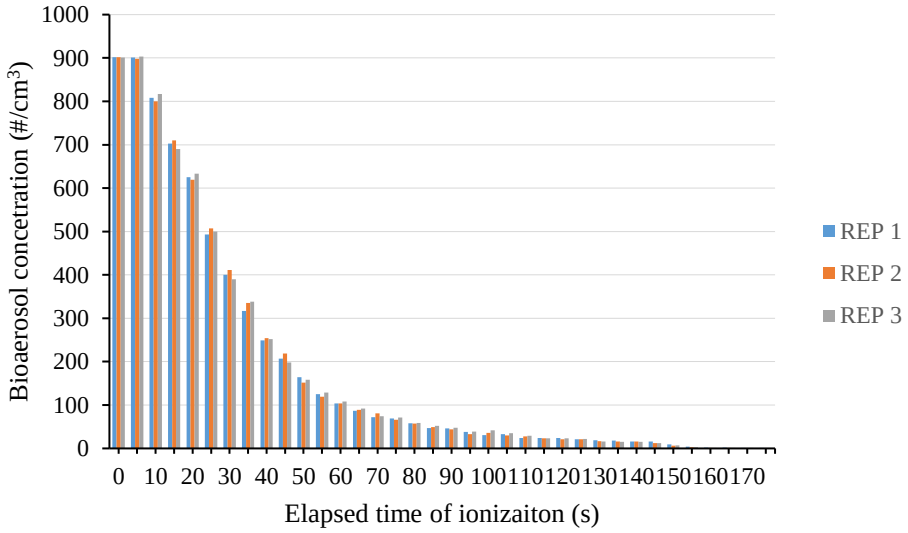

Fig. 4.16 Measured bioaerosol concentrations during ionization (three replications).

The model prediction of the bioaerosol concentration at each and every sampling time was compared to the measured data to determine if the predicted concentration fell within the 95% confidence interval (CI) of the corresponding measured value (Fig. 4.17). It was observed that only 22% of the predicted values fell within the 95% CI of the measured bioaerosol concentrations. The model predictions in the first 40 s of ionization agreed closely with the measured bioaerosol

concentration. However, after 40 s of ionization, the model predictions were higher than the measured values. At 175 s, all bioaerosols had been removed from the chamber in the experiment, whereas, the simulation predicted a concentration of 30 bioaerosols/cm^3. It should be noted that the bioaerosol concentrations obtained for the measured replicates at each time point were very close to each other (Fig. 4.16), and hence, a very narrow CI band was obtained. Consequently, although some predicted values were not within the 95% CI band, the trend of bioaerosol removal predicted by the model closely followed the measured data. Further statistical analyses were then performed to the model adequacy and performance.

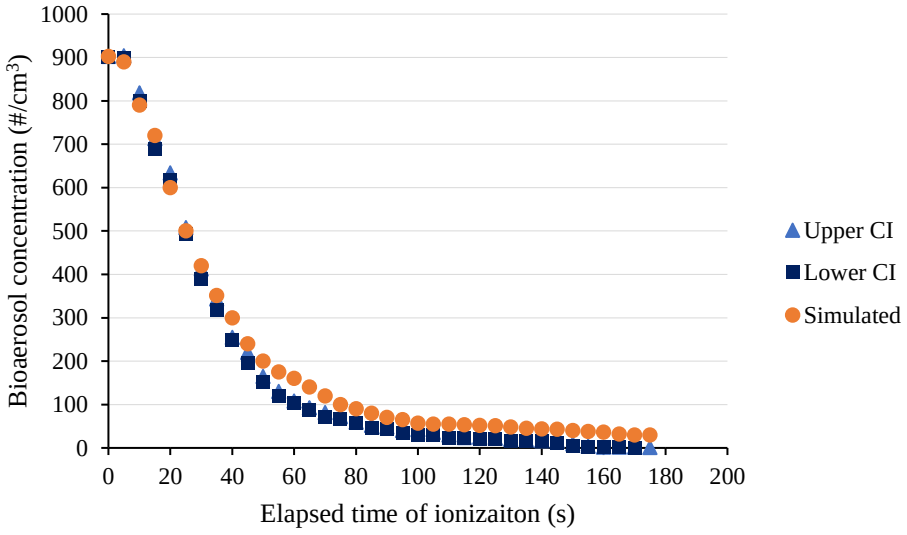

Fig. 4.17 Comparison of predicted bioaerosol concentration with the measured data during 180 s of ionization (with only the floor grounded in simulation).

Fractional bias (FB) was used to determine the bias in model prediction. The obtained FB value increased gradually with time but stayed within 2 (Fig. 4.18). This indicated that that the bias was acceptable. The slightly negative FB values obtained from start until about 20 s of ionization show that the model predicted lesser bioaerosol concentrations than the measured tests.

This means the model removed bioaerosols at a faster rate than the measured tests within the first 20 s. However, after 20 s of ionization, the model began to remove bioaerosols at a lesser rate than the measured tests and hence produced higher concentrations in the chamber after 20 s until ionization ended. This faster rate removal produced positive FB values after 20 s of ionization. The bias in the model increased with time however this was mainly due to the relative differences obtained between the measured and predicted. For instance, at 40 s of ionization, a bioaerosol concentration of 252 #/cm^3 was measured in the chamber. However, a concentration of 300 #/cm^3 was predicted by the model yielding a numerical difference of 48 #/cm^3 and a relative difference of 16%. An FB value of 0.18 was obtained. At 160 s of ionization, a chamber concentration of 2 #/cm^3 was measured while the model predicted a concentration of 36 #/cm^3. This produced a numerical concentration difference of 34 #/cm^3 (which was less than obtained at 40 s) and a relative difference of 94%. However, the FB value of 1.89 obtained at that point was bigger than the 0.18 obtained at 40 s. Overall, an average FB of 0.6 was obtained over the ionization period which makes the bias in the model prediction acceptable.

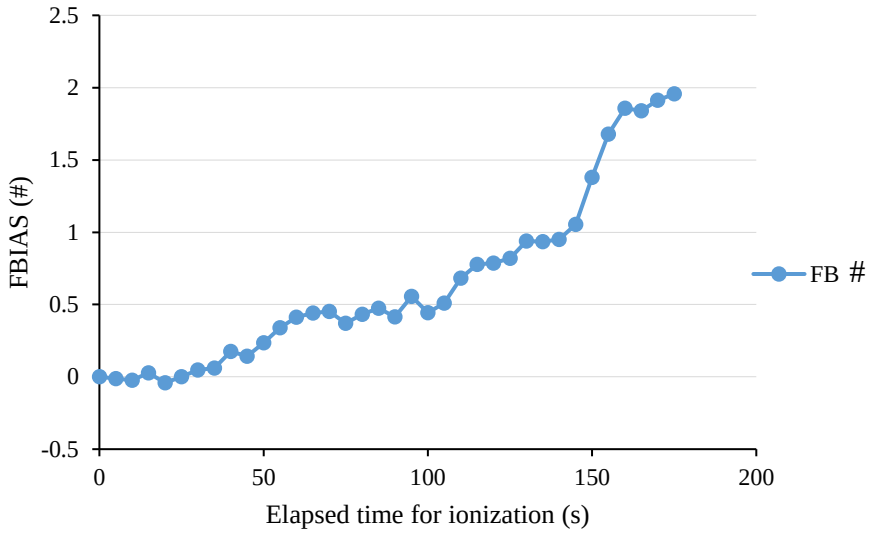

Fig. 4.18 Fractional Bias values for evaluating the bias of model predictions (with only the floor grounded in simulation).

A regression of the measured concentration against the predicted concentration was performed to further evaluate the overall agreement between the model prediction and the measurement (Fig. 4.19). An R^2 value of 0.985 was obtained for the regression, indicating the overall prediction by the model for removing bioaerosols strongly followed the experimental data. A slope of 1 was obtained for the regression, indicating the model predictions agree closely to the measured data.

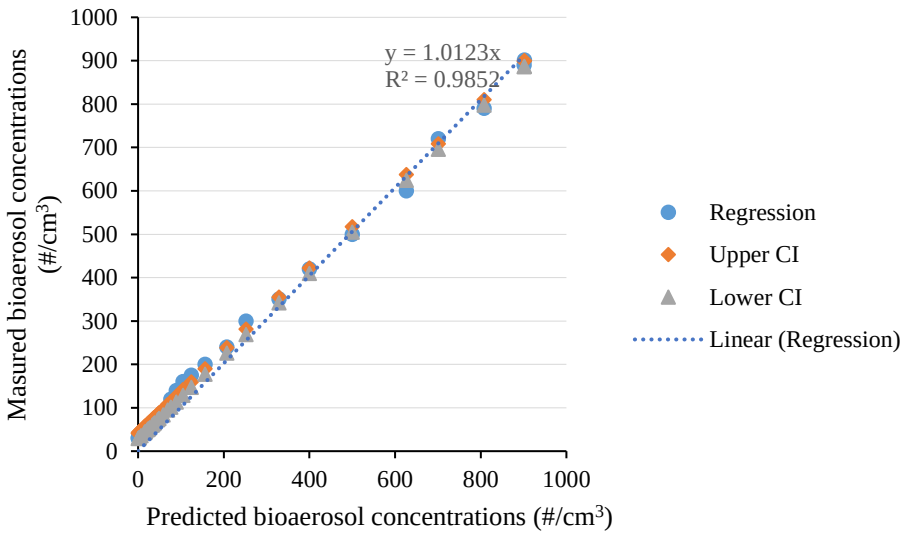

Fig. 4.19 A regression of the measured bioaerosol concentrations versus the predicted bioaerosol concentration (with only floor grounded in simulation).

As discussed earlier, the discrepancies between the model predictions and the measured data occurred after 40 s of ionization, with the model predictions higher than the measured values. In particular, the bioaerosol concentration reached zero at 175 s in the experiment but predicted to be 30 #/cm^3 by the model. This might be due to the exclusion of chamber walls in adsorbing bioaerosols in the model simulation. Specifically, the simulation assumed that the bioaerosols were only to be attracted to the grounded surface (a metal strip placed on the floor of the chamber). Although the plexiglas walls were not grounded, they might still attract /collect bioaerosols. Wu et al. (2006) conducted a chamber study to investigate the effect of the nature of wall surface materials (stainless steel, wood, PVC, wallpaper and cement paint) on the removal of airborne particles in the presence of negative ions. They showed that all the surfaces tested were effective in removing particles with the efficiency in a descending order as follow: wood > PVC> cement paint > wallpaper > stainless steel. Other investigators reported similar observations (McMurry

and Rader 1985; Nomura et al. 2007). A smoke test conducted in this study also showed that smoke particles were deposited on the chamber walls during ionization (Fig. 4.11). Based on the above discussion, it seemed reasonable to consider the attraction of bioaerosols by the chamber walls. Therefore, a set of simulations were carried out with all the chamber walls considered to be grounded so that the bioaerosols could be attracted to and collected by them. The simulations with grounded walls resulted in bioaerosol concentrations in good agreement with the measured values (Fig. 4.20). It should be pointed out that the bioaerosol concentration remained at 30 bioaerosols/cm^3 in the simulation without considering the wall attraction, whereas the new simulation considering the wall effect predicted that all the bioaerosols were removed from the chamber at 155 s of ionization (Fig. 4.20), which was in better agreement with the experimental observation in comparison with the simulations without considering the wall effect. However, the complete removal of bioaerosols from the chamber occurred 20 s earlier in the model simulation than in the experiment (155 s vs. 170 s). This meant that the plexiglas walls in the test chamber were probably as efficient as a grounded wall in attracting charged aerosols. In other words, treating the plexiglas walls as grounded walls in simulations might lead to over prediction of the bioaerosol removal efficiency. Improvement of model performance by considering the wall attraction (grounding the walls) was reflected after 40 s of ionization, with 78 % of the predicted values within the 95% CI band of the measured data (Fig. 4.20). However, the improvement was not apparent before 40 s mainly due to the longer time for the simulation to reach the steady state than the experiment.

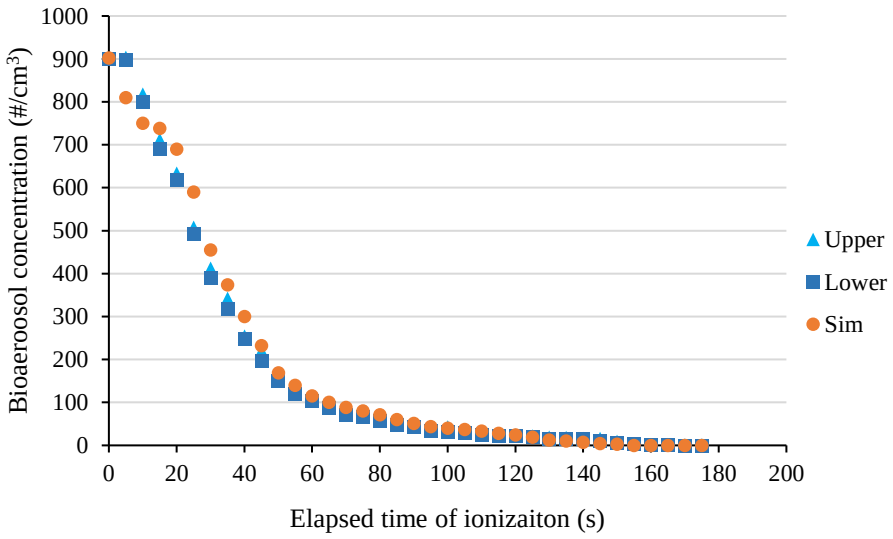

Fig. 4.20 Comparison of predicted bioaerosol concentration with the measured data during a 180 s ionization (with all walls grounded in simulation).

The bias in model predictions with the wall effect was evaluated using the FB. Negative FB values were obtained from start of ionization until 10 s of ionization and between 125 s of ionization until 175 of ionization. At these times, the model predicted lesser concentrations than the measured. This means the model removed more bioaerosols at these time points than measured. From 15 s to 120 s however, positive FB values were obtained with an average of 0.13. Between these time points, the model predicted higher concentrations than the measured, which also means that the model removed bioaerosols slowly than measured. FB values between -1 and -2 were obtained for time points between 145 and 175 s of ionization. These values obtained are mainly due to the relative differences between the predictions and the measurements. For example, at 170 s of ionization, a bioaerosol concentration of 1 #/cm^3 was measured, while the model had predicted 100% removal of bioaerosols at that point, hence yielding a concentration difference of 1 #/cm^3 and a relative difference of 100%. A relative difference of 100% would suggest a large bias (FB

value of -2). However, from a practical viewpoint, a numerical difference of 1 #/cm^3 means the model prediction agrees closely with measured and should not be considered biased. Overall, an FB value of -0.3 was obtained for simulations with all walls grounded, compared with an FB value of 0.6 for simulations without the walls grounded. Hence model predictions for simulations with all walls grounded is less biased that without walls grounded.

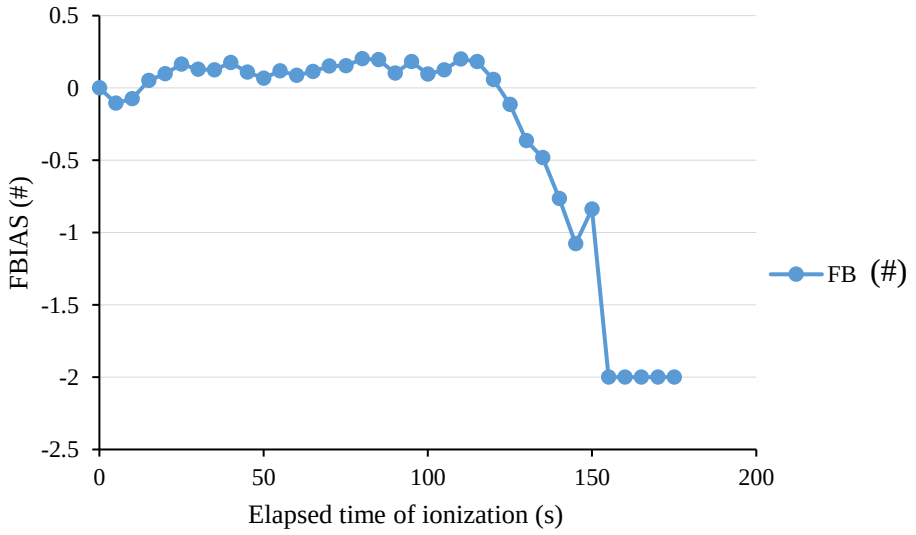

Fig. 4.21 Fractional Bias values for evaluating the bias of model predictions (with walls and floor grounded in simulation).

The adequacy of model performance with the wall effect was further confirmed by the regression analysis (Fig. 4.22). An R^2 value of 0.987 was obtained for the regression, indicating the overall prediction by the model for removing bioaerosols strongly followed the experimental data. A slope of 1 was obtained for the regression line, indicating the model predictions agreed closely with the measured data.

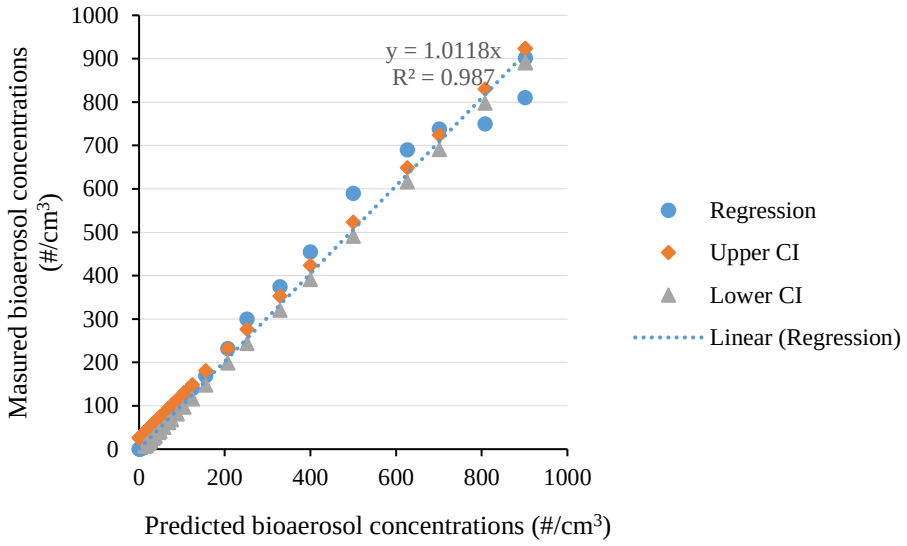

Fig. 4.22 A regression of the measured bioaerosol concentrations versus the predicted bioaerosol concentration (with all walls grounded in simulation).

Predicted bioaerosol concentrations were compared between simulations with and without considering the wall attraction (Fig. 4.23). The simulation without the wall attraction predicted higher concentration of bioaerosols in general except at time points between 15 s and 35 s. Taking 20 s as an example, a concentration of 600 bioaerosols/cm^3 was predicted in simulation with only a metal strip grounded at the chamber bottom, while a concentration of 690 bioaerosols/cm^3 was predicted by the model with all the walls grounded. This was probably because the simulation with grounded walls did not reach the steady state until 20 s. Overall, an average difference of 33 bioaerosols/cm^3 was found between the two simulation conditions (the simulation with grounded walls had a higher removal rate, as expected).

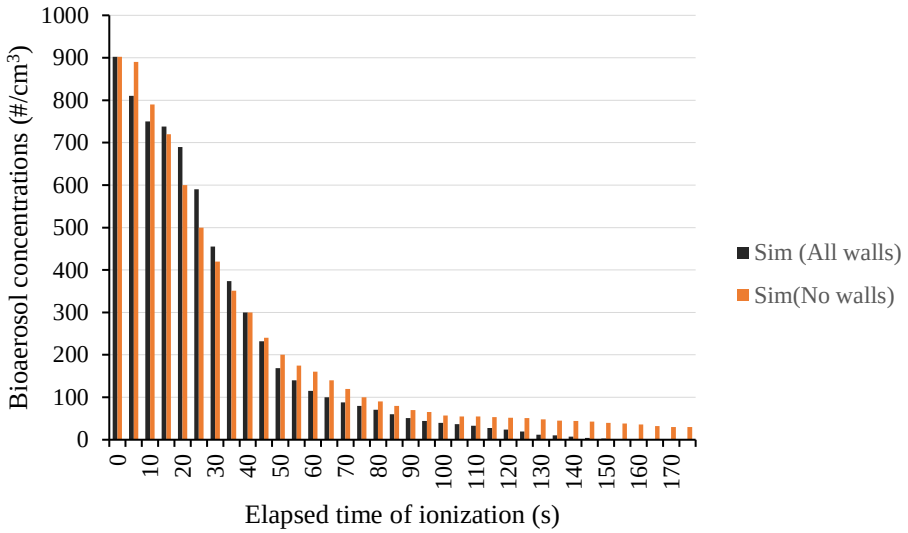

Fig. 4.23 Comparison of bioaerosol concentrations between simulations with and without wall attractions. All walls: all chamber walls were grounded in simulation; No walls: only the floor was grounded in simulation.

In summary, the results from the simulation with all walls grounded were in closer agreement with the measurements than the simulation with only a metal strip grounded at the bottom of chamber. In particular, all bioaerosols in the chamber were removed in the simulation with grounded walls, while an average concentration of 30 bioaerosols /cm^3 remained in the chamber at 175 s of ionization in the simulation without grounded walls. Even when simulation was extended to 250 s of ionization, a concentration 14 bioaerosols/cm^3 still remained. Therefore, it was concluded that the wall attraction should be considered in simulating bioaerosol removal by air ionization even if the walls are made of non-conductive materials. However, it should also be noted that treating the non-conductive walls (such as plexiglass in this study) as grounded surface in simulations might lead to over prediction of the bioaerosol removal.

4.5 Biological effects of air ionization

4.5.1 Adequacy of sampling bioaerosols for infectivity measurement

A t-test pairwise comparison between the calculated and measured viral titers were conducted to determine if the titers of sampled bioaerosols were the same as that theoretically calculated from the amount of stock solutions introduced into the chamber. It was observed that the measured titers were numerically lower than the calculated titers at all measurement time points (decay stages)(Fig. 4.24 a, b, c). The maximum relative difference was 20% near the end of decay test at a bioaerosol concentration of $9/cm^3$ for stock solution A, 18% for B at a bioaerosol concentration of $631/cm^3$ and 20% at a bioaerosol concentration of $90/cm^3$ for C. However, paired t-tests showed that the difference between the calculated and the measured titers was not statistically significant ($p>0.05$).

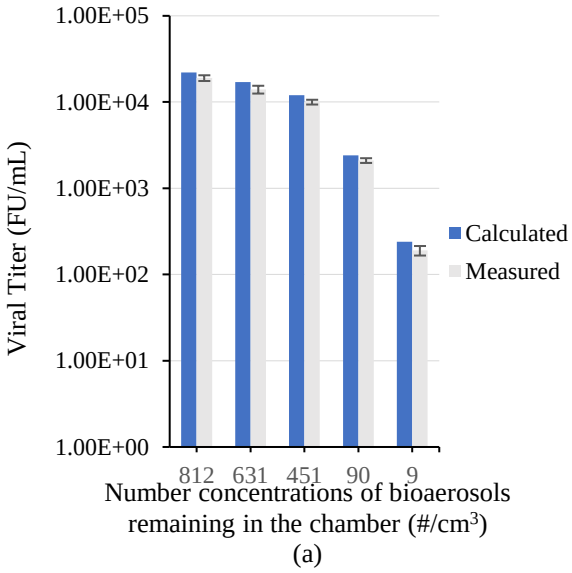

(a)

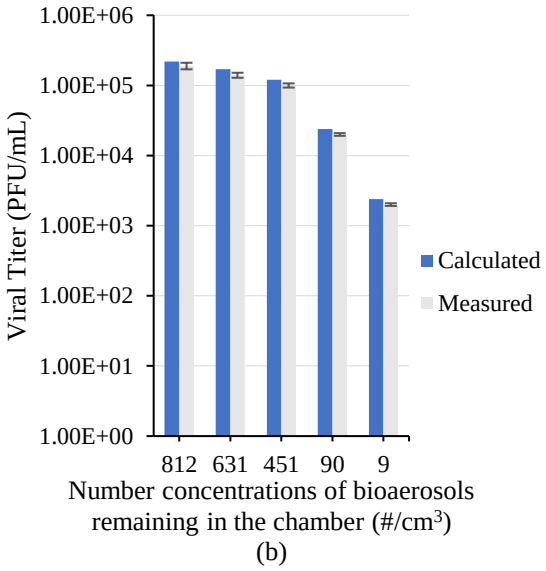

(b)

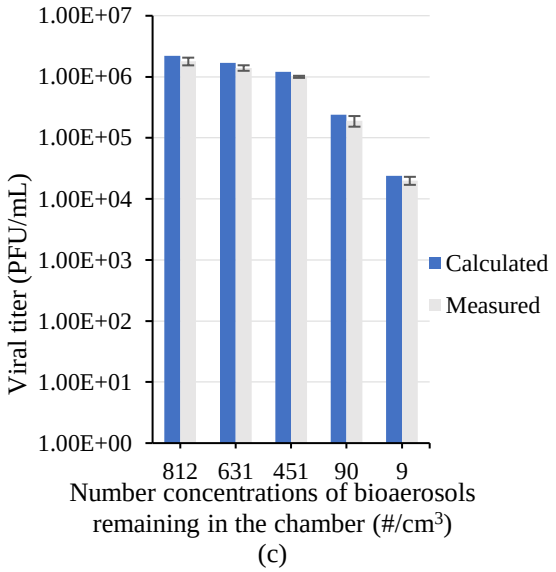

(c)

Fig. 4.24 Comparison of the measured titers in the chamber to theoretically calculated titers for stock solution a, b and c. *Error bars show the SEM obtained from three replicates of each stock solution*

The lower measured titer values in comparison with the calculated values could be attributed to losses of viral solution in the bioaerosol generation process. Specifically, it was observed that aliquots of the stock solution accumulated at the aerosol inlet tubing after the aerosolization process. To estimate the lost amount, the tubing was carefully pulled out after each experiment

and the liquid accumulated in the tubing was carefully poured into a 2 mL Eppendorf tube. Due to low volumes of liquid accumulated in the tubing for each test, the six replicates were pooled together, and the average was taken as the volume lost for each test. The results showed that stock virus losses due to accumulation in the inlet tubing accounted for less than 5% of the reduction in the measured titers (Table 4.1).

Table 4.1 Estimated viral titer losses due to liquid accumulation in the aerosol inlet tubing.

Stock titer	Volume accumulated (µL)	Estimated final titer without losses (PFU)	Estimated final titer with losses (PFU)	Titer reduction (%)
2.8×10^9	250	2.4×10^6	2.3×10^6	4.2
2.8×10^8	250	2.4×10^5	2.3×10^5	4.2
2.8×10^7	250	2.4×10^4	2.3×10^4	4.2

Another possible reason for the lower measured titer values was the losses of bioaerosols to the walls of the chamber. The trajectory of the bioaerosols into the chamber was perpendicular to one of the chamber walls and therefore some bioaerosols might have hit the walls and settled there. To account for this loss, wall swabs were taken immediately after aerosolization and used to conduct plaque assays. A piece of Whatman paper measuring 2 cm x 2 cm was used to swab the six surfaces within the chamber. Each piece of paper was subsequently diluted in 20 mL of PBS and vortexed. Afterwards, the six solutions were pooled together and a volume of 100 µL was used to conduct plaque assays (Table 4.2)

Table 4.2 Table showing titer losses due to bioaerosols settling on chamber surfaces.

Stock titer (PFU/mL)	Titer from swabbed area (PFU/mL) ± SEM	Total titer loss to chamber walls (PFU/mL)	Relative to calculated titer (%)
2.8×10^9	$2 \times 10^1 \pm 3$	9.8×10^4	4
2.8×10^8	8 ± 1	3.9×10^4	1.6

The total titer loss to the chamber walls was obtained by first dividing the total surface area of the chamber (19600 cm^2) by the swabbed area. The value obtained was then multiplied by the titer obtained from the swabbed surface area to obtain the total titer loss to the chamber. A loss of 4 and 1.6% was obtained for stock C and B respectively.

Another reason for the differences between the calculated and the measured titers could be the sampling efficiency of the SKC Biosampler used in this study. The manufacturer specifications states that, the biosampler has a physical sampling efficiency as 90% for aerosols which have aerodynamic diameters of 0.5 µm and below (SKC 2019). However, several investigators evaluated the SKC biosampler's ability to capture bioaerosols and reported various efficiencies for the biosampler. Hogan et al. (2005) aerosolized IBDV virus and used the SKC sampler for bioaerosol collection. They showed that the sampling efficiency of the SKC biosampler was below 10% for viral particles in the size range of 30 – 100 nm. Lia et al. (2018) aerosolized H1N1 influenza A and evaluated the viral sampling efficiency of the SKC biosampler. They reported that the SKC biosampler had a 5% viral collection efficiency for viral particles in the size range between 10 nm and 300 nm. Kesavan et al. (2010) conducted a study to investigate the sampling efficiency of the SKC sampler for both biological active and inactive particles. They reported a

sampling efficiency of 96 and 98% for particle sizes of 1 and 3 µm respectively. They further reported that the SKC sampler had a sampling retention efficiency of 79% for culturable *Bacillus atrophaeus.* La (2014) aerosolized Porcine Reproductive and Respiratory Syndrome Virus (PRRSV) and captured the bioaerosols using SKC biosampler. The PCR analysis of her results showed that the virus concentration she measured with SKC sampler was only about 21% of the theoretically calculated concentrations of aerosolized virus concentration . It's possible that the biosampler's capturing capacity was a causal effect to the low concentrations she measured. Zhao et. al (2014) showed that the AGI- 30 (All glass impinger) had a physical sampling efficiency of 96% for airborne viral sampling. However, in an earlier study, Herman and Zimmerman (2008) compared the efficiency of the SKC biosampler to the AGI-30 and reported that there was no statistically significant difference between the analytical sensitivity for the collection of artificially generated bioaerosols containing cell-cultured PRRSV. It appears that the sampling efficiency of the SKC biosampler is dependent on the type of microbe being sampled and the unique idiosyncrasies of the biosampler.

The average relative difference in titers obtained for the natural decay tests showed the actual titers obtained from plaque assay was about 20% lower than the calculated titers (Fig. 4.24), of which about 10 % was due to losses to the inlet and the walls (Table 4.1 and Table 4.2) and the remaining possibly due to the biosampler efficiency. This percentage loss was factored into actual titers obtained from plaque assays.

4.5.2 Ionization effect on virus titers

The effect of ionization on virus infectivity was determined by a t-test comparison between viral titers obtained for the natural decay (no ionization) and ionization tests at the same time points for the three stock solutions A, B and C (Fig. 4.25a, b, c). For the natural decay, the viral titers did not significantly change over the determined time of 90 s for each stock solution. In comparison, viral titers during ionization decreased with time. During the first 10 seconds, the viral titers were reduced by 25% to 33% for each test, further reduced by 94% and 96% in 20 s, and by more than 99% (more than two $\log_{10}$ reduction) in 90 s. Paired t-tests revealed the viral titers obtained for ionization tests were significantly lower than those in natural decay at 30 s and 90 s. In other words, ionization significantly reduced the viral titer and the longer the ionization continued, the greater the reduction in viral titers.

The effectiveness of ionization for viral inactivation was also described by the virus survival percentage (SP). The SP describes the percentage of viruses remaining in the chamber which are still infectious and was calculated as shown below;

$$SP = \frac{V_{ins}}{V_{nds}} \times 100 \tag{4.3}$$

where:

SP = survival percentage

V_{ins}= viral titer obtained for ionization at sampling point (PFU/mL)

V_{nds} = viral titer obtained for natural decay at a sampling point(PFU/mL)

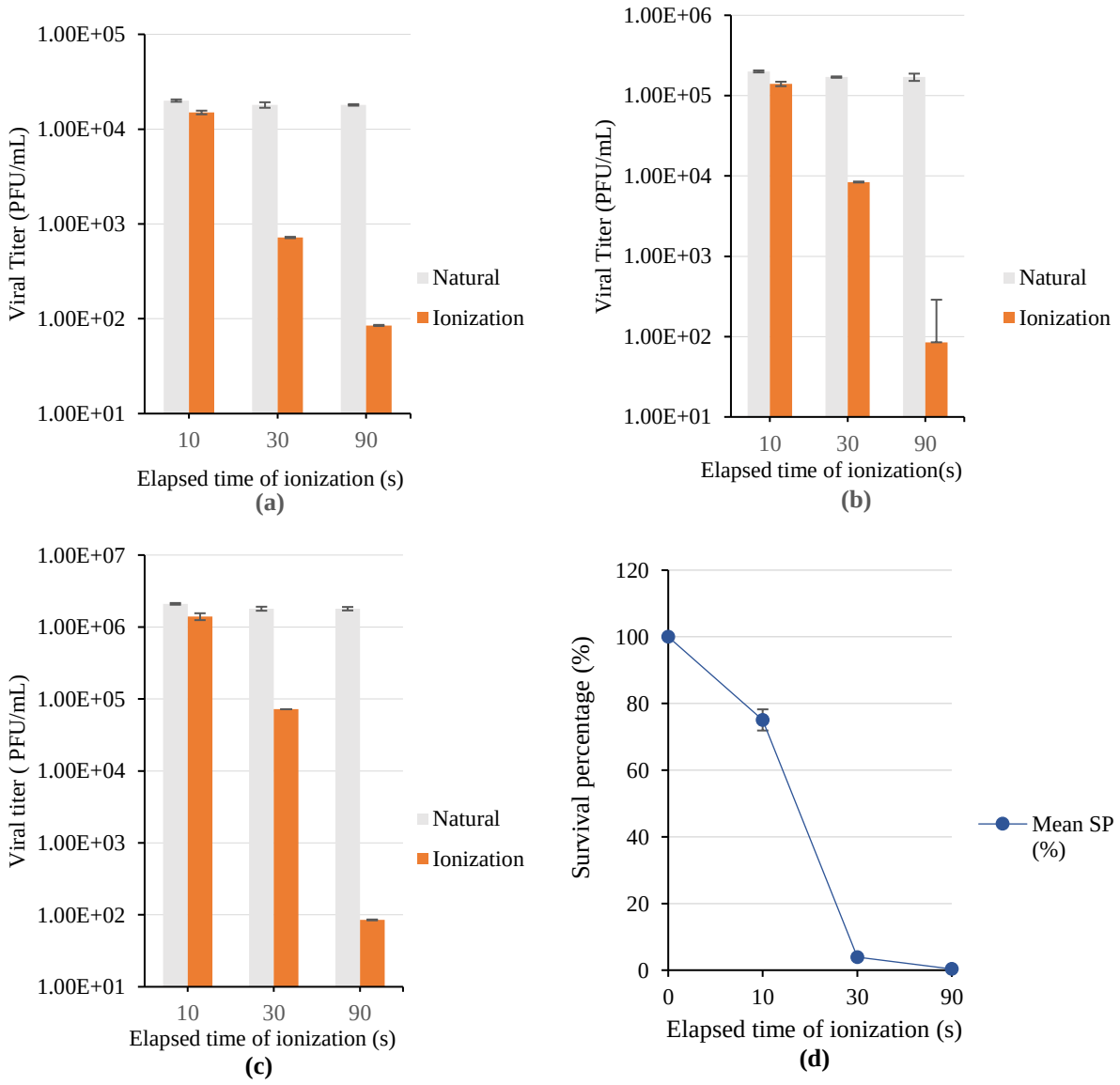

Fig. 4.25 Comparison of virus titers between ionization and natural decay for stock solutions A (a), B (b) and C (c) at ion concentration of 2.4×10^{13} ions/cm^3 and the mean survival percentage (d). *Error bars indicate SEM obtained from three replicates of each stock solution.*

The SP values were determined for nine biological replicates (three replicates for each of the three stock solutions: 3 x 3 = 9) and the general trends for reduction of viral titers were similar for all replicates. Therefore, the SP values for all the biological replicates at each time point were averaged to obtain a representative SP at each sampling point (Fig. 4.25d).

For all the three stock solutions, the SP decreased with the elapsed time of ionization, from 100% at the start to almost 0% at 90 s. The obtained SP values ranged from 75% at 10 s; 4% at 30 s; and 0.4% at 90 s (Fig. 4.25). At 10 s, ionization produced a 25% reduction in the starting stock titer and the remaining virus load in the chamber had a titer equivalent to 75% of the initial stock. At 30 s, ionization caused a 96% reduction in the virus titer which meant only 4% of the surviving virus load was infectious. At 90 s, only 0.4 % of the airborne virus load was infectious. As explained earlier in section 4.5.2, time is critical to the number of ions which became attached to a bioaerosol. The longer the residence time of a bioaerosol in the chamber, the more ions it acquired, and consequently the greater the viricidal effects.

4.5.3 Biological effect of ionization on virus titers

The reduction of bioaerosol infectivity in air samples by ionization may be attributed to two mechanisms: physical removal of bioaerosols from the air and inactivation of virus by ions. Paired t-tests were performed to compare the viral titers between ionization and natural decay when the same number of bioaerosols remained in the chamber to determine the effect of ionization on viral titers (Fig. 4.26).

Results in Fig. 4.26 show that ionization reduced the viral titers when compared to the natural decay at the same bioaerosol concentrations except at sampling point of 812 #/cm^3 for all

three stock solutions. This means that ionization either biologically inactivated the virus or physically removed the virus from air. At a bioaerosol concentration of 812 #/cm^3 remaining in the chamber, the viral titers were reduced by 22% to 24%, by 60% and 65% at 631 #/cm^3, and greater than 95% at 451 #/cm^3 or less.

It must be emphasized that most of the virus generated into the chamber were below the detection threshold of the particle counter and therefore bioaerosol concentrations were only used as sampling points to get an understanding of the rate of reduction of total virus load in the chamber. Therefore, the virus titers obtained at the sampling points reflect both the titers of the detectable bioaerosols and the undetectable virus load in air. The continuous reduction in viral titers as bioaerosol concentrations became lesser was due to the reason that, at lower bioaerosol concentrations, the airborne viral load had been exposed to a longer time of ionization (it took a longer time to reach the lower concentrations in this experiment). It was therefore expected that the longer the virus spent in the chamber during ionization, the more ions they acquired. As they acquired more ions, the viricidal and removal effects of the ions increased and hence contributed to a continuous reduction in viral titers over time.

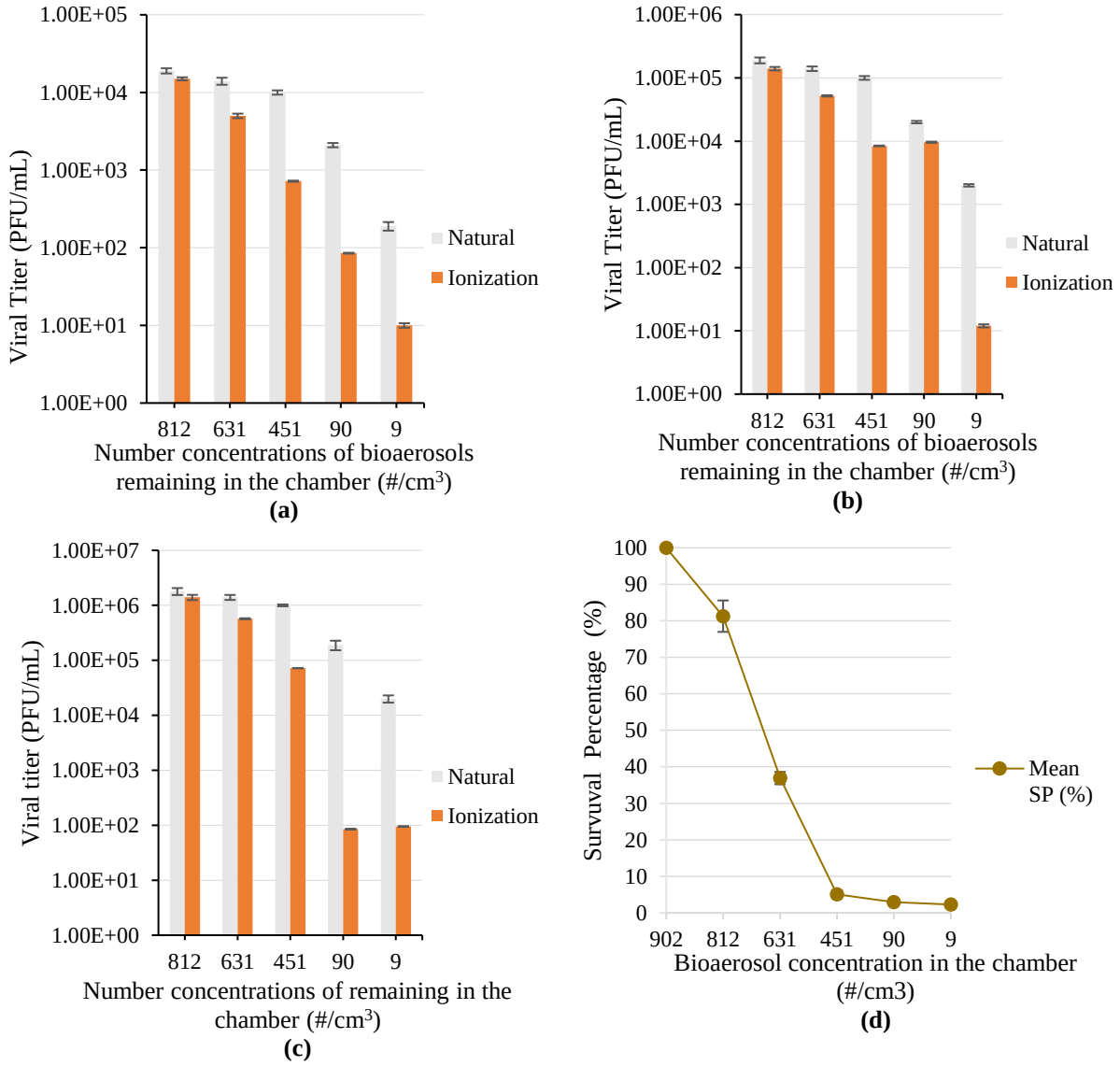

Fig. 4.26 Comparison of virus titers between ionization and natural decay for stock solutions A (a), B (b) and C (c) at the same level of bioaerosol concentration for ion concentration of 2.4×10^{13} ions/cm^3 and the mean survival percentage (d). *Error bars show SEM obtained from three replicates of each stock solution.*

For all the three stock solutions, the SP decreased from 100% at bioaerosol concentration of 902 #/cm^3 to almost 0% at 9 #/cm^3. The general SP trends were similar for all 9 biological replicates and therefore, SP values for the replicates at same sampling points were averaged (Fig.

4.26d). The SP values obtained ranged from 81% at bioaerosol concentration of 812 #/cm^3; 37% at 631 #/cm^3; 5% at 451 #/cm^3, 3% at 90 #/cm^3 and 2% at 9 #/cm^3. The continuous reduction of SP values as the bioaerosol concentration decreased was mainly due to the effects of the negative ions generated. Ionization was used to quickly reduce the concentrations of bioaerosols in the chamber to the same concentrations as under natural decay. In the process of reducing the bioaerosol concentrations, the ions might have either caused the removal of virus from air or might have produced viricidal effects on the virus or both. The removal and viricidal effects of the ions on the virus are discussed in section 4.6.3.

It must be emphasized that reduction in infectivity was observed for a steady state ion concentration of 2.4×10^{13} ions/m^3 within the chamber during ionization. To test the effect of ion concentration, an experiment was conducted at a lower ion concentration. Specifically, a smooth corona electrode without pins (corona points) attached was used to generate less ions in the chamber. It was found that at a lower ion concentration of 3×10^{10} ions/m^3, the viral titers obtained were not statistically significantly ($p > 0.05$) different between ionization and natural decay (Fig. 4.27). In other words, an ion concentration of 3×10^{10} ions/m^3 did not produce viricidal effects on bioaerosols in the chamber. To further investigate the effect of ion concentration on the effectiveness of deactivation of viruses, a model is presented in section 4.5.5.

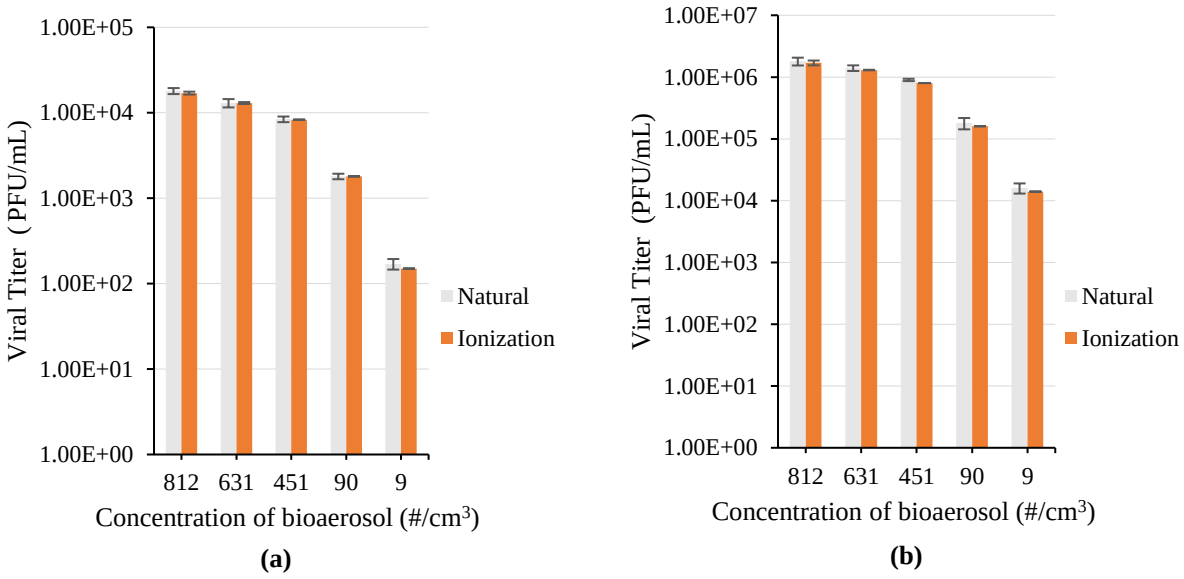

Fig. 4.27 Comparison of virus titers between ionization and natural decay for stock solutions A (a), and C (c) at the same level of bioaerosol concentration for ion concentration of 3.0×10^{10} ions/cm^3

4.5.4 The effect of initial stock concentration

During the ionization process, the number of ions that are attached to a bioaerosol is dependent on the ion concentration within the vicinity of the bioaerosol, the size of the bioaerosols and the exposure time of the bioaerosol to ions. At a given ion concentration in the number, the number of ions attracted to a bioaerosol with a certain aerodynamic diameter (e.g., 0.5 μm as in this study) could be predicted as a function of exposure time (Fig. 4.28). When the ion concentration in the chamber reached a steady state level 2.4×10^{13} ions/m^3, as measured in the test, a total of 45 ions had been attached to a 0.5 μm bioaerosol at 10 s of ionization. Plaque assay titers obtained at 10 s showed that this number of ions did not produce significant reduction in the infectivity of the bioaerosols for all the stock solutions (Fig. 4.25). At 30 s, approximately 54 ions became attached to the bioaerosol, and significant reduction (one $\log_{10}$) in the viral titer began to

occur in all the stock solutions (Fig. 4.25). In comparison, at an ion concentration of 3×10^{10} ions/m^3, a maximum of 40 ions were predicted by the model to have been attached to a 0.5 μm bioaerosol in 180 s. As discussed in earlier, 45 ions were not sufficient to produce any significant viricidal effect on the bioaerosol infectivity, hence the 40 ions which were predicted to have been attached to the bioaerosols was unlikely to cause a biocidal action. It is evident from this study that a threshold of ions must be attached to a bioaerosol for reduction in viral infectivity to occur, and this threshold was estimated be 54 ions for inactivating a 0.5 μm MRV bioaerosol.

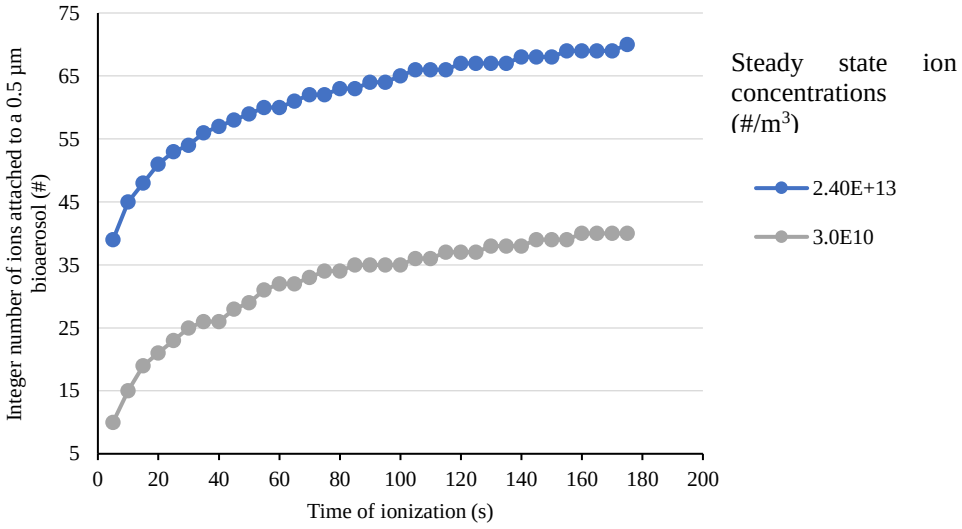

Fig. 4.28 Number of ions predicted by the model to be attached to a bioaerosol (0.5 μm) based on the concentration of ions measured at steady state under diffusion charging.

The results obtained also show that the viral titers for the stock solution (A, B, C) initially generated into the chamber were all reduced to similar percentages even though the stock solution differed in titers. Hence the effect of the initial stock titer on virus infectivity was the same. This can be explained by the reason that at steady state conditions, there was a high concentration of

ions (2.4×10^{13} ions/m^3) available in the chamber. As discussed earlier, only 54 ions were required to cause 90% (one $\log_{10}$) reduction in infectivity at 30 s of ionization and 64 ions required to cause a 99% (two $\log_{10}$) reduction in infectivity at 90 s of ionization. In this study, diffusion charging was determined to be the primary mechanism by which viruses acquired charges (ions). This means that there were random collisions of ions with virus particles and due to the high energy and high concentration of ions available, the virus particles could easily acquire the needed charges for virus inactivation in a short time frame.

4.5.5 The mechanism of viral inactivation by ionization

Little is known of the biological and physical mechanisms by which ions inactivate viruses contained in bioaerosols. It is hypothesized herein that inactivation of the MRV occurred due to an induced dipole torque on the virus capsid proteins. The capsid proteins of MRV virus particles (Fig. 4.29) are critical for the attachment and entry of the virus to host cells (Vidal et al. 2006). The σ1 protein is fiber-like molecule that attaches the virion to the host cell membrane by binding to a primary receptor and to sialic acid containing proteins (coreceptor). The λ2 protein is involved in capping the mRNA to molecules in the cell cytoplasm that are in the process of being synthesized particularly during the early stages of gene expression. The μ1 proteins associate with host membranes to induce cell membrane penetration and the delivery of transcriptionally active viral particles into the host cell cytoplasm. They also induce apoptosis in the host cell. Successful attachment and entry to host cell must occur for virus to move to the replication stage in the cytoplasm. Therefore, damage to any of the capsid proteins could render the viral particles non-

infectious. During air ionization, it is likely that the capsid acted as receptacles on which the ions landed. When the ions landed on the capsid proteins, they created an electric dipole (A dipole is formed when charges of opposite polarity but carry same amounts charge a separated by a distance). Due to the high electric field strength generated, the induced dipole produced a torque which might have distorted the capsid protein molecules and consequently inactivated the virus. At an ion concentration of 2.4×10^{13} ions/m^3, an average electric field strength of 5.8×10^{10} V/m was predicted at a radial distance of 1 cm around the bioaerosols. The threshold of the electric field strength required to distort MRV proteins is yet to be determined.

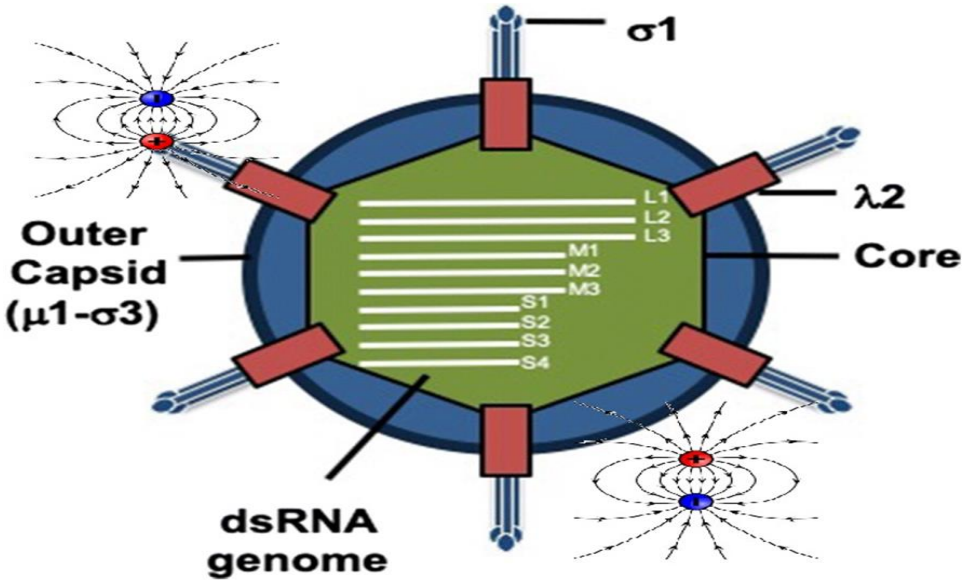

Fig. 4.29 The formation of dipole on a Reovirus capsid proteins. *Reovirus cross sectional diagram modified from (Eledge et al. 2019).*

There is also a probability that hydroxyl radicals (OH) were formed during the ionization process and these radicals attacked the viral proteins and inactivated them. Ion plasma (an avalanche of ions) has been reported to be a potent technology for inactivating influenza virus (Sharp 2004). Positive and negative ions which were generated into an air stream laden with

aerosolized influenza virus were reported to have formed hydroxyl radicals around the virus. The newly formed radicals took a hydrogen molecule from hemagglutinin (a spike protein on the influenza virus) and formed water. The loss of hydrogen from the hemagglutinin inhibited the virus ability to cause an infection. In fungi, it was reported that the radicals took a hydrogen molecule from the cell wall and hence caused inactivation. "Hydroxyl radicals are also known to break DNA or RNA strands directly or attack the phosphate backbones of purines or pyriminidase and ribose or deoxyribose" (Yoo 2018). Hydroxyl radical is the most reactive species of oxygen and a powerful oxidizing agent. Park et al. (2019) conducted a study to determine the effects of plasma (ions) on the generation of OH radicals. In their study, they set up a plasma system by applying a potential of 4.5 kV to a single pin electrode which was connected to a silica tube filled with argon and small fraction of N_2. A cuvette filled with 3 mL of water was subsequently subject to the plasma for 3, 5, 7 and 9 minutes, respectively. They compared the concentration of OH produced from the set-up to the concentration of OH produced from UV. Their results showed that the concentration of OH generated by UV photolysis was approximately 20% of that produced by plasma. In other words, plasma produced a concentration of OH significantly more than UV, a well-known mechanism for producing OH radicals.

For this study, the bioaerosols were generated using PBS and therefore there was a significant amount of water content in the air (relative humidity greater than 80%). During ionization, it was likely that the excited ions reacted with water vapor to form OH radicals, which reacted with the virus capsid protein and produced an inhibiting effect on the virus replication. So far, very little is known about the mechanism through which ions inactivate microorganisms and

therefore further studies to particularly investigate this mechanism(s) is necessary to further our understanding of how air ionization inactivates viruses.

4.6 Effect of ionization on virion concentrations

4.6.1 Comparison between qRT-PCR and plaque assay measurements

To evaluate possible errors in sampling and measurement processes, the airborne virus concentrations measured by qRT-PCR were compared with the equivalent viral concentration estimated from the plaque assay measurement. Specifically, the estimated concentration was obtained by multiplying the plaque assay titers by a virion factor of 450. Because a volume of 5 µL of the sample collected by the biosampler was used to conduct the qRT-PCR while 100 µL was used to conduct the plaque assay and, the concentrations were also normalized to VGCN/mL for comparison.

It was observed that the PCR measurements were slightly lower that those estimated from the plaque assays at all bioaerosol concentration levels for all three stock solutions (Fig. 4.30 a, b and c). But the differences were not statistically significant ($p>0.05$), except for a bioaerosol concentration of 9 /cm^3 for stock solution B with a difference of 52%. This difference was likely due to random errors which occurred during the PCR process. A strong correlation ($R^2 > 0.98$) was also obtained between the plaque assay titers and the viral particle concentrations for all the measured tests. This confirmed that the factor of 450 used for plaque to virion conversion was reasonable.

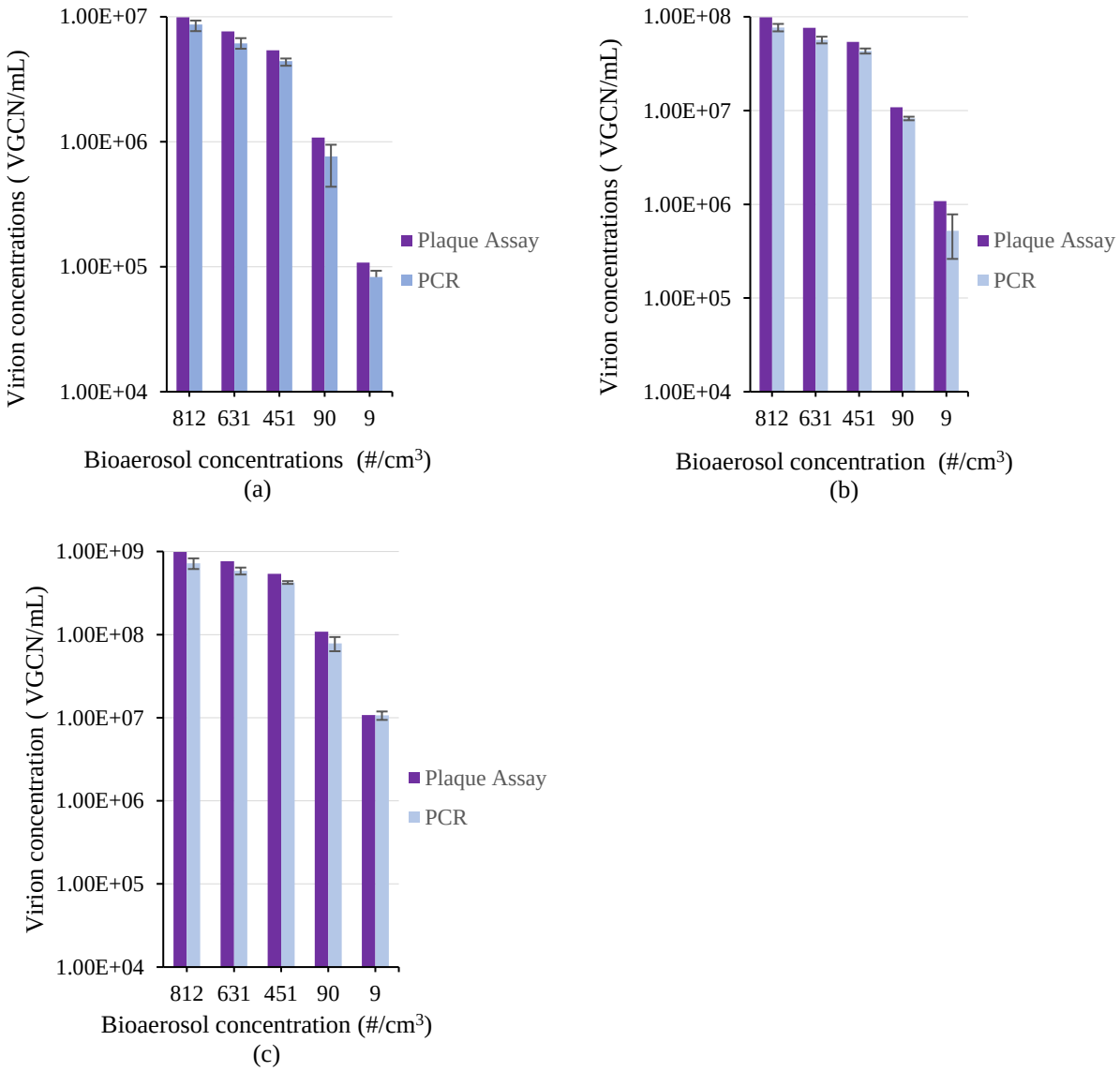

Fig. 4.30 Comparison of virion concentration obtained from PCR with the equivalent concentration estimated from plaque assay. *Error bars show SEM obtained from three replicates of each stock solution.*

4.6.2 Comparison of virion concentrations between natural decay and ionization

The effect of ionization on virion concentration was determined by conducting paired t-tests to compare the virion concentrations between the natural decay (no ionization) and ionization at

each time point (Fig. 4.31 a, b, c). For the natural decay tests, the virion concentration did not significantly change over the time. This meant that the virus particles remained airborne during the entire test period. In contrast, the virion concentration for ionization decreased significantly with time, resulting significant differences in virion concentration between the natural decay and ionization. This meant the virus particles were removed from air by ionization. The virion concentration was reduced by 24% to 26% during the first 10 s of ionization, by 48% to 56% for 20s, and 90% for 90 s.

The effectiveness of ionization for reducing virion concentration was also determined by the survival percentage (SP). The SP expresses the percentage of airborne virions remaining (surviving) in the chamber at a sampling point and was calculated as shown below:

$$SP = \frac{VG_{ins}}{VG_{nds}} \times 100 \qquad 4.4$$

where:

SP = survival percentage (%)

VG_{nds} = virion concentration for natural decay at a sampling point (VGCN/mL)

VG_{ins}= virion concentration for ionization test at a sampling point (VGCN/mL)

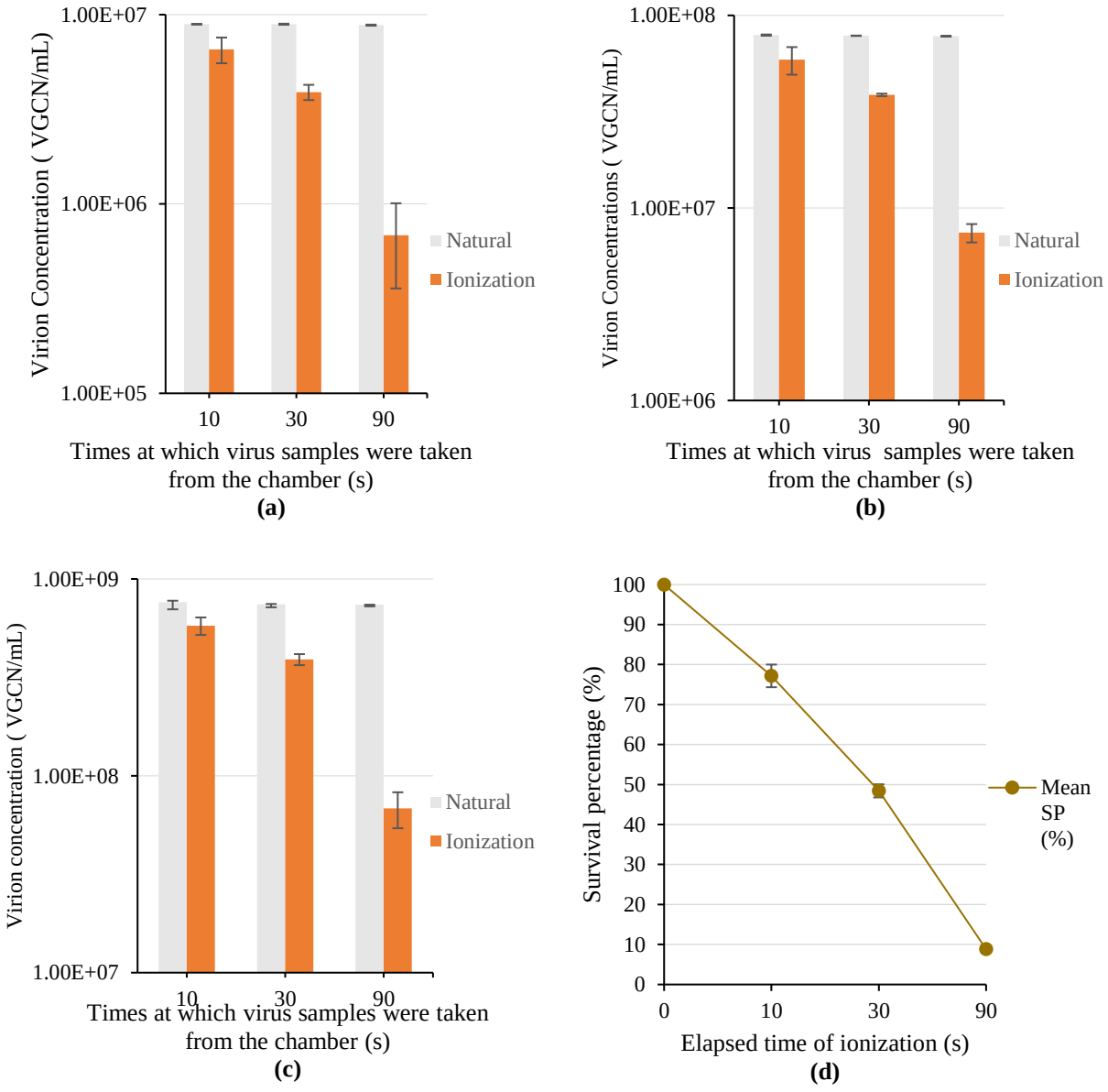

Fig. 4.31 Comparison of virion concentration obtained from PCR between ionization and natural decay for ion concentrations of 2.4× 10^{13} ions/cm^3 (a: Stock A; b: Stock B; c: Stock C) and the mean survival percentage (d) . *Error bars show SEM obtained from three replicates of each stock solution.*

For all the three stock solutions, the SP decreased with the elapsed time of ionization, from 100% at the start to about 10% at 90 s (Fig. 4.31). The general trends for removal were similar for

nine biological replicates and therefore the replicates were averaged to obtain a representative SP value at each sampling point. The obtained SP values for the replicates ranged from 77% at 10 s; 48 at 30 s; and 9% at 90 s. The SP value obtained means that at 10 s, ionization removed 23% of the total initial airborne virions generated into the chamber and therefore 77% survived. At 30 s, 52% of the virions had been removed and therefore 48% of the initially generated airborne virions survived. At 90 s, ionization had removed 91% of the airborne virions, hence only 9% of the virions survived. The decrease of SP over time can be explained by the reason that; under natural decay, the virion concentrations remained almost the same over the sampling time points (Fig. 4.31) however, under ionization there were significant reductions in virion concentrations over the same time points. Consequently, decreasing SP values were obtained over the sampling time points.

4.6.3 Virus removal versus inactivation

While plaque assay measurements reflect both physical removal and biological inactivation of virus by ionization, the PCR measurements reflect only the physical removal. The difference between the two illustrates the degree of biological inactivation.

SP values for both viral titer and virion removal were almost the same at 10 s of ionization (75% vrs 77%) (Fig. 4.32). This means that at 10 s, ionization mainly removed the virions from air and therefore the reduction in infectivity was mainly due to virion removal effect. At 30 s of ionization however, an SP value of about 5% was obtained for the viral titer however, a significantly higher SP value of 50% was obtained for virion concentrations. In other words, the infectivity loss was 10-fold higher at 30 s than the physical particle loss. This also means that apart

from the physical removal of viral particles, ionization also produced a biocidal action on the virus and therefore contributed to the reduction in the viral infectivity.

At 90 s of ionization, an SP value of 0.4% was obtained for the viral titer however an SP value of 9% was obtained for virion concentrations. In other words, the infectivity loss at 90 s was about 20-fold higher than the physical particle loss. This also means that apart from the physical removal of viral particles at 90 s, the biocidal effect of the ions on the virus increased. Therefore, it can be concluded that ionization did not only physically remove virus particles from air but also produced a significant biocidal effect on the virus to reduce viral infectivity over time.

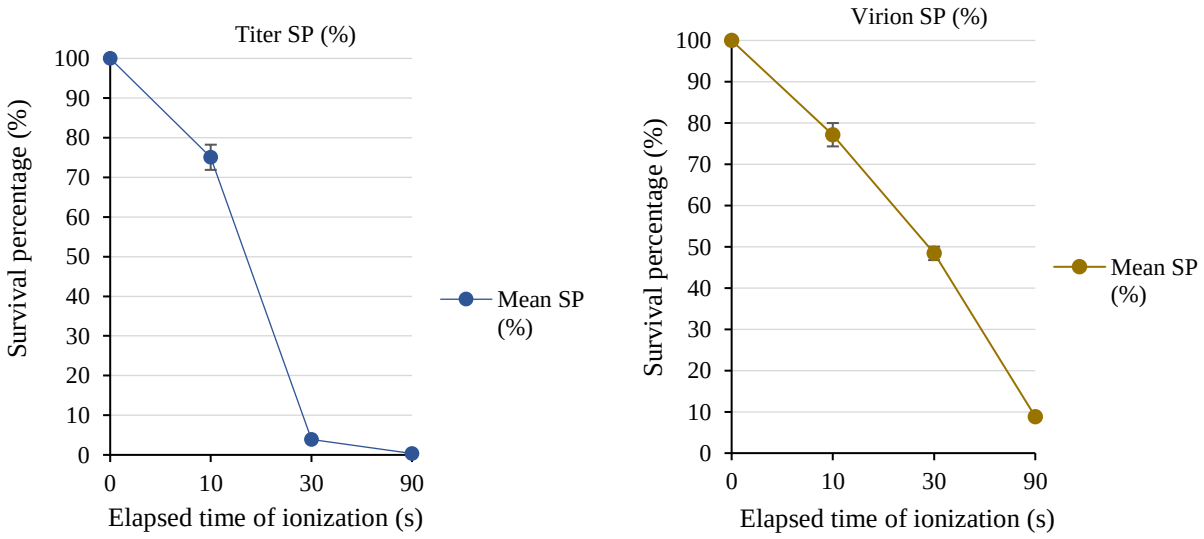

Fig. 4.32 Comparison of the survival percentage for viral titers and survival percentage of virion concentrations at an ion concentration of 2.4×10^{13} ions/m^3. *Error bars indicate SEM obtained from three replicates of each stock solution.*

The results from this study show that air ionization can be used as an effective air purification technology. Air ionization significantly removed high concentrations of bioaerosols and virions. Air ionization also significantly reduced the infectivity of airborne viruses. The study also showed that the reduction in viral infectivity was due to the combined effects of virion removal and a unique biocidal action of the negative ions on the virus.

5. Conclusions and Recommendations

5.1 Numerical model

The finite volume model provided a powerful tool to simulate the various physical processes involved in negative air ionization. The airflow field, the movement of the negative ions, the motion of bioaerosols and the removal of the bioaerosols were successfully coupled in the model. The model adequately predicted the airflow velocity within the chamber. Both the ion and bioaerosol concentrations predicted by the model were in good agreement with the experimental data. Overall, the model was adequate for simulating interconnected complex physical processes during ionization.

5.2 Effects of ionization on virion concentrations

Negative air ionization significantly reduced the virion concentration in air through physical removal of bioaerosols in a relatively short time frame (< 90 s). More than 1.0 $\log_{10}$ reduction (90%) in virion concentrations was observed over a 90 s entire ionization period at an ion concentration of 2.4×10^{13} ions/m.

5.3 Effects of ionization on viral infectivity

This study showed that negative air ionization produced significant effect on the infectivity of MRV. At an ion concentration of 2.4×10^{13} ions/m^3, significant reduction in the viral titers of the virus began to occur at ionization time of 30 s. A 2.0 $\log_{10}$ reduction (99%) in infectivity were obtained over a 90 s ionization time. There was a threshold of ion concentrations (estimated as 2.4×10^{13} ions/m^3 in this study) below which ionization did not produce any effect on the viral

infectivity. The total reduction in infectivity was due to the removal of virions from air and the biocidal action of the ions on the virus. The biocidal effect of the ions in reducing viral infectivity increased with increasing time of ionization.

5.4 Recommendations

The model presented in this study was used to investigate the removal mechanism of bioaerosols under negative air ionization. Predictions for the number of ions attracted to bioaerosols were made on the assumption that bioaerosols are spherical in shape. In reality however, this may not be true for all cases. Bioaerosols take on different shapes and therefore this criterion must be factored into predicting the concentrations of ions that can be attracted to each bioaerosol. Furthermore, another assumption made was that, the bioaerosols generated were monodispersed (of the same aerodynamic diameter). This assumption permitted a convenient tracking of the bioaerosol travel. However, in most aerosol studies, polydisperse (aerosols of different diameters) aerosols are generated simultaneously and therefore to obtain accurate prediction of the bioaerosol removal through ionization, the bioaerosol size distribution within the domain have to be tracked at all times.

For this study, the ions generated were unipolar and mainly negative ions. Consequently, the reported effects of ions on bioaerosols are mainly due to the biocidal effect of only negative ions. To understand the overall effects of ions on bioaerosols, a future ionization study which utilizes both positive and negative ions is recommended.

This study showed that negative air ionization can reduce MRV concentrations and infectivity. However, the threshold of ions at which the ions begin to produce biocidal effects has

not yet been established. To further improve our understanding, it is recommended that a future study be conducted to establish the exact threshold for viral removal and inactivation. Moreover, this study focused on the effect of ionization on a viral family (Reoviradae). To increase our understanding of the viricidal effects of ions, an investigation into the effect of ionization on other types of viruses and microbes is recommended.

An unknown aspect of ionization is the biological mechanism through which virus become inactivated. Viral inactivation could occur through protein denaturation or the destruction of the genome. The effect of electric fields on virus is still little understood. A future study is recommended to evaluate the effects of airborne ions on the protein and genome of virus.

6. References

Adamiak K. (1994). Simulation of corona in wire-duct electrostatic precipitator by means of the boundary element method. *IEEE Transactions on Industry Applications, 30*(2), 381-386. doi:10.1109/28.287519

Adamiak, K. (1991). Application of Boundary Element and Characteristic Methods for Modelling of Corona Fields. In: Springer, Dordrecht. In B. C. Gipson, *Boundary Elements XIII* (pp. 407-418). Dordrecht: Springer. doi:10.1007/978-94-011-3696-9_33

Ahn, Y.C., S.K.Park, G.T.Kim, Y.J.Hwang, C.G.Lee, H.S.Shin & J.K.Lee. (2006). Development of high efficiency nanofilters made of nanofibers. *Current Applied Physics, 6*(6), 1030-1035. doi:10.1016/j.cap.2005.07.013

Alonso C., P.C. Raynor, P.R. Davies , R.B. Morrison & M. Torremorell. (2016). Evaluation of an electrostatic particle ionization technology for decreasing airborne pathogens in pigs. *Aerobiologia, 32*, 405-419. doi:10.1007/s10453-015-9413-3

American Society for Testing and Materials (ASTM). (2008). *Standard guide for statistical evaluation of indoor air quality models.* West Conshohocken, PA: ASTM International.

ANSYS FLUENT. (2009, 01 23). *ANSYS.* Retrieved 05 12, 2018, from http://www.afs.enea.it/project/neptunius/docs/fluent/html/th/node247.htm

ANSYS Fluent. (2016). User's Guide. Version 16.2. Canonsburg, Pennsylvania: Ansys Inc.

ASME. (2006). *Guide for verification and validation in computational solid mechanics.* New York: The American Society of Mechanical Engineers.

Baer, A. and K. Kehn-Hall. (2015). Viral Concentration Determination Through Plaque Assays: Using Traditional and Novel Overlay Systems. *Journal of Visualised Experiments*, 1-19.

Bai, Y.-X and B. Sun. (2011). Study of electrohydrodynamic (EHD) drying technique for shrimps. *Journal of Food Processing and Preservation, 35*(6), 891–897. doi:https://doi.org/10.1111/j.1745-4549.2011.00542.x

Bajgai, T.R. and F. Hashinaga. (2001). High electric field drying of Japanese radish. *Drying Technology, 19* (9), 2291–2302. doi:https://doi.org/10.1081/DRT-100107499

Barthakur N.N. (1989). An electrostatic method of drying saline water. *Drying Technology, 7*(3), 503 -521. doi:https://doi.org/10.1080/07373938908916606

Barthakur N.N. and T. Al-Kanani. (1990). An electrohydrodynamic technique for removal of moisture from soil samples. *Communications in Soil Science and Plant Analysis, 21*(7-8), 649–665. doi:https://doi.org/10.1080/00103629009368260

Barthakur, N.N. and S. Bhartendu. (1988). Enhancement of evaporation rates from thin layers of liquids exposed to air ions. *International Journal of Biometeorology, 32*(3), 163–167. doi:https://doi.org/10.1007/BF01045274

Baumgartner, M. (2016, August 29). Personal communication. (E. D, Interviewer)

Beggs C.B., C.J.Noakes, P.A.Sleigh, L.A.Fletcher & K.G.Kerr. (2005). Methodology for determining the susceptibility of airborne microorganisms to irradiation by an upper-room UVGI system. *Journal of Aerosol Science, 37*, 885-902. doi:10.1016/j.jaerosci.2005.08.002

Beggs, C. (2003). The Airborne Transmission of Infection in Hospital Buildings: Fact or Fiction? *Indoor and Built Environment , 12*(1), 1-10. doi:https://doi.org/10.1177/1420326X03012001002

Blazek J. (2001). *Computational Fluid Dynamics : Principles and Applications.* Oxford: Elsevier.

Bohgard, M. & Eklund, P. (1998). Effect of an ionizer on sub-micron particles in indoor air. . *J. Aerosol Sci., 29*((supp 2)), 1313-1315. doi:http://dx.doi.org/10.1016/S0021-8502(98)90839-4

Boutin, P., M. Torre, R. Serceau and P. J. Rideau. (1988). Atmospheric bacterial contamination from land spreading of animal wastes: Evaluation of the respiratory risk for people nearby. *Agricultural Engineering Research, 39*, 149-160.

Bradford, E., C.R. Christie, E.M.Campbell & A.S. Bowman. (2017). A real-time PCR method for quantification of the total and major variant strains of the deformed wing virus. *Plos One*, 1-19. doi:10.1371/journal.pone.0190017

Brincat, J.P., D. Sardella, A.Muscat, S.Decelis, J.N.Grima, V. Valdramidis & R. Gatta. (2016). A review of the state-of-the-art in air filtration technologies as may be applied to cold storage warehouses. *Trends in Food Science and Technology, 50*, 175-185. doi:10.1016/j.tifs.2016.01.015

Burke T.P and P. F. Frain. (1975). Small ion diffusion variations in air containing condensation nuclei. *Proceedings of the Royal Irish Academy.Section A: Mathematical and Physical Sciences* (pp. 11-31). Dublin: Royal Irish Academy.

Butler A .J., Z. J. Cendes and J. F. Hoburg. (1989). Interfacing the finite-element method with the method of characteristics in self-consistent electrostatic field models. *IEEE Transactions on Industry Applications, 25*(3), 533 - 538. doi: 10.1109/28.31225

Cambra-Lopez, M., A. Winkel, J. van Harn, N.W.M. Ognik and A.J.A Aarnink. (2009). Ionization for reducing particulate matter emissions from poultry houses. *Transactions of American Society of Agricultural and Biological Engineers, 52*(5), 1757-1771.

Cambra-Lopez, M., A.J.A Aarnink, Y. Zhao, S. Calvat and A. G Torres. (2010). Airborne particulate matter from livestock production systems: a review of an air pollution problem. *Environmental Pollution, 158*, 1-17.

Cao, W., Y. Nishiyama, S. Koide & Z. H. Lu. (2004). Drying enhancement of rough rice by an electric field . *Biosystems Engineering, 87*(4), 445 – 451. doi:https://doi.org/10.1016/j.biosystemseng.2003.12.007

Cartwright, C., S. Horrocks, J. Kirton, & B. Crook. (2009). *Review of methods to measure bioaerosols from composting sites.* Bristol: Environment Agency, .

Chang, J. S. (1981). Journal of Aerosol Science. *Theory of diffusion charging of arbitrarily shaped conductive aerosol particles by unipolar ions., 12*(1), 19 - 26. doi:https://doi-org.uml.idm.oclc.org/10.1016/0021-8502(81)90006-9

Chang, J.C. & S. R. Hanna. (2004). Air quality model performance evaluation. *Meteorology and Atmospheric Physics , 87*, 167–196. doi:10.1007/s00703-003-0070-7

Choi B.S. and C.A.J. Fletcher. (1997). Computation of particle transport in an electrostatic precipitator. *Journal of Electrostatics, 40-41*, 413-418. doi:https://doi.org/10.1016/S0304-3886(97)00080-6

Chuaybamroong P., R. Chotigawin, S. Supothina, P. Sribenjalux, S. Larpkiattaworn, C.-Y. Wu. (2010). Efficacy of photocatalytic HEPA filter on microorganism removal. *Indoor Air, 20*(3), 246-254. doi:10.1111/j.1600-0668.2010.00651

Cochet, R. (1961). Lois charge des fine sparticules (Submicroniques) Etudesthe´ oriques—Controles re´ cents spectredeparticules. *Colloque Internationalla Physique des Forces*

Electrostatiques et Leurs Application. 102, pp. 331 -338. Paris: Centre National de la Recherche Scientifique.

Coombs, K. M. (2006). Reovirus Structure and Morphogenesis. In P. Roy, *Reoviruses: Entry, Assembly and Morphogenesis. Current Topics in Microbiology and Immunology* (p. 309). Berlin, Heidelberg: Springer.

Cooper, P. D. (1961). The plaque assay of animal viruses. . *Adv. Virus Res.*, 319–378.

Cox, C. (1987). *The aerobiological pathway of microorganisms.* Chihester: John Wiley and sons.

Cox, C. (1995). Stability of airborne microbes and allegens. In C. Wathes, *Bioaerosol handbook* (pp. 77-79). Boca Raton: CRC Lewis Publishers.

David Rosenwasser & Jill Stephen. (2009). *Writing Analytically.* Boston: Thomson Wadsworth.

Davidson J. H., P. J. McKinney and P. Linnebur. (1996). Three-dimensional (3-D) model of electric field and space charge in the barbed plate-to-plate precipitator. *IEEE Transactions on Industry Applications, 32*(4), 858-866.

Davis, J. L & J. F. Hoburg. (1983). Wire-duct precipitator field and charge computation using finite element and characteristics methods. *Journal of Electrostatics, 14*(2), 187-199.

De Jong, J.C., T. Trouwborst and K.C. Winkler. (1973). The Mechanism of virus decay in aerosols. In W. J.H., *AIrborne transmission and airborne infection* (pp. 543-548). New York: John Wiley and sons.

Dee, S., A. Pitkin, S. Otake and J. Deen. (2011). A four year summary of air filtration system efficacy for preventing airborne spread of porcine reproductive and respiratory syndrome virus and Mycoplasma hyponeumoniae. *Journal of Swine Health and Production, 19*(5), 292 -295.

Dee, S., S. Otake and J. Deen. (2009). Evidence of long distance airborne transport of porcine reproductive and respiratory syndrome virus and Mycoplasma hypneumoniae. *Veterinary Research, 40*(39), 1-13.

Desjardins, P. & D. Conklin. (2010). NanoDrop Microvolume Quantitation of Nucleic Acids. *Journal of Visualized Experiments, 45*, e2556. doi: 10.3791/2565

Digel, I., A. Temiz Artmann, K. Nishikawa, M. Cook, E. Kurulgan & G. M. Artmann. (2005). Bactericidal effects of plasma-generated cluster ions. *Medical & Biological Engineering & Computing, 43*, 800-807.

Eduard, W. & D. Heederik, D. (1998). Methods for quantitative assessment of airborne levels of non-infectious microorganisms in highly contaminated work environments. *American Industrial Hygiene Association Journal, 59*(2), 113–127.

Eledge, M.R., M.D Zita & K.W. Boehme. (2019). Reovirus: Friend and Foe. *Current Clinical Microbiology Reports , 6*, 132-168. doi:doi.org/10.1007/s40588-019-00121-8

Essien D., Zhang Q., Coomb K. & Levin D. (2017). Effectiveness of Negative Air Ionization for Removing Viral Bioaerosols in an Enclosed Space. *CSBE/SCGAB 2017 Annual Conference* (pp. 1-7). Winnipeg: CSBE/SCGAB 2017 Annual Conference.

Essien, D., Zhang, Q., Levin, D., & Coombs, K. (2018). Numerical Modelling of Negative Air Ionization for Removing Viral Bioaerosols in an Enclosed Space. *10th International Livestock Symposium (ILESX)* (pp. 1-8). Omaha: ASABE.

Farnoosh, N., K. Adamiak, & G. Castle. (2011). Three-dimensional analysis of electrohydrodynamic flow in a spiked electrode-plate electrostatic precipitator. *Journal of Electrostatics, 69*(5), 419–428. doi:https://doi.org/10.1016/j.elstat.2011.06.002

Fisk, W. J., D.Faulkner, J. Palonen & O. Seppanen, O. . (2002). Performance and costs of particle air filtration technologies. *Indoor Air, 12*(4), Pages 223-234. doi:10.1034/j.1600-0668.2002.01136.x

Fjeld, R. A., & A. R. McFarland. (1989). Evaluation of selected approximations for calculating particlec harging rates in thecontinuum regime. *Aerosol Science and Technology, 10*, 535–549. doi:https://doi-org.uml.idm.oclc.org/10.1080/02786828908959293

Fletcher, L., L. Gaunt, C. B. Beggs, S .J. Shepherd, P. A. Sleigh, C. J. Noakes & K. G. Kerr. (2007). Bactericidal action of positive and negative ions in air. *BMC Microbiology, 7*(32), 1-9. doi:10.1186/1471-2180-7-32

Franken N.A, H.M Rodermond , J. Stap, J. Haveman, C. van Bree. (2006). Clonogenic assay of cells in vitro. *Nat. Protoc., 1*(5), 2315-2319. doi:doi: 10.1038/nprot.2006.339

Fuchs, N. A. (1963). On the stationary charge distribution on aerosol particles in a bipolar ionic atmosphere. *Geofisica PuraeApplicata, 56*(1), 185 -193. doi:https://doi.org/10.1007/BF01993343

Galbusera F. and F. Niemeyer. (2018). *Mathematical and Finite Element Modeling.* Amsterdam: Elsevier.

Gast R.K., B.W. Mitchell & P.S. Holt. (1999). Application of negative air Ionization for reducing experimental airborne transmission of Salmonella enteritidis to chicks. *Poultry Science , 78*(1), 57–61. doi:https://doi.org/10.1093/ps/78.1.57

Gilbert, Y & C. Duchaine. (2009). Bioaerosols in industrial environments: a review. *Canadian Journal of Civil Engineering, 36,* 1873–1886.

Grabarczyk, Z. (2001). Effectiveness of indoor air cleaning with corona ionizers. *J. Electrost, 51-52*, 278-283. doi:https://doi.org/10.1016/S0304-3886(01)00058-4

Gray, D. & A. Giorgini. (1976). The validity of the Boussinesq approximation for liquids and gases. *International Journal of Heat and Mass Transfer, 19*(5), 545-551.

Grigoriadis D.G.E. & S.C.Kassinosa. (2009). Lagrangian particle dispersion in turbulent flow over a wall mounted obstacle. *International Journal of Heat and Fluid Flow, 30*(3), 462-470. doi:10.1016/j.ijheatfluidflow.2009.01.010

Grinshpun, S. A., Mainelis, G., Trunov M., Adhikari ,A., Reponen, T., & Willeke, K. (2005). Evaluation of ionic air purifiers for reducing aerosol exposure in confined indoor spaces. *Indoor Air, 15*(4), 235-245. doi:https://doi-org.uml.idm.oclc.org/10.1111/j.1600-0668.2005.00364.x

Grishpun, S.A., M.P. Buttner, K. Willeke, A.L. Mill. (2007). Manual of Environmental Microbiology. In C. J. Husrt, *Manual of Environmental Microbiology* (3 ed., pp. 939–951). Washington DC: ASM press.

Guarino, M., L.D. Jacobson, and K.A. Janni. (2007). Dust reduction from oil-based feed additives. *Transactions of the ASAE, 23*(3), 329-332.

Hagbom, M., J. Nordgren, R. Nybom, K. Hedlund, H. Wigzell & L. Svensson. (2015). *Ionizing air affects influenza virus infectivity and prevents airborne transmission.* London: Nature (Scientific reports). doi:10.1038/srep11431

Han, J., G.A. Colditz, L.D. Samson & D.J. Hunter. (2004). Polymorphisms in DNA double-strand break repair genes and skin cancer risk. *Cancer Research, 64*, 3009-3013. doi:10.1158/0008-5472.CAN-04-0246

Hart, J.F., T.J. Ward, T.M. Spear & R.J. Rossi, N.N. Holland & B.G. Loushin. (2011). Evaluating the Effectiveness of a Commercial Portable Air Purifier in Homes with Wood Burning Stoves: A Preliminary Study. *Journal of Environmental and Public Health*, 1-7.

Hathway E.A, C.J. Noakes, P.A. Sleigh & L.A. Fletcher. (2011). CFD simulation of airborne pathogen transport due to human activities. *Building and Environment, 46*, 2500-2511. doi:10.1016/j.buildenv.2011.06.001

Heber, A., M.Stroik, J.L. Nellssen, D.A. Donaldson. (1988). Influence of environmental factors on concentrations and inorganic content of aerial dust in swine finishing building. *Transactions of the American Society of Agricultural Engineers, 31*, 882-887.

Heidelberg, J.F., M. Shamat, M. Levin, I. Rahman, G. Stelma, C. Grim and R.R Colwell. (1997). Effect of the aerosolization on culturability and viability of gram negative bacteria. *Applied and Environmental Microbiology, 63*, 3585 - 3588.

Henningson E.W., I. Fangmark, E. Larsson & L .E. Wikstrom. (1998). Collection efficiency of liquid samplers for microbiological aerosols. *Journal of Aerosol Science, 19*(7), 911–914.

Hensel, A., N. Stockhofe, M. Ganter and K. Petzoldt. (1995). Aerosol exposure of pigs to viable or inactivated Actinobaccillus pleuropneumoniae. *Veterinary Microbiology, 47*, 27-41.

Herman, J. , C.A. Munoz-Zanzi and J.J. Zimmerman. (2009). A method to provide improved dose-response estimates for airborne pathogens in animals: An example using using porcine reproductive and respiratory syndrome virus. *Veterinary Microbiology, 133*, 297-302.

Herman, J.R. and J.J. Zimmerman. (2008). Analytical sensitivity of air samples based on uniform point-source exposure to airborne porcine reproductive and respiratory syndrome virus and swine influenza. *The Canadian Journal of Veterinary Research, 72*, 440-443.

Herman, J.R., S.J. Hoff, K.J. Yoon, A.C. Burkhardt, R.B. Evans and J.J. Zimmerman. (2006). Optimization of a sampling system for recovery and detection of airborne porcine reproductive and respiratory syndrome virus and swine influenza. *Applied and Environmental Microbiology, 72*(7), 4811-4818.

Herman, J.R., S.L. Brockmeier, K. J. Yoon and J.J. Zimmerman. (2008). Detection of respiratory pathogens in air samples from acutely infected pigs. *The Canadian Journal of Veterinary Research, 72*, 367-370.

Hinds, C. W. (1999). *Aerosol Technology - Properties, Behavior and Measurement of Airborne Particles* (2nd ed.). Toronto: John Wiley & Sons.

Hinds, W.C. (1982). .*Aerosol Technology*. New York, NY: John Wiley & Sons, Ltd.

Hogan, C. J., Jr., E. M. Kettleson, M. H. Lee, B. Ramaswami, L. T. Angenent, and P. Biswas. 2005. (2005). Sampling methodologies and dosage assessment techniques for submicrometre and ultrafine virus aerosol particles. *Journal of Applied. Microbiology, 99*, 1422–1434.

Hyun J., S.G Lee & J. Hwang. (2017). Application of corona discharge-generated air ions for filtration of aerosolized virus and inactivation of filtered virus. *Journal of Aerosol Science, 107*, 31-40. doi:https://doi.org/10.1016/j.jaerosci.2017.02.004

Illias H. A., S. Dabak & G. Altamimi. (2015). Modeling of corona partial discharge under various electrode types with Finite Element Analysis . *Proceedings of COMSOL* . Kuala Lumpur: COMSOL.

Iwama, H., H. Ohmizo, S. Furuta, S. Ohmori, K. Watanabe, T. Kaneko, K. Tsutsumi. (2002). Inspired superoxide anions attenuate blood lactate concentrations in postoperative patients. *Critical Care Medicine, 30*(6), 1246–1249.

James D. Lester, James D. Lester Jr & Patricia I. Mochnacz. (2003). *The Essential Guide to Writing Research Papers: Canadian Edition.* Toronto: Longman.

Jamriska, M., D. Martin & L.Morawska,. (1997). Investigation of the filtration efficiency of HEPA and ULPA filters in submicrometer size range. *Clean Air Environ. Qual., 31*, Pages 31-37.

Jana K., D. Schepers & A . R. McFarland. (2010). Sampling and Retention Efficiencies of Batch-Type Liquid-Based Bioaerosol Samplers. *Aerosol Science & Technology, 10*(44), 817-829. doi:10.1080/02786826.2010.497513

Jiang S.Y., A.Ma, & S. Ramachandran. (2018). Negative Air Ions and Their Effects on Human Health and Air Quality Improvement. *International Journal of Molecular Sciences, 19*(10), 1-19. doi:10.3390/ijms19102966

Johansson B., S. Jain, J. Montoya-Torres, J. Hugan & E. Yücesan. (2010). Verification and validation of simulation model. *Proceedings of the 2010 Winter Simulation Conference* (pp. 167-183). Baltimore, Maryland: IEEE.

Jung J.H., J.E Lee & G.N. Bae. (2011). Real-time measurement of UV-inactivated Escherichia coli bacterial particles by electrospray-assisted UVAPS spectrometry. *Science of The Total Environment, 409*(17), 3249-3255. doi:https://doi.org/10.1016/j.scitotenv.2011.05.005

Kesavan J., D. Schepers & Andrew R. McFarland. (2010). Sampling and retention efficiencies of batch-Type liquid-based bioaerosol samplers. *Aerosol Science and Technology, 44*(10), 817-829. doi:https://doi.org/10.1080/02786826.2010.497513

Khan A., Sapra B.K., Sawant,V.D., Shaikh, A.N., Mayya, Y.S. (2000). Behaviour of cigarette smoke in a test enclosure. *Bulletin of Indian Aerosol Science and Technology*, pp. 160-163.

Kim W., H. An, D. Lee, W. Lee & J.H. Jung. (2015). Development of a Novel Electrostatic Precipitator. *Aerosol Science and Technology, 49*(11), 1100-1108. doi: https://doi.org/10.1080/02786826.2015.1101051

Kim, S. H. & K.W. Lee. (1999). Experimental study of electrostatic precipitator performance and comparison with existing theoretical prediction models. *Journal of Electrostatics, 48*(1), 3 -25. doi:https://doi.org/10.1016/S0304-3886(99)00044-3

King M-F, C.J. Noakes, P.A. Sleigh & M.A. Camargo-Valero. (2012). Bioaerosol deposition in single and two-bed hospital rooms: A numerical and experimental study. *Building and Environment, 59*, 436-447. doi:http://dx.doi.org/10.1016/j.buildenv.2012.09.011

Knight, V. (1980). Viruses as agents of airborne contagion. *Annals of the New York Academy of Sciences, 353*(1), 147-156.

Knight, V. (1973). Airborne transmission and pulmonary deposition of viruses. *IVth International Symposium on Aerobiology* (pp. 175-182). Utrect: Oosthoek Publishing Company.

Krueger A.P., W. W. Hick & J. C. Beckett. (1958). Effects of unipolar air ions on microorganisms and on evaporation. *Journal of the Franklin Institute, 266*(1), 9 - 19. doi: 10.1016/0016-0032(58)90803-2

Kujundzic E., F. Matalkah, C.J. Howard, M. Hernandez & S.L. Miller. (2007). UV air cleaners and upper-room air ultraviolet germicidal irradiation for controlling airborne bacteria and

fungal Spores. *Journal of Occupational and Environmental Hygiene, 10*(3), 536-546. doi:doi.org/10.1080/15459620600909799

La, A. (2014). Effectiveness of negative air ionization in reducing airborne porcine reproductive and respiratory syndrome virus (PRRSV) and aerosols. MS thesis. Winnipeg, Canada:University of Manitoba, Biosystems Engineering Department. Canada.

Lai A.C.K , L.T. Wong, K.W. Mui, W.Y. Chan & H.C. Yu. (2012). An experimental study of bioaerosol (1-10 microns) deposition in a ventilated chamber. *Building and Environment, 56*, 118-126. doi:10.1016/j.buildenv.2012.02.027

Lami, E., F. Mattachini, R. Sala & H. Vigl. (1997). A mathematical model of electrostatic field in wires–plate electrostatic precipitators. *Journal of Electrostatics , 39*(1). doi:https://doi.org/10.1016/S0304-3886(96)00044-7

Lawless, P. A. (1996). Particle charging bounds,symmetry relations and ananalytic charging rate model for the continuum regime. *Journal of Aerosol Science, 27*(2), 191-215. doi:https://doi-org.uml.idm.oclc.org/10.1016/0021-8502(95)00541-2

Leary T.P., J.C Erker, M.L. Chalmers , A.T Cruz , J.D Wetzel , S.M Desai , I.K Mushahwar , T.S. Dermody. (2002). Detection of mammalian Rreovirus RNA by using reverse transcription-PCR: Sequence diversity within the λ3-encoding L1 Gene. *Journal of Clinical Microbiology., 40*(4), 1368-1375. doi: 10.1128/JCM.40.4.1368-1375.2002

Lee B.H., H.J. Kil, J.H. Eom & C.H. Ahn. (2003). Characteristics of an ionic wind in a DC corona discharge in needle to punched plate geometry. *Journal of the Korean Institute of Illuminating and Electrical Engineers, 17*(4), 74-80.

Lee, B.U., M. Yermakov and S.A Grinshhpun. (2004). Removal of fine and ultrafine particles from indoor environments by unipolar ion emission. *Atmospheric Environment, 38*, 4815-4823.

Levin P.L & J.F. Hobur. (1990). Donor cell-finite element descriptions of wire-duct precipitator fields, charges, and efficiencies. *IEEE Transactions on Industry Applications, 26*(4), 662 - 670. doi: 10.1109/28.55991

Li X., Y. Shang, Y. Yan, L. Yang & J. Tu. (2018). Modelling of evaporation of cough droplets in inhomogeneous humidity fields using the multi-component Eulerian-Lagrangian approach. *Building and Environment, 128*, 68 -76. doi:https://doi.org/10.1016/j.buildenv.2017.11.025

Li, F., E.S. Lee, J. Liu, & Y. Zhu. (2015). Predicting self-pollution inside school buses using a CFD and multi-zone coupled model. *Atmospheric Environment*(107), 16-23. doi:http://dx.doi.org/10.1016/j.atmosenv.2015.02.024

Lia J., A. Leaveya, Y. Wanga, C. O'Neil, M. A. Wallace, C. A. D. Burnham, A. C. M. Boon, H. Babcock & P. Biswasa. (2018). Comparing the performance of 3 bioaerosol samplers for influenza. *Journal of Aerosol Science, 115*, 133-145. doi:http://dx.doi.org/10.1016/j.jaerosci.2017.08.007

Lidwell O.M. (1994). Ultraviolet radiation and the control of airborne contamination in the operating room. *Journal of Hospital Infection, 28*(4), 245-248. doi:10.1016/0195-6701(94)90088-4

Lin C.Y. & C.S Li. (2002). Control effectiveness of ultraviolet germicidal irradiation on bioaerosols. *Aerosol Science and Technology, 36*(4), 474-478. doi:10.1080/027868202753571296

Lindsley, W.G., T. A. Pearce, J. B. Hudnall, K. A. Davis, S. M. Davis, M.A. Fisher, D.H. Beezhold. (2012). Quantity and size distribution of cough-generated aerosol particles produced by influenza patients during and after illness. *Journal of Occupational and Environment Hygiene, 9*(7), 443-449. doi:10.1080/15459624.2012.684582

Liu C.Y., C.H. Tseng, H.C. Wang, C.F. Dai & Y.H Shih. (2019). The study of an ultraviolet radiation technique for removal of the indoor air volatile organic compounds and bioaerosol. *International Journal of Environmental Research and Public Health, 16*(14), 1-16. doi: 10.3390/ijerph16142557

Long Z. & Q. Yao. (2010). Evaluation of various particle charging models for simulating particle dynamics in electrostatic precipitators. *Journal of Aerosol Science, 41*, 702 -718. doi:https://doi-org.uml.idm.oclc.org/10.1016/j.jaerosci.2010.04.005

Long Z., Q. Yao, Q. Song & L. Shuiqing. (2009). A second-order accurate finite volume method for the computation of electrical conditions inside a wire-plate electrostatic precipitator on unstructured meshes. *Journal of Electrostatics, 67*, 597–604. doi:10.1016/j.elstat.2008.12.006

Lowen, A.C., S. Mubereka, J. Steel and P. Palese. (2007). Influenza virus transmission is dependent on relative humidity. *PlosPathogens, 3*(10), 1470-1476.

Lowen, A.C., S. Mubereka, J. Steel and P. Palese. (2008). High temperature blocks aerosol but not contact transmission of influenza. *Journal of Virology, 80*(11), 5650-5652.

Macher, J.M and H.C. Hansson. (1987). Personal size-separating impactor for sampling micobiological aerosols. *American Industrial Hygiene Association Journal, 48*, 652-655.

Mamahlodi M.T. (2019). Potential benefits and harms of the use of UV radiation in transmission of tuberculosis in South African health facilities. *Journal of Public Health in Africa, 10*, 61-67. doi: 10.4081/jphia.2019.742

Mandal J. & Brandl H. (2011). Bioaerosols in Indoor Environment - A review with special reference to residential and occupational locations. *The Open Environmental & Biological Monitoring Journal, 4*, 83-96. doi:10.2174/1875040001104010083

Mayya Y. S., B. K. Sapra, A. Khan & F. Sunny. (2004). Aerosol removal by unipolar ionization in indoor environments. *Journal of Aerosol Science, 35*(8), 923 - 941. doi:https://doi-org.uml.idm.oclc.org/10.1016/j.jaerosci.2004.03.001

McMurry P.H & D.J. Rader. (1985). Aerosol wall losses in electrically charged chambers. *Aerosol Science and Technology, 4*(3), 249 -268. doi:doi.org/10.1080/02786828508959054

Miaśkiewicz -Peska, E. & M Łebkowska. (2011). Effect of Antimicrobial Air Filter Treatment on Bacterial Survival . *Fibres and Textiles in Eastern Europe, 19*(1), 73-77.

Moraes A.O.S & P.L.C Lage. (2013). Analysis of the non-orthogonality correction of finite volume discretization on unstructured meshes. *22nd International Congress of Mechanical Engineering (COBEM 2013)* (pp. 3519-3530). Ribeirão Preto, SP, Brazi: ABCM.

Morawska, L., G.R. Johnson, Z.D. Ristovski, M. Hargreaves, K. Mengersen, S. Corbett, C.Y.H. Chao, Y. Li, D. Katoshevski. (2009). Size distribution and sites of origin of droplets expelled from the human respiratory tract during expiratory activities. *Aerosol Science, 40*, 256 -- 269. doi:10.1016/j.jaerosci.2008.11.002

Mortensen, S.H., R. Stryhn, R. Sorgaard, A. Boklund, K.D. Stark and J. Christensen. (2002). Risk factors for infection of sow herds with porcine reproductive and respiratory syndrome virus (PRRSV). *Preventive Veterinary Medicine, 54*, 83-101.

Murray, B. K., S. Ohmine, D. P. Tomer, K. J. Jensen, F. B. Johnson, J. J. Kirsi , R. A. Robison, K. L. O'Neill. (2008). Virion disruption by ozone-mediated reactive oxygen species. *Journal of virological methods, 153*, 74 -77.

Nicas M., W. W. Nazaroff, A. Hubbard . (2005). Toward understanding the risk of secondary airborne infection: emission of respirable pathogens. . *J. Occup Environ Hyg., 2*, 143–54. doi:10.1080/15459620590918466

Nicas M., W.W. Nazaroff & A. Hubbard. (2005). Toward understanding the risk of secondary airborne infection: emission of respirable pathogens. *Journal of Occupational Environmental Hygiene. , 2*, 143–54.

Nikas, K. S. P., A. A. Varonos, & G. C. Bergeles. (2005). Numerical simulation of the flow and the collection mechanisms inside a laboratory scale electrostatic precipitator. *Journal of Electrostatics*, 423 -443. doi:https://doi.org/10.1016/j.elstat.2004.12.005

Nikas, K. S. P., Varonos, A. A., Bergeles G. C. (2005). Numerical simulation of the flow and the collection mechanisms inside a laboratory scale electrostatic precipitator. *J. Electrost, 63*(5), 423-443. doi:https://doi.org/10.1016/j.elstat.2004.12.005

Noakes C.J; L.A. Fletcher, C.B. Beggs, P.A. Sleigh & K.G. Kerr. (2004). Development of a numerical model to simulate the biological inactivation of airborne microorganisms in the presence of ofultraviolet light. *Aerosol Science 35 , 35*, 489 - 507. doi:doi:10.1016/j.jaerosci.2003.10.011

Noakes, C .J., P.A. Sleigh & C. Beggs. (2007). Modelling the air cleaning performance of negative air ionisers in ventilated Rooms. *Proceedings of the 10th International Conference on Air Distribution in Rooms* - (pp. 1-10). Helsinki: Roomvent. Retrieved 02 05, 2018, from http://eprints.leedsbeckett.ac.uk/2669/6/Noakes_roomvent_07.pdf

Nomura Y., P. K. Hopke , B. Fitzgerald & B. Mesbah. (2007). Deposition of particles in a chamber as a function of ventilation rate. *Aerosol Science and Technology, 27*(1), 62-72. doi:10.1080/02786829708965458

Otake, S., S. Dee, C. Corzo, S. Oliveira and J. Deen. (2010). Long distance airborne transport of infections PRRSV and Mycosplama hyponeumoniae from a swine population infected with multiple variants. *Veterinary Microbiology, 145*, 198-208.

Ounis, H., G. Ahmadi and J. B. McLaughlin. (1991). Brownian diffusion of submicrometer particles in the viscous sublayer. *Journal of Colloid and Interface Science, 143*(1), 266 - 277.

Owen, B. (2015, 07 23). *Hard to keep labourers at Keeyask*. Retrieved 03 15, 2019, from Winnipeg Free Press: https://www.winnipegfreepress.com/local/hard-to-keep-labourers-at-keeyask-318244131.html

Park, J. H & C. H. Chun. (2002). An improved modelling for prediction of grade efficiency of electrostatic precipitators with negative corona. *Journal of Aerosol Science* , 673 -694. doi:https://doi-org.uml.idm.oclc.org/10.1016/S0021-8502(01)00205-1

Park, J. H., K. Y. Yoon, Y. S. Kim, J. H. Byeon & J. Hwang. (2009). Removal of submicron aerosol particles and bioaerosols using carbon fiber ionizer assisted fibrous medium filter media. *Journal of Mechanical Science and Technology , 23*, 1846–1851. doi:10.1007/s12206-009-0613-z

Park, S., J. Y Park, & W. Choe. (2019). Origin of hydroxyl radicals in a weakly ionized plasma-facing liquid. *Chemical Engineering Journal, 378*, 1-8.

Pauthenier, M., & M. Moreau-Hanot. (1932). La charge des particles sphe´ riques dans un champ ionize. . *Journal of Physique Radium, 3*, 590–615.

Picard-Meyer, E., C.P de Garam, J.L. Schereffer, C. Marchal, E. Robardet & F. Cliquet. (2015). Cross-platform evaluation of commercial real-time of European bat Lyssavirus type 1. *BioMed Research International*, 1-18. doi:10.1155/2015/839518

Pitkin, A.N., J. Deen and S.A. Dee. (2009). Use of a production region model to assess the spread of porcine reproductive and respiratory syndrome virus. *Veterinary Microbiology, 136*, 1-7.

Podgórski A., A. Bałazy & L. Gradoń. (2006). Application of nanofibers to improve the filtration efficiency of the most penetrating aerosol particles in fibrous filters. *Chemical Engineering Science, 61*(20), 6804-6815. doi:10.1016/j.ces.2006.07.022

Potrymai, E. & I. Perstnov. (2014). Time dependent dodelling and simulation of the corona discharge in electrostatic precipitators. *A master's thesis submitted to the department of Physics and Electrical Engineering, Linnaeus University*. Sweden.

Pushpawela, B., R. Jayaratne, A. Nguy & L. Morawska. (2017). *Journal of Electrostatics, 90*, 79-84. doi:doi.org/10.1016/j.elstat.2017.10.002

Radhakrishnan, T. V., C. Balaji & S.P.Venkateshan. (2010). Optimization of multiple heaters in a vented enclosure – A combined numerical and experimental study. *49*(4), 721-732. doi:https://doi-org.uml.idm.oclc.org/10.1016/j.ijthermalsci.2009.09.012

Redrow J., S. Maob, I. Celik, J. A. Posada & Z. Feng. (2011). Modeling the evaporation and dispersion of airborne sputum droplets expelled from a human cough. *Building and Environment, 46*, 2042-2051. doi:10.1016/j.buildenv.2011.04.011

Rosenberg, D. M., R. A. Bodaly and P. J. Usher. (1995). Environmental and Social Impacts of Large ScaleHydroelectric Development:Who is Listening? . *Global Environmental Change, 5*(2), 127–148.

Sanchez-Monedero, M. A. & E. I. Stentiford. (2003). Generation and dispersion of air-borne microorganisms from composting facilities. *Process Safety and Environmental Protection, 81* (B3), 166–170. doi:10.1205/095758203765639861

Schmid, H. J. (2003). On the modeling of the particle dynamics in electro-hydrodynamic flowfields:II. Influences of inhomogeneities on electrostatic precipitation. .*Powder Technology, 135 &136,, 135 - 136*, 136 -149. doi:https://doi-org.uml.idm.oclc.org/10.1016/j.powtec.2003.08.010

Schneiderbauer, S. & M. Krieger. (2013). What do the Navier–Stokes equations mean? *European Journal of Physics, 35*(1), 1 -26. doi:10.1088/0143-0807/35/1/015020

Schneiderbauer, S., & Krieger, M. (2013). What do the Navier–Stokes equations mean? *Eur. J. Phys., 35* (015020), 1-26. doi:https://doi.org/10.1088/0143-0807/35/1/015020

Sharma, A., E. Clark, J.D. McGlothlin & S.K. Mittal. (2015). *Efficiency of Airborne Sample Analysis Platform (ASAP) bioaerosol sampler for pathogen detection.* Switzerland: Frontiers. doi:10.3389/fmicb.2015.00512

Sharp. (2004). *Plasmacluster ions inactivate an airborne corona virus—A world first.* Osaka: Sharp Corporation.

Shrivastava, S.R., P. Shrivastava & J. Ramasamy. (2013). Airborne Infection Control in Healthcare Settings. *Infection Ecology & Epidemiology*(1), 1-2. doi:https://doi.org/10.3402/iee.v3i0.21411

SKC. (2019, 02 15). Retrieved from https://www.skcinc.com/catalog/pdf/instructions/1603.pdf

Skodras, G., S .P. Kaldis, D. Sofialidis, O. Faltsi, P. Grammelis & G. P. Sakellaropoulos. (2006). Particulate removal via electrostatic precipitators—CFD simulation. *Fuel Processing Technology, 87*(7), 623–631. doi:https://doi-org.uml.idm.oclc.org/10.1016/j.fuproc.2006.01.012

Skrodas G., S.P. Kaldis, D.Sofialdis, O. Faltsi, P. Grammelis & G.P. Sakellaropoulos. (2006). Particulate removal via electrostatic precipitators — CFD simulation. *Fuel Processing Technology, 87*(7), 623-631. doi:https://doi.org/10.1016/j.fuproc.2006.01.012

Smith, D.J. (2008). Ultimate resolution in the electron microscope? *Materials today*, 30-38. doi:doi.org/10.1016/S1369-7021(09)70005-7

Spronk, G., S. Otake and S. Dee. (2010). Prevention of PRRSV infection in large breeding herds using air filtration. *Veterinary Record, 166*, 758 -759.

Srikanth P., S. Sudharsanam & R. Steinberg. (2008). Bioaerosols in indoor environment:composition, health effects and analysis. *Indian Journal of Medical Microbiology, 26*, 302-312.

Stark, K. (1999). The role of infectious aerosols in disease transmission in pigs. *Veterinary Journal, 85*, 164-181.

Talaie, M. R. (2005). Mathematical modeling of wire–duct single-stage electrostaticprecipitators. . *Journal of Hazardous Materials, 124*(1-3), 44-52. doi:https://doi-org.uml.idm.oclc.org/10.1016/j.jhazmat.2005.01.007

Tang J .W. , C.J. Noakes, P.V. Nielsen , I. Eames , A. Nicolle, Y. Li & G.S. Settles. (2011). Observing and quantifying airflows in the infection control of aerosol- and airborne-transmitted diseases: an overview of approaches. *Journal of Hospital Infection, 77*, 213 - 222. doi:https://doi.org/10.1016/j.jhin.2010.09.037

Tang, W. (2009). The effect of environmental parameters on the survival of airborne infectious agents. *Journal of Royal Society Interface*, 737-746.

Tellier, R. (2006). Review of aerosol transmission of influenza A virus. *Emerging Infectious Diseases , 12*(11), 1657 - 1662.

Toljic N., K. Adamiak , G. S. Peter Castle , H. Kuo , H. Fan. (2012). 3D Numerical model of the electrostatic coating process with moving objects using a moving mesh. *Journal of Electrostatics, 70*, 499 -504. doi:http://dx.doi.org/10.1016/j.elstat.2012.08.001

Tseng C.C & C.S Li. (2005). Inactivation of virus-containing aerosols by ultraviolet germicidal irradiation. *Aerosol Science and Technology, 39*(12), 1136-1142. doi:10.1080/02786820500428575

Vaddi R.S., Y. Guan & I. Novosselov. (2020). Behavior of ultrafine particles in electro-hydrodynamic flow induced by corona discharge. *Journal of Aerosol Science, 148*, 1-13. doi:https://doi.org/10.1016/j.jaerosci.2020.105587

Verdenelli, M. C., C. Cecchini, C. Orpianesi, G. M. Dadea & A. Cresci. (2003). Efficacy of antimicrobial filter treatments on microbial colonization of air panel filters. . *Journal of Applied Microbiology, 94*, 9–15.

Versteeg, H. and W. Malalasekra. (2007). *An introduction to computational fluid dynamics* (2nd Edition ed.). Toronto: Pearson -Prentice Hall.

Vidal, L., T. A. Yap, C. L. White, K. Twigger, M. Hingorani, V. Agrawal, S. B. Kaye, K. J. Harrington & J. S. de Bono. (2006). Reovirus and other oncolytic viruses for the targeted treatment of cancer. *Targeted Oncology, 1*, 130–150. doi:10.1007/s11523-006-0026-1

Walker C.M & G. Ko. (2007). Effect of ultraviolet germicidal irradiation on viral aerosols. *Environmental Science Technology, 41*, 5460-5465. doi:https://doi-org.uml.idm.oclc.org/10.1021/es070056u

Walter, J. & G. Reischl. (1978). Measurements of the filtration efficiencies of selected filter types. *Atmospheric Envirionment, 12*(10), 2015-2019. doi:10.1016/0004-6981(78)90139-7

Wang, L. H. (2016). Space and time domain finite volume method for numerical simulation of negative corona discharge in air. *Journal of Electrical Engineering and Technology 11(5):, 11*(5), 1348-1356. doi:10.5370/JEET.2016.11.5.1348

Wang, N., A. Raza, Y. Si, J. Yu., G. Sun & B. Ding. (2013). Tortuously structured polyvinyl chloride/polyurethane fibrous membranes for high-efficiency fine particulate filtration. *Journal of Colloid and Interface Science, 398*, 240-246. doi:10.1016/j.jcis.2013.02.019

Wells, W. (1955). *Airborne contangion and air hygiene - an ecological study of droplet infection.* Cambridge: Harvard University Press.

White, H. J. (1963). *Industrial electrostatic precipitation.* Reading, MA: Addison Wesley.

Willeke, K., S.A. Grinshpun, J. Donnelly, A. Juozaitis, M. Thompson, C.W. Chang, F. Liebhaber & A. Nevalainen. (1993). Physical and biological sampling efficiencies of bioaerosol samplers. .*Indoor Air Quality and Climate, 4*, 131–136.

Wu C.C., G.W.M. Lee, P. Cheng, S. Yang, K.P. Yu. (2006). Effect of wall surface materials on deposition of particles with the aid of negative air ions. *Journal of Aerosol Science, 37*(5), 616-630. doi:doi.org/10.1016/j.jaerosci.2005.05.018

Wu J., P. Traoré & C. Louste. (2013). An efficient finite volume method for electric fieldespace charge coupled problems. *Journal of Electrostatics, 71*(3), 319-325. doi:10.1016/j.elstat.2012.12.004

Yamashita Y., K. Shinozaki and E. Nakamae. (1988). A boundary-finite element method to compute directly electric field intensity with high accuracy. *IEEE Transactions on Power Delivery, 3*(4), 1754 - 1760. doi:10.1109/61.193981

Yoo, J. (2018). Review of disinfection and sterilization – Back to the basics. *Journal of Infection and Chemotherapy, 50*(2), 101 -109. doi:doi.org/10.3947/ic.2018.50.2.101

Zamora, I.R., A. Tabazadeh, D.M. Golden & M.Z. Jacobson. (2011). Hygroscopic Growth of Common Organic Aerosol Solutes, including Humic Substances, as derived from Water Activity Measurements. *Journal of Geophysical Research, 116*, 1-12. doi:10.1029/2011JD016067

Zhang N., Z. Liu, Q. Han, J. Qiu, J. Chen, G. Zhang, Z. Li, S. Lou &N. Li. (2011). Development of one-step SYBR Green real-time RT-PCR for quantifying bovine viral diarrhea virus type-1 and its comparison with conventional RT-PCR. *Virology Journal, 8*, 1-8. doi: 10.1186/1743-422X-8-374

Zhao L., & K. Adamiak. (2008). Numerical simulation of the electrohydrodynamic flow in a single wire-plate electrostatic precipitator. *IEEE Transactions on Industry Applications, 44*(3), 683-691.

Zhao, L. & K. Adamiak. (2011). Numerical simulation of the effect of EHD flow on corona discharge in compressed air. (pp. 290-304). Orlando: IEEE Industry Applications Society Annual Meetings. doi:10.1109/IAS.2011.6074283

Zhao, Y., A. J. A. Aarnink , W. Wang , T. Fabri, P. W .G. Groot Koerkamp, M. C. M. de Jong. (2014). Airborne virus sampling: Efficiencies of samplers and their detection limits for

infectious bursal disease virus (IBDV). *Annals of Agricultural and Environmental Medicine, 21*(3), 464-471. doi: 10.5604/12321966.1120585

Zhao, Y., A.J.A. Aarnink, R. Dijkman, T. Fabri, M.C.M De Joong, P.W.G.G Koerkamp. (2012). Effects of Temperature, Relative Humidity, Absolute Humidity and Evaporation Potential on Survival of Airborne Gumboro Vaccine Virus. *Applied and Environmental Microbiology*, 1048-1054.

Zhu S., J. Srebric, J.D. Spengler & P. Demokritou. (2012). An advanced numerical model for the assessment of airborne transmission of influenza in bus microenvironments. *Building and Environment, 47*, 67-75. doi:10.1016/j.buildenv.2011.05.003

6.1 Appendix A: ANSYS FLUENT UDF codes for simulating air ionization in a chamber

```
#include "udf.h"
#define C_I 240 /* mean thermal speed of the ions*/
#define K_EE 9e9/*electric field conversion factor*/
#define R_PERM 2.1 /* relative permittivity of virus bioaerosol*/
#define E_E 1.602177e-19 /* charge on an electron*/
#define EPS_0 8.85e-12/* permittivity of space*/
#define M_ION 1.5e-4 /* Ion mobility */
#define K 1.38E-23 /* Boltzmann constant */
static int flag=0;
DEFINE_INIT(bioaerosol_init,domain)
{
/* Set memory for bioaerosols*/
if (NULLP(user_bioaerosol_vars)) Init_User_Particle_Vars();
/* now set the name and label */
strcpy(user_particle_vars[0].name,"charge");
strcpy(user_particle_vars[0].label," charge acquired");
strcpy(user_particle_vars[1].name,"ElectroF");
strcpy(user_particle_vars[1].label," Electrostatic force on bioaerosol");
strcpy(user_particle_vars[2].name,"Bioaerosol-speed");
strcpy(user_particle_vars[2].label,"Bioaerosol speed");
}
/* Inject bioaerosol velocity and temperature same at the point of injection * (Not applicable to file injection)*/
DEFINE_DPM_INJECTION_INIT(Init_V_T,I)
```

```
{
Particle *p;
cell_t cell;
Thread *cthread;
loop(p,I->p) /*  Macro to get bioaerosol injected into the  gas phase */
{
cell = P_CELL(p); /* Macro for getting the thread and cell that the bioaerosol
is currently in */
cthread = P_CELL_THREAD(p);
P_T(p)=C_T(cell,cthread); /* temperature  macro*/
P_VEL(p)[0]=C_U(cell,cthread); /* x velocity macro */
P_VEL(p)[1]=C_V(cell,cthread); /* y velocity macro */
P_VEL(p)[2]=C_W(cell,cthread); /* z velocity macro */
}
}
DEFINE_DPM_SOURCE(q_source,c,t,S,strength,p)
{
real charge,d_charge,delta_qp;
real t_res, qp;
real v_cell_x,v_cell_y,v_cell_z,dx,dy,dz;
real mfr,nfr;
delta_qp=P_USER_REAL(p,0);
t_res=P_TIME(p)-P_TIME0(p); /* macro to get the time bioaerosol has spent in a cell */
dx=P_VEL(p)[0]*t_res;
```

```
dy=P_VEL(p)[1]*t_res;
dz=P_VEL(p)[2]*t_res;
nfr=strength*t_res;
d_charge=delta_qp*nfr*(t_res/P_DT(p));
mfr=P_MASS(p)*nfr;
v_cell_x=P_MASS(p)*strength*dx;
v_cell_y=P_MASS(p)*strength*dy;
v_cell_z=P_MASS(p)*strength*dz;
C_UDMI(c,t,20) += nfr;
C_UDMI(c,t,21) += mfr;
C_UDMI(c,t,22)+= v_cell_x;
C_UDMI(c,t,23)+= v_cell_y;
C_UDMI(c,t,24)+= v_cell_z;
C_UDMI(c,t,25)+= d_charge;
flag=1; /* set flag to 1 */
}
DEFINE_ADJUST(dens_particle,d)
{
Thread *t;
cell_t c;
face_t f;
Thread *t0;
cell_t c0;
real dr0[ND_ND],dr1[ND_ND], xf[ND_ND], dy;
```

```
if (!Data_Valid_P()) return;
thread_loop_c(t,d)
{
begin_c_loop(c,t)
{
if (flag==1)
{
C_UDMI(c,t,26) = C_UDMI(c,t,25)/(C_VOLUME(c,t)); /* diffusion charge-rho-particle */
C_UDMI(c,t,27) = C_UDMI(c,t,20)/(C_VOLUME(c,t));/* number conc */
C_UDMI(c,t,28) = C_UDMI(c,t,21)/(C_VOLUME(c,t));/* mass-conc */
}
}
end_c_loop(c,t)
}
}
```

/*UDF to calculate the electrostatic force which acts on a bioaerosol*/

```
DEFINE_DPM_BODY_FORCE(body_force,p,i)
{
real bforce, Ex, Ey,Ez, n_charge;
Thread *t;
cell_t c;
/* get current cell and thread pointer */
c = P_CELL(p);
t = P_CELL_THREAD(p);
```

```
/* get particle charge */
n_charge = (C_UDMI(c,t,13)*E_E);
/* calculate body force */
bforce = C_UDMI(c,t,3)*n_charge;
C_UDMI(c,t,14)=bforce;
C_UDMI(c,t,15)=bforce/P_MASS(p);
/* an acceleration should be returned */
return(bforce/P_MASS(p));
}
```

/*UDF for estimating the convective component of the UDS for ion transport*/

```
DEFINE_UDS_FLUX(my_uds_flux,f,t,i)
{
  cell_t  c0,  c1 = -1;
  Thread *t0, *t1 = NULL;

  real NV_VEC(psi_vec), NV_VEC(A), flux = 0.0;

  c0 = F_C0(f,t);
  t0 = F_C0_THREAD(f,t);
  F_AREA(A, f, t);

  /* If face lies at domain boundary, use face values; */
  /* If face lies IN the domain, use average of adjacent cells. */
```

```
        if (BOUNDARY_FACE_THREAD_P(t)) /*Most face values will be available*/
          {
            real dens;
            /* Depending on its BC, density may not be set on face thread*/
            if (NNULLP(THREAD_STORAGE(t,SV_DENSITY)))
              dens = F_R(f,t);   /* Set dens to face value if available */
            else
              dens = C_R(c0,t0); /* else, set dens to cell value */

            NV_DS(psi_vec,  =, F_U(f,t), F_V(f,t), F_W(f,t), *, dens);

            flux = NV_DOT(psi_vec, A)/dens; /* flux through Face */
          }
        else
          {
            c1 = F_C1(f,t);       /* Get cell on other side of face */
            t1 = F_C1_THREAD(f,t);

            NV_DS(psi_vec,  =, C_U(c0,t0),C_V(c0,t0),C_W(c0,t0),*,C_R(c0,t0));
            NV_DS(psi_vec, +=, C_U(c1,t1),C_V(c1,t1),C_W(c1,t1),*,C_R(c1,t1));

            flux = (NV_DOT(psi_vec, A)/2)/((C_R(c0,t0)+C_R(c1,t1))/2); /* Average flux through
face */
          }
        /* Fluent will multiply the returned value by phi_f (the scalar's
```

```
    value at the face) to get the "complete" advective term.  */
 return flux;
}
/* UDF for estimating the source terms for uds-0 */
DEFINE_SOURCE(pot_source,c,t,dS,eqn)
{
real pot_source, S_1, S_2;
dS[eqn] = 0.0;
S_1 = (C_UDSI(c,t,1)*E_E);
 pot_source = S_1/EPS_0;
C_UDMI(c,t,16) = pot_source;
return pot_source;
}
/*UDF for estimating momentum source terms for the gas phase*/

DEFINE_SOURCE(x_mom_source,c,t,dS,eqn)
{
real x_m_source;
dS[eqn] = 0.0;
/* Do nothing if data not valid yet. */
if (Data_Valid_P())
{
x_m_source = ((C_UDSI(c,t,1)*E_E)/(C_VOLUME(c,t)))*C_UDMI(c,t,0);
C_UDMI(c,t,17) = x_m_source; /* store to memory 8 */
```

```
return x_m_source;
}
else
{
x_m_source = 0.0;
return x_m_source;
}
}
DEFINE_SOURCE(y_mom_source,c,t,dS,eqn)
{
real y_m_source;
dS[eqn] = 0.0;
/* Do nothing if data not valid yet. */
if (Data_Valid_P())
{
y_m_source = ((C_UDSI(c,t,1)*E_E)/(C_VOLUME(c,t)))*C_UDMI(c,t,1);
C_UDMI(c,t,18) = y_m_source; /* store to memory 9 */
return y_m_source;
}
else
{
y_m_source = 0.0;
return y_m_source;
}
```

```
}
DEFINE_SOURCE(z_mom_source,c,t,dS,eqn)
{
real z_m_source;
dS[eqn] = 0.0;
/* Do nothing if data not valid yet. */
if (Data_Valid_P())
{
z_m_source = ((C_UDSI(c,t,1)*E_E)/(C_VOLUME(c,t)))*C_UDMI(c,t,2);
C_UDMI(c,t,19) = z_m_source; /* store to memory 28*/
return z_m_source;
}
else
{
z_m_source = 0.0;
return z_m_source;
}
}
DEFINE_ADJUST(ION_particle,d)
{
Thread *t;
cell_t c;
face_t f;
Thread *t0;
```

```
cell_t c0;
real dr0[ND_ND],dr1[ND_ND], xf[ND_ND], dx,dy, dz, dw;
if (!Data_Valid_P()) return;
thread_loop_c(t,d)
{
begin_c_loop(c,t)
{
if (flag==1)
{
dx = ((C_UDSI(c,t,1)*E_E)/(C_VOLUME(c,t)))*M_ION*abs(C_UDMI(c,t,0));
C_UDMI(c,t,29) =dx;
dy = ((C_UDSI(c,t,1)*E_E)/(C_VOLUME(c,t)))*M_ION*abs(C_UDMI(c,t,1));
C_UDMI(c,t,30) = dy;
dz = ((C_UDSI(c,t,1)*E_E)/(C_VOLUME(c,t)))*M_ION*abs(C_UDMI(c,t,2));
C_UDMI(c,t,31) =dz;
dw = ((C_UDSI(c,t,1)*E_E)/(C_VOLUME(c,t)));
C_UDMI(c,t,31) = dw;
}
}
end_c_loop(c,t)
}
}
/* Macros to estimate electric field components and magnitude*/
/*Macros that estimates User defined scalars (UDS)*/
```

```
/*Macros that initializes the UDMs*/
DEFINE_ADJUST(EstE_xyz,d) */
{
Thread *t;
cell_t c;
face_t f;
Thread *t0;
cell_t c0;
real dr0[ND_ND],dr1[ND_ND], xf[ND_ND], dy;
if (!Data_Valid_P()) return;
thread_loop_c(t,d)
{
if (NULL != THREAD_STORAGE(t,SV_UDS_I(0)) &&
NULL != T_STORAGE_R_NV(t,SV_UDSI_G(0)))
{
begin_c_loop(c,t)
{
C_UDMI(c,t,0) = -1.*C_UDSI_G(c,t,0)[0];
C_UDMI(c,t,1) = -1.*C_UDSI_G(c,t,0)[1];
C_UDMI(c,t,2) = -1.*C_UDSI_G(c,t,0)[2];
C_UDMI(c,t,3) = NV_MAG(C_UDSI_G(c,t,0));
}
end_c_loop(c,t)
}
```

```
}
thread_loop_f(t,d)
{
if (NULL != THREAD_STORAGE(t,SV_UDS_I(0)) &&
NULL != T_STORAGE_R_NV(t->t0,SV_UDSI_G(0)))
{
if (BOUNDARY_FACE_THREAD_P(t)) /*Determine  electric field values at face boundaries only */
{
begin_f_loop(f,t)
{
c0 = F_C0(f,t);
t0 = THREAD_T0(t);
F_CENTROID(xf,f,t);
C_CENTROID(dr0,c0,t0);
NV_VV(dr1,=,xf,-,dr0);
F_UDMI(f,t,0) = C_UDMI(c,t0,0) + (C_UDSI_G(c0,t0,0)[0]*dr1[0]);
F_UDMI(f,t,1) = C_UDMI(c,t0,1) + (C_UDSI_G(c0,t0,0)[1]*dr1[1]);
F_UDMI(f,t,2) = C_UDMI(c,t0,2) + (C_UDSI_G(c0,t0,0)[2]*dr1[2]);
}
end_f_loop(f,t)
}
}
}
}
```

```
/*Macros to estimate the number of ions attached to a bioaerosol*/
DEFINE_DPM_SCALAR_UPDATE (bioaerosol_charge,c,t,initialize,p)
{
real  diam, rho_ion, n_ion;
real n_p, n_t,t_t,v_t,e_m,t_m,z_t, n_charge, n_pions;
n_ion = C_UDSI(c,t,1);
C_UDMI(c,t,4) = C_UDSI(c,t,1);
diam = P_DIAM(p);
C_UDMI(c,t,5) = diam;
t_m= CURRENT_TIME;
C_UDMI(c,t,6) = t_m;
e_m=pow(E_E, 2) ;
C_UDMI(c,t,7)=e_m;
n_p=diam*K*P_T(p)/(2*pow(E_E, 2)*K_EE);
C_UDMI(c,t,8) = n_p;
n_t=(M_PI*K_EE*diam*C_I*pow(E_E, 2)*(C_UDMI(c,t,4)*CURRENT_TIME);
C_UDMI(c,t,9) = n_t;
t_t=(2*K*P_T(p));
C_UDMI(c,t,10) = t_t;
v_t = (n_t)/(t_t);
C_UDMI(c,t,11) = v_t;
z_t=(1+v_t);
C_UDMI(c,t,12) = z_t;
n_pions =n_p*log(z_t);
```

```
C_UDMI(c,t,13) = n_pions;
}

/*UDF to convert Eulerian values to Lagrangian*/
```

6.2 Appendix B: ANOVA for measurement location

A one-way ANOVA analysis for the effect of measurement location on bioaerosol concentration in the chamber with injection of bioaerosols and circulation fans at different sampling times

Sampling time: 10 seconds

Source of Variation	*SS*	*df*	*MS*	*F*	*P-value*	*F crit*
Between Groups	34823.6	4	8705.9	47.2291	1.8E-06	3.47805
Within Groups	1843.33	10	184.333			
Total	36666.9	14				

20 seconds

Source of Variation	*SS*	*df*	*MS*	*F*	*P-value*	*F crit*
Between Groups	41295.6	4	10323.9	20.1272	9E-05	3.47805
Within Groups	5129.33	10	512.933			
Total	46424.9	14				

30 seconds

Source of Variation	*SS*	*df*	*MS*	*F*	*P-value*	*F crit*
Between Groups	95.6	4	23.9	2.18598	0.14403	3.47805
Within Groups	109.333	10	10.9333			
Total	204.933	14				

40 seconds

Source of Variation	*SS*	*df*	*MS*	*F*	*P-value*	*F crit*
Between Groups	15.7333	4	3.93333	0.78667	0.55938	3.47805
Within Groups	50	10	5			
Total	65.7333	14				

50 seconds

Source of Variation	*SS*	*df*	*MS*	*F*	*P-value*	*F crit*
Between Groups	46.2667	4	11.5667	1.94944	0.17867	3.47805
Within Groups	59.3333	10	5.93333			
Total	105.6	14				

60 seconds

Source of Variation	*SS*	*df*	*MS*	*F*	*P-value*	*F crit*
Between Groups	26.9333	4	6.73333	1.68333	0.22958	3.47805
Within Groups	40	10	4			
Total	66.9333	14				

70 seconds

Source of Variation	*SS*	*df*	*MS*	*F*	*P-value*	*F crit*
Between Groups	13.8667	4	3.46667	1.4717	0.25998	3.05557
Within Groups	35.3333	15	2.35556			
Total	49.2	19				

80 seconds

Source of Variation	*SS*	*df*	*MS*	*F*	*P-value*	*F crit*
Between Groups	25.0667	4	6.26667	2.18605	0.14403	3.47805
Within Groups	28.6667	10	2.86667			
Total	53.7333	14				

90 seconds

Source of Variation	SS	df	MS	F	P-value	F crit
Between Groups	8.9333333	4	2.23333	1.59524	0.24991	3.47805
Within Groups	14	10	1.4			
Total	22.933333	14				

100 seconds

Source of Variation	*SS*	*df*	*MS*	*F*	*P-value*	*F crit*
Between Groups	6.4	4	1.6	0.75	0.58009	3.47805
Within Groups	21.333333	10	2.13333			
Total	27.733333	14				

110 seconds

Source of Variation	*SS*	*df*	*MS*	*F*	*P-value*	*F crit*
Between Groups	5.6	4	1.4	1.23529	0.35637	3.47805
Within Groups	11.3333	10	1.13333			
Total	16.9333	14				

120 seconds

Source of Variation	*SS*	*df*	*MS*	*F*	*P-value*	*F crit*
Between Groups	5.6	4	1.4	1.23529	0.35637	3.47805
Within Groups	11.3333	10	1.13333			
Total	16.9333	14				

130 seconds

Source of Variation	*SS*	*df*	*MS*	*F*	*P-value*	*F crit*
Between Groups	8.4	4	2.1	0.95455	0.47273	3.47805
Within Groups	22	10	2.2			
Total	30.4	14				

140 seconds

Source of Variation	*SS*	*df*	*MS*	*F*	*P-value*	*F crit*
Between Groups	4	4	1	0.625	0.65536	3.47805
Within Groups	16	10	1.6			
Total	20	14				

170 seconds

Source of Variation	*SS*	*df*	*MS*	*F*	*P-value*	*F crit*
Between Groups	3.33333	4	0.83333	1.78571	0.20826	3.47805
Within Groups	4.66667	10	0.46667			
Total	8	14				

6.3 Appendix C: Paired T-test for plaque assay tests

(Stock C - Natural Decay)

Bioaerosol concentration of 812 #/cm^3

	Natural	*Theoretical*
Mean	1.77E+06	2.20E+06
Variance	2.03E+11	0.00E+00
Observations	3.00E+00	3.00E+00
Pearson Correlation	#DIV/0!	
Hypothesized Mean Difference	0.00E+00	
df	2.00E+00	
t Stat	-1.66E+00	
P(T<=t) one-tail	1.19E-01	
t Critical one-tail	2.92E+00	
P(T<=t) two-tail	2.38E-01	
t Critical two-tail	4.30E+00	

Bioaerosol concentration of 631 #/cm^3

	Natural	*Theoretical*
Mean	1.43E+06	1.70E+06
Variance	6.33E+10	0.00E+00
Observations	3.00E+00	3.00E+00
Pearson Correlation	#DIV/0!	
Hypothesized Mean Difference	0.00E+00	
df	2.00E+00	
t Stat	-1.84E+00	
P(T<=t) one-tail	1.04E-01	
t Critical one-tail	2.92E+00	
P(T<=t) two-tail	2.08E-01	
t Critical two-tail	4.30E+00	

Bioaerosol concentration of 90 #/cm^3

	Natural	*Theoretical*
Mean	1.93E+05	2.40E+05
Variance	4.23E+09	0.00E+00
Observations	3.00E+00	3.00E+00
Pearson Correlation	#DIV/0!	
Hypothesized Mean Difference	0.00E+00	
df	2.00E+00	
	-	
t Stat	1.24E+00	
P(T<=t) one-tail	1.70E-01	
t Critical one-tail	2.92E+00	
P(T<=t) two-tail	3.40E-01	
t Critical two-tail	4.30E+00	

Bioaerosol concentration of 9 #/cm^3

	Natural	*Theoretical*
Mean	2.00E+04	2.40E+04
Variance	2.70E+07	0.00E+00
Observations	3.00E+00	3.00E+00
Pearson Correlation	#DIV/0!	
Hypothesized Mean Difference	0.00E+00	
df	2.00E+00	
	-	
t Stat	1.33E+00	
P(T<=t) one-tail	1.57E-01	
t Critical one-tail	2.92E+00	
P(T<=t) two-tail	3.14E-01	
t Critical two-tail	4.30E+00	

Stock solution C at ion concentration of 2.4×10^{13} ions/m^3

Bioaerosol concentration of 812 #/cm^3

	Natural Decay	*Ionization*
Mean	1.77E+06	1.40E+06
Variance	2.03E+11	7.00E+10
Observations	3.00E+00	3.00E+00
Pearson Correlation	-1.26E-01	
Hypothesized Mean Difference	0.00E+00	
df	2.00E+00	
t Stat	1.15E+00	
P(T<=t) one-tail	1.84E-01	
t Critical one-tail	2.92E+00	
P(T<=t) two-tail	3.68E-01	
t Critical two-tail	4.30E+00	

Bioaerosol concentration of 631 #/cm^3

	Natural Decay	*Ionization*
Mean	1.43E+06	5.73E+05
Variance	6.33E+10	4.33E+08
Observations	3.00E+00	3.00E+00
Pearson Correlation	9.23E-01	
Hypothesized Mean Difference	0.00E+00	
df	2.00E+00	
t Stat	6.40E+00	
P(T<=t) one-tail	1.18E-02	
t Critical one-tail	2.92E+00	
P(T<=t) two-tail	2.35E-02	
t Critical two-tail	4.30E+00	

Bioaerosol concentration of 451 #/cm^3

	Natural Decay	*Ionization*
Mean	1.02E+06	7.23E+03
Variance	4.63E+09	2.33E+04
Observations	3.00E+00	3.00E+00
Pearson Correlation	3.21E-02	
Hypothesized Mean Difference	0.00E+00	
df	2.00E+00	
t Stat	2.59E+01	
P(T<=t) one-tail	7.46E-04	
t Critical one-tail	2.92E+00	
P(T<=t) two-tail	1.49E-03	
t Critical two-tail	4.30E+00	

Bioaerosol concentration of 90 #/cm^3

	Natural Decay	*Ionization*
Mean	1.93E+05	8.50E+01
Variance	4.23E+09	4.00E+00
Observations	3.00E+00	3.00E+00
Pearson Correlation	9.99E-01	
Hypothesized Mean Difference	0.00E+00	
df	2.00E+00	
t Stat	5.14E+00	
P(T<=t) one-tail	1.79E-02	
t Critical one-tail	2.92E+00	
P(T<=t) two-tail	3.58E-02	
t Critical two-tail	4.30E+00	

Bioaerosol concentration of 9 #/cm^3

	Natural Decay	*Ionization*
Mean	2.00E+04	9.57E+01
Variance	2.70E+07	1.33E+00
Observations	3.00E+00	3.00E+00
Pearson Correlation	-5.00E-01	
Hypothesized Mean Difference	0.00E+00	
df	2.00E+00	
t Stat	6.63E+00	
P(T<=t) one-tail	1.10E-02	
t Critical one-tail	2.92E+00	
P(T<=t) two-tail	2.20E-02	
t Critical two-tail	4.30E+00	

Stock solution B -Natural Decay

Bioaerosol concentration of 812 #/cm^3

	Natural Decay	*Theoretical*
Mean	1.87E+05	2.20E+05
Variance	1.03E+09	0.00E+00
Observations	3.00E+00	3.00E+00
Pearson Correlation	#DIV/0!	
Hypothesized Mean Difference	0.00E+00	
df	2.00E+00	
	-	
t Stat	1.80E+00	
P(T<=t) one-tail	1.07E-01	
t Critical one-tail	2.92E+00	
P(T<=t) two-tail	2.14E-01	
t Critical two-tail	4.30E+00	

Bioaerosol concentration of 631 #/cm^3

	Natural Decay	*Theoretical*
Mean	1.43E+05	1.70E+05
Variance	4.33E+08	0.00E+00
Observations	3.00E+00	3.00E+00
Pearson Correlation	#DIV/0!	
Hypothesized Mean Difference	0.00E+00	
df	2.00E+00	
	-	
t Stat	2.22E+00	
P(T<=t) one-tail	7.84E-02	
t Critical one-tail	2.92E+00	
P(T<=t) two-tail	1.57E-01	
t Critical two-tail	4.30E+00	

Bioaerosol concentration of 451 #/cm^3

	Natural Decay	*Theoretical*
Mean	1.06E+05	1.20E+05
Variance	1.40E+08	0.00E+00
Observations	3.00E+00	3.00E+00
Pearson Correlation	#DIV/0!	
Hypothesized Mean Difference	0.00E+00	
df	2.00E+00	
	-	
t Stat	2.00E+00	
P(T<=t) one-tail	9.19E-02	
t Critical one-tail	2.92E+00	
P(T<=t) two-tail	1.84E-01	
t Critical two-tail	4.30E+00	

Bioaerosol concentration of 90 #/cm^3

	Natural Decay	*Theoretical*
Mean	2.03E+04	2.40E+04
Variance	5.33E+06	0.00E+00
Observations	3.00E+00	3.00E+00
Pearson Correlation	#DIV/0!	
Hypothesized Mean Difference	0.00E+00	
df	2.00E+00	
	-	
t Stat	2.75E+00	
P(T<=t) one-tail	5.54E-02	
t Critical one-tail	2.92E+00	
P(T<=t) two-tail	1.11E-01	
t Critical two-tail	4.30E+00	

Stock solution B at ion concentration of 2.4×10^{13} ions/m^3

Bioaerosol concentration of 812 #/cm^3

	Natural Decay	*Ionization*
Mean	1.87E+05	1.43E+05
Variance	1.23E+09	2.33E+08
Observations	3.00E+00	3.00E+00
Pearson Correlation	5.90E-01	
Hypothesized Mean Difference	0.00E+00	
df	2.00E+00	
t Stat	2.60E+00	
P(T<=t) one-tail	6.08E-02	
t Critical one-tail	2.92E+00	
P(T<=t) two-tail	1.22E-01	
t Critical two-tail	4.30E+00	

Bioaerosol concentration of 613 #/cm^3

	Natural Decay	*Ionization*
Mean	1.40E+05	5.17E+04
Variance	4.00E+08	4.33E+06
Observations	3.00E+00	3.00E+00
Pearson Correlation	9.61E-01	
Hypothesized Mean Difference	0.00E+00	
df	2.00E+00	
t Stat	8.50E+00	
P(T<=t) one-tail	6.79E-03	
t Critical one-tail	2.92E+00	
P(T<=t) two-tail	1.36E-02	
t Critical two-tail	4.30E+00	

Bioaerosol concentration of 451 #/cm^3

	Natural Decay	*Ionization*
Mean	1.06E+05	8.40E+03
Variance	1.40E+08	4.00E+04
Observations	3.00E+00	3.00E+00
Pearson Correlation	8.44E-01	
Hypothesized Mean Difference	0.00E+00	
df	2.00E+00	
t Stat	1.45E+01	
P(T<=t) one-tail	2.35E-03	
t Critical one-tail	2.92E+00	
P(T<=t) two-tail	4.71E-03	
t Critical two-tail	4.30E+00	

Bioaerosol concentration of 90 #/cm^3

	Natural Decay	*Ionization*
Mean	2.03E+04	9.57E+03
Variance	2.33E+06	1.23E+05
Observations	3.00E+00	3.00E+00
Pearson Correlation	-7.15E-01	
Hypothesized Mean Difference	0.00E+00	
df	2.00E+00	
t Stat	1.04E+01	
P(T<=t) one-tail	4.57E-03	
t Critical one-tail	2.92E+00	
P(T<=t) two-tail	9.14E-03	
t Critical two-tail	4.30E+00	

Bioaerosol concentration of 9 #/cm^3

	Natural Decay	*Ionization*
Mean	2.03E+03	1.23E+01
Variance	2.33E+04	1.33E+00
Observations	3.00E+00	3.00E+00
Pearson Correlation	-9.45E-01	
Hypothesized Mean Difference	0.00E+00	
df	2.00E+00	
t Stat	2.28E+01	
P(T<=t) one-tail	9.63E-04	
t Critical one-tail	2.92E+00	
P(T<=t) two-tail	1.93E-03	
t Critical two-tail	4.30E+00	

Stock solution A - Natural Decay

Bioaerosol concentration of 831 #/cm^3

	Natural	*Theoretical*
Mean	1.93E+04	2.20E+04
Variance	6.33E+06	0.00E+00
Observations	3.00E+00	3.00E+00
Pearson Correlation	#DIV/0!	
Hypothesized Mean Difference	0.00E+00	
df	2.00E+00	
t Stat	-1.84E+00	
P(T<=t) one-tail	1.04E-01	
t Critical one-tail	2.92E+00	
P(T<=t) two-tail	2.08E-01	
t Critical two-tail	4.30E+00	

Bioaerosol concentration of 631 #/cm^3

	Natural	*Theoretical*
Mean	1.43E+04	1.70E+04
Variance	6.33E+06	0.00E+00
Observations	3.00E+00	3.00E+00
Pearson Correlation	#DIV/0!	
Hypothesized Mean Difference	0.00E+00	
df	2.00E+00	
t Stat	-1.84E+00	
P(T<=t) one-tail	1.04E-01	
t Critical one-tail	2.92E+00	
P(T<=t) two-tail	2.08E-01	
t Critical two-tail	4.30E+00	

Bioaerosol concentration of 451 #/cm^3

	Natural	*Theoretical*
Mean	1.09E+04	1.20E+04
Variance	1.21E+06	0.00E+00
Observations	3.00E+00	3.00E+00
Pearson Correlation	#DIV/0!	
Hypothesized Mean Difference	0.00E+00	
df	2.00E+00	
t Stat	-1.68E+00	
P(T<=t) one-tail	1.18E-01	
t Critical one-tail	2.92E+00	
P(T<=t) two-tail	2.35E-01	
t Critical two-tail	4.30E+00	

Bioaerosol concentration of 90 #/cm^3

	Natural	*Theoretical*
Mean	2.13E+03	2.40E+03
Variance	5.33E+04	0.00E+00
Observations	3.00E+00	3.00E+00
Pearson Correlation	#DIV/0!	
Hypothesized Mean Difference	0.00E+00	
df	2.00E+00	
t Stat	-2.00E+00	
P(T<=t) one-tail	9.18E-02	
t Critical one-tail	2.92E+00	
P(T<=t) two-tail	1.84E-01	
t Critical two-tail	4.30E+00	

Bioaerosol concentration of 9 #/cm^3

	Natural	*Theoretical*
Mean	1.93E+02	2.40E+02
Variance	1.73E+03	0.00E+00
Observations	3.00E+00	3.00E+00
Pearson Correlation	#DIV/0!	
Hypothesized Mean Difference	0.00E+00	
df	2.00E+00	
t Stat	-1.94E+00	
P(T<=t) one-tail	9.59E-02	
t Critical one-tail	2.92E+00	
P(T<=t) two-tail	1.92E-01	
t Critical two-tail	4.30E+00	

Stock solution A at ion concentration of 2.4×10^{13} ions/m^3

Bioaerosol concentration of 812 #/cm^3

	Natural Decay	*Ionization*
Mean	1.93E+04	1.53E+04
Variance	6.33E+06	1.33E+06
Observations	3.00E+00	3.00E+00
Pearson Correlation	-9.18E-01	
Hypothesized Mean Difference	0.00E+00	
df	2.00E+00	
t Stat	1.92E+00	
P(T<=t) one-tail	9.73E-02	
t Critical one-tail	2.92E+00	
P(T<=t) two-tail	1.95E-01	
t Critical two-tail	4.30E+00	

Bioaerosol concentration of 631 #/cm^3

	Natural Decay	*Ionization*
Mean	1.43E+04	5.00E+03
Variance	6.33E+06	1.00E+06
Observations	3.00E+00	3.00E+00
Pearson Correlation	5.96E-01	
Hypothesized Mean Difference	0.00E+00	
df	2.00E+00	
t Stat	8.60E+00	
P(T<=t) one-tail	6.63E-03	
t Critical one-tail	2.92E+00	
P(T<=t) two-tail	1.33E-02	
t Critical two-tail	4.30E+00	

Bioaerosol concentration of 451 #/cm^3

	Natural Decay	*Ionization*
Mean	1.09E+04	7.20E+02
Variance	1.21E+06	4.00E+02
Observations	3.00E+00	3.00E+00
Pearson Correlation	4.54E-01	
Hypothesized Mean Difference	0.00E+00	
df	2.00E+00	
t Stat	1.62E+01	
P(T<=t) one-tail	1.90E-03	
t Critical one-tail	2.92E+00	
P(T<=t) two-tail	3.79E-03	
t Critical two-tail	4.30E+00	

Bioaerosol concentration of 90 #/cm^3

	2.40E+03	*8.50E+01*
Mean	2.10E+03	8.50E+01
Variance	0.00E+00	8.00E+00
Observations	2.00E+00	2.00E+00
Pearson Correlation	#DIV/0!	
Hypothesized Mean Difference	0.00E+00	
df	1.00E+00	
t Stat	9.58E+02	
P(T<=t) one-tail	3.32E-04	
t Critical one-tail	6.31E+00	
P(T<=t) two-tail	6.65E-04	
t Critical two-tail	1.27E+01	

Bioaerosol concentration of 9 #/cm^3

	Natural Decay	*Ionization*
Mean	1.93E+02	1.07E+01
Variance	1.73E+03	1.33E+00
Observations	3.00E+00	3.00E+00
Pearson Correlation	-6.93E-01	
Hypothesized Mean Difference	0.00E+00	
df	2.00E+00	
t Stat	7.45E+00	
P(T<=t) one-tail	8.76E-03	
t Critical one-tail	2.92E+00	
P(T<=t) two-tail	1.75E-02	
t Critical two-tail	4.30E+00	

Stock A and ion concentration of 3×10^{10} ions/m^3

Bioaerosol concentration of 831 #/cm^3

	Natural	*Ionization*
Mean	1.93E+04	1.67E+04
Variance	6.33E+06	3.33E+05
Observations	3.00E+00	3.00E+00
Pearson Correlation	1.15E-01	
Hypothesized Mean Difference	0.00E+00	
df	2.00E+00	
t Stat	1.84E+00	
P(T<=t) one-tail	1.04E-01	
t Critical one-tail	2.92E+00	
P(T<=t) two-tail	2.08E-01	
t Critical two-tail	4.30E+00	

Bioaerosol concentration of 631 #/cm^3

	Natural	*Ionization*
Mean	1.43E+04	1.17E+04
Variance	6.33E+06	3.33E+05
Observations	3.00E+00	3.00E+00
Pearson Correlation	1.15E-01	
Hypothesized Mean Difference	0.00E+00	
df	2.00E+00	
t Stat	1.84E+00	
P(T<=t) one-tail	1.04E-01	
t Critical one-tail	2.92E+00	
P(T<=t) two-tail	2.08E-01	
t Critical two-tail	4.30E+00	

Bioaerosol concentration of 451 #/cm^3

	Natural	*Ionization*
Mean	1.09E+04	9.67E+03
Variance	1.21E+06	1.03E+05
Observations	3.00E+00	3.00E+00
Pearson Correlation	-2.07E-01	
Hypothesized Mean Difference	0.00E+00	
df	2.00E+00	
t Stat	1.81E+00	
P(T<=t) one-tail	1.06E-01	
t Critical one-tail	2.92E+00	
P(T<=t) two-tail	2.11E-01	
t Critical two-tail	4.30E+00	

Bioaerosol concentration of 90 #/cm^3

	Natural	*Ionization*
Mean	2.13E+03	1.90E+03
Variance	5.33E+04	0.00E+00
Observations	3.00E+00	3.00E+00
Pearson Correlation	#DIV/0!	
Hypothesized Mean Difference	0.00E+00	
df	2.00E+00	
t Stat	1.75E+00	
P(T<=t) one-tail	1.11E-01	
t Critical one-tail	2.92E+00	
P(T<=t) two-tail	2.22E-01	
t Critical two-tail	4.30E+00	

Bioaerosol concentration of 9 #/cm^3

	Natural	*Ionization*
Mean	1.93E+02	1.05E+02
Variance	1.73E+03	6.98E+03
Observations	3.00E+00	3.00E+00
Pearson Correlation	6.04E-01	
Hypothesized Mean Difference	0.00E+00	
df	2.00E+00	
t Stat	2.28E+00	
P(T<=t) one-tail	7.52E-02	
t Critical one-tail	2.92E+00	
P(T<=t) two-tail	1.50E-01	
t Critical two-tail	4.30E+00	

Stock C and ion concentration of 3×10^{10} ions/m^3

Bioaerosol concentration of 812 #/cm^3

	Natural	*Ionization*
Mean	1.77E+06	1.53E+06
Variance	2.03E+11	9.33E+10
Observations	3.00E+00	3.00E+00
Pearson Correlation	9.92E-01	
Hypothesized Mean Difference	0.00E+00	
df	2.00E+00	
t Stat	2.65E+00	
P(T<=t) one-tail	5.90E-02	
t Critical one-tail	2.92E+00	
P(T<=t) two-tail	1.18E-01	
t Critical two-tail	4.30E+00	

Bioaerosol concentration of 631 #/cm^3

	Natural	*Ionization*
Mean	1.43E+06	1.27E+06
Variance	6.33E+10	1.33E+10
Observations	3.00E+00	3.00E+00
Pearson Correlation	9.18E-01	
Hypothesized Mean Difference	0.00E+00	
df	2.00E+00	
t Stat	1.89E+00	
P(T<=t) one-tail	9.97E-02	
t Critical one-tail	2.92E+00	
P(T<=t) two-tail	1.99E-01	
t Critical two-tail	4.30E+00	

Bioaerosol concentration of 451 #/cm^3

	Natural	*Ionization*
Mean	1.02E+06	9.67E+05
Variance	4.63E+09	3.33E+07
Observations	3.00E+00	3.00E+00
Pearson Correlation	6.79E-01	
Hypothesized Mean Difference	0.00E+00	
df	2.00E+00	
t Stat	1.53E+00	
P(T<=t) one-tail	1.33E-01	
t Critical one-tail	2.92E+00	
P(T<=t) two-tail	2.66E-01	
t Critical two-tail	4.30E+00	

Bioaerosol concentration of 90 #/cm^3

	Natural	*Ionization*
Mean	1.93E+05	1.43E+05
Variance	4.23E+09	6.33E+08
Observations	3.00E+00	3.00E+00
Pearson Correlation	3.56E-01	
Hypothesized Mean Difference	0.00E+00	
df	2.00E+00	
t Stat	1.42E+00	
P(T<=t) one-tail	1.45E-01	
t Critical one-tail	2.92E+00	
P(T<=t) two-tail	2.91E-01	
t Critical two-tail	4.30E+00	

Bioaerosol concentration of 9 #/cm^3

	Natural	*Ionization*
Mean	1.09E+04	9.67E+03
Variance	1.21E+06	1.03E+05
Observations	3.00E+00	3.00E+00
Pearson Correlation	-2.07E-01	
Hypothesized Mean Difference	0.00E+00	
df	2.00E+00	
t Stat	1.81E+00	
P(T<=t) one-tail	1.06E-01	
t Critical one-tail	2.92E+00	
P(T<=t) two-tail	2.11E-01	
t Critical two-tail	4.30E+00	